Dynamics of Precursor Films:

Experiment and Theory

PROEFSCHRIFT

ter verkrijging van de graad van doctor
aan de Technische Universiteit Delft,
op gezag van de Rector Magnificus prof. ir. K.C.A.M. Luyben,
voorzitter van het College voor Promoties,
in het openbaar te verdedigen op dinsdag 8 april 2014 om 15:00 uur

door

Mark Johannes Zeger FRANKEN
werktuigbouwkundig ingenieur
geboren te Rotterdam.

Dit proefschrift is goedgekeurd door de promotor:
Prof. dr. ir. J. Westerweel

Samenstelling promotiecommissie:

Rector Magnificus,	voorzitter
Prof. dr. ir. J. Westerweel,	Technische Universiteit Delft, promotor
Dr. ir. C. Poelma,	Technische Universiteit Delft, copromoter
Prof. ir. R.H. Munnig Schmidt,	Technische Universiteit Delft
Prof. dr. A.A. Darhuber,	Technische Universiteit Eindhoven
Dr. ir. R. Badie,	ASML
Prof. dr. ir. J. Snoeijer,	Universiteit Twente
Prof. dr. M. Yoda,	Georgia Institute of Technology
Prof. dr. ir. G. Ooms,	Technische Universiteit Delft, reservelid.

The work in this thesis was carried out at the Laboratory for Aero & Hydrodynamics of the faculty of Mechanical, Maritime & Materials Engineering of the Delft University of Technology. It is part of the research programme 'Contact Line Control during Wetting and Dewetting' (CLC) of the 'Stichting voor Fundamenteel Onderzoek der Materie (FOM)', which is financially supported by the 'Nederlandse Organisatie voor Wetenschappelijk Onderzoek (NWO)'. The CLC programme is co-financed by ASML and Océ.

Copyright © 2014 by M.J.Z. Franken
All rights reserved.
ISBN 978-94-6108-644-0

Printed by Gildeprint V.V., Enschede

Contents

Summary

Dynamics of Precursor Films: Experiment and Theory - M.J.Z. Franken

Despite the fact that moving droplets are very common, a moving contact line is a long-standing fundamental challenge in the field of fluid mechanics. This fundamental challenge is the main topic of this thesis in the context of ASML immersion lithography equipment.

In Chapter 2 an overview of existing theoretical and experimental work is given, that focuses on the mechanism of singularity removal in case of a moving contact line. In order to get more insight in this mechanism, it was proposed to study the nanoscale region of a contact line while it is moving. In this region van der Waals forces come into play and the contact line is referred to as a precursor film. Two types of precursor films exist, namely adiabatic and diffusive, which are present in case of a moving or non-moving contact line respectively. The current experimental results demonstrate the existence of a precursor film, but remain qualitative only in case of a moving precursor film. Hence, there is no adequate comparison of experimental results with the complete theory. Furthermore, conflicting results exist regarding the existence of a precursor film in a partial wetting situation. Nevertheless, a good understanding of the behavior of precursor films in the case of complete wetting is present, and the experimental results for the diffusive precursor film are in good agreement with theory. However, there is no experimental data regarding (the film profile of) adiabatic precursor films. This is related to the inherent difficulty of probing the region of a precursor film due to the great disparity of length and time scales involved. Moreover, understanding the behavior of adiabatic films is the key to understanding moving contact lines. Therefore, a measurement technique with sufficient spatial as well as temporal resolution is developed to probe this region.

Chapter 3 describes Total Internal Reflection Fluorescence Microscopy (TIRFM), which formed the basis for the developed measurement technique. TIRFM is an advanced microscopy technique that limits the illumination to a very thin layer at the substrate by using an evanescent wave. This offers an unprecedented signal-to-noise ratio since only the fluorescent particles or fluorophores within the penetration depth of the evanescent wave are producing signal towards the detector. Furthermore, the experimental setup is designed and built to accurately measure the precursor film profile while it is moving. The basis of the setup is a TIRF-microscope, which is extended with an AFM-head and a long-distance microscope. This experimental setup allowed simultaneous operation of TIRFM and AFM, such that it was possible to characterize the evanescent field by moving a submicron-sized fluorescent bead attached to an AFM-probe into the evanescent field, while recording its fluorescence intensity. The results confirmed an exponential behavior of the evanescent field, and validated the assumption of a minimum penetration depth for the maximum incident angle setting.

Chapter 4 describes the special considerations to employ TIRFM for quantitatively measuring film thickness. This novel method uses the intensity distribution resulting from total internal reflection of incident light and the value for the penetration depth of the evanescent wave. The methodology and data processing to reconstruct the contact line at a nanoscale from the obtained intensity distributions are described. It is demonstrated that the reconstructed contact line of a droplet based on TIRFM is in good agreement with the contact line obtained from AFM-imaging and conventional contact angle measurement. Moreover, the range of TIRFM in combination with sufficient temporal resolution makes it possible to study moving contact lines at nanoscale level. The developed technique pushes the limits of what is currently possible in order to precisely characterize the profile of an adiabatic precursor film and study its dynamics.

Chapter 5 describes the dynamics of precursor films of advancing and receding contact lines on smooth horizontal glass substrates using the developed technique. The measurement technique has sufficient spatial as well as temporal resolution to capture the contact line at mesoscopic level at various contact line velocities. A theoretical model has been developed to explain the measurements of the advancing precursor film profile. Furthermore, the experimental results agree well with theoretical predictions based on a slip boundary condition at the solid surface. Moreover, the slip length is found to be proportional with the contact line velocity using the lubrication theory.

The difference between an advancing and a receding contact line is commonly referred to as contact line hysteresis, and is explained in Chapter 6. It is experimentally shown for the first time that contact line hysteresis is present at a mesoscopic scale as well. A theoretical model for the advancing and receding contact line is developed in order to explain this difference. When a correction term is introduced into the force balance for the precursor film region of a receding contact line, a good agreement with the experimental results appeared. The correction term was brought into relation with molecular effects that cause wetting and dewetting to be an inherent irreversible process. Hence, it is argued that not all the physics are included in the theoretical model, such as molecular effects, since the model used for the disjoining pressure is a relatively simple model. This is based on literature findings where contact line hysteresis is the result of energy dissipation occuring in advancing and receding contact lines.

Chapter 7 describes a study into the precursor film formed ahead of a meniscus of a wetting fluid in a microfluidic channel. Up to now, only precursor films of a droplet were studied experimentally. The precursor film profile is measured in a microfluidic channel for varying channel depths, in order to study the effect of channel geometry on the profile of the precursor film. The results demonstrate that local flow hydrodynamics have an effect on the wettability.

The research provides insight in the fundamental behavior of fluid spreading and indicates that not all the physics is included in the theoretical models.

Samenvatting

Dynamica van Precursorfilms: Experiment en Theorie - M.J.Z. Franken

Ondanks het feit dat bewegende druppels vaak voorkomen, is een bewegende contactlijn een lang bestaande fundamentele uitdaging op het gebied van stromingsleer. Deze fundamentele uitdaging is het hoofdonderwerp van dit proefschrift in het kader van ASML immersie lithografie-apparatuur.

In Hoofdstuk 2 wordt een overzicht van bestaand theoretisch en experimenteel onderzoek gegeven, dat zich richt op het mechanisme dat de singulariteit verwijdert in het geval van een bewegende contactlijn. Om meer inzicht in dit mechanisme te krijgen, is voorgesteld om op een nanoschaal een contactlijn te bestuderen terwijl deze in beweging is. Op deze schaal werken van der Waals krachten en wordt de contactlijn aangeduid als een precursorfilm. Twee types precursorfilms bestaan, namelijk adiabatische en diffusieve, welke respectievelijk worden gevormd in het geval van een bewegende of stilstaande contactlijn. De huidige experimentele resultaten tonen het bestaan van een precursorfilm aan, maar zijn kwalitatief in het geval van een bewegende precursorfilm. Daarom is er geen goede vergelijking mogelijk met resultaten van experimenten en de volledige theorie. Bovendien bestaan er tegenstrijdige resultaten over het bestaan van een precursorfilm in het geval van gedeeltelijke bevochtiging. Desondanks is er een goed begrip van het gedrag van precursorfilms bij volledige bevochtiging, en de experimentele resultaten voor een diffusieve precursorfilm zijn in goede overeenstemming met de theorie. Echter zijn er geen experimentele gegevens betreffende (het filmprofiel van de) adiabatische precursorfilms. Dit hangt samen met de inherente moeilijkheid om een precursorfilm te onderzoeken vanwege de grote verschillen in lengte- en tijdschalen. Hoe dan ook is het begrip van het gedrag van adiabatische precursorfilms de sleutel tot het begrijpen van bewegende contactlijnen. Om deze precursorfilms te onderzoeken is derhalve een meettechniek vereist met voldoende resolutie in zowel plaats als tijd.

Hoofdstuk 3 beschrijft *Total Internal Reflection Fluorescence Microscopy* (TIRFM), welke de basis vormt voor de ontwikkelde meettechniek. TIRFM is een geavanceerde microscopie techniek die de belichting beperkt tot een zeer dunne laag op het substraat door middel van een *evanescent wave.* Dit biedt een ongeëvenaarde signaal-ruisverhouding, aangezien alleen de fluorescente deeltjes of fluoroforen binnen de indringdiepte van de *evanescent wave* signaal produceren richting de detector. Verder is de experimentele opstelling ontworpen en gebouwd om nauwkeurig het profiel van een bewegende precursorfilm

te meten. De basis van de opstelling is een TIRF-microscoop, welke is uitgebreid met een AFM-kop en een lange-afstands microscoop. Deze experimentele opstelling laat gelijktijdig gebruik van TIRFM en AFM toe, zodat het mogelijk is om de *evanescent wave* te karakteriseren door een fluorescent deeltje van submicron afmeting in de *evanescent wave* te bewegen, terwijl de intensiteit van het fluorescente signaal gemeten wordt. De resultaten bevestigden het exponentiële verloop van de *evanescent wave* en valideren de aanname van een minimale indringdiepte voor een maximale invalshoek.

Hoofdstuk 4 beschrijft de maatregelen om TIRFM te gebruiken voor een kwantitatieve meting van filmdiktes. Deze nieuwe methode gebruikt de intensiteitsverdelingm, welke een gevolg is van totale reflectie van invallend licht en de waarde van de indringdiepte van de *evanescent wave*. De methodiek en de verwerking van gegevens uit de verkregen intensiteitsverdelingen om de contactlijn te meten op een nanoschaal worden beschreven. Er wordt aangetoond dat de gereconstrueerde contactlijn van een druppel op basis van TIRFM goed overeenkomt met de contactlijn aan de hand van AFM-metingen en conventionele contacthoek metingen. Bovendien maakt het bereik van TIRFM in combinatie met voldoende tijdsresolutie het mogelijk om bewegende contactlijn te bestuderen op een nanoschaal. De ontwikkelde techniek verlegt de grenzen van wat op dit moment mogelijk is. Hierdoor kan nauwkeurig het profiel van een adiabatische precursorfilm gemeten worden, om zo de dynamiek hiervan te bestuderen.

Hoofdstuk 5 beschrijft de dynamiek van de precursorfilms van vooruitgaande en terugtrekkende contactlijnen op gladde horizontale glazen substraten met behulp van de ontwikkelde techniek. De meettechniek heeft voldoende resolutie in zowel plaats als tijd, zodat de contactlijn op mesoscopisch niveau bij verschillende contactlijnsnelheden gemeten kan worden. Een theoretisch model is ontwikkeld om de metingen van vooruitgaande precursorfilm profiel te verklaren. Verder komen de experimentele resultaten goed overeen met de theoretische voorspellingen gebaseerd op een slip randvoorwaarde bij het vaste oppervlak. Bovendien wordt met behulp van de lubricatietheorie de sliplengte evenredig bevonden met de contactlijnsnelheid.

Het verschil tussen een vooruitgaande en een terugtrekkende contactlijn wordt gebruikelijk aangeduid als contactlijn hysterese, en wordt toegelicht in Hoofdstuk 6. Het is voor de eerste keer experimenteel aangetoond dat contactlijnhysterese ook aanwezig is op een mesoscopische schaal. Een theoretisch model voor de vooruitgaande en terugtrekkende contactlijn is ontwikkeld om dit verschil te verklaren. Wanneer een correctiefactor in de krachtenbalans van de precursorfilm van terugtrekkende contactlijn wordt geïntroduceerd ontstaat een goede overeenkomst met de experimentele resultaten. De correctie term is in verband gebracht met effecten die tijdens bevochting en ontvochtiging een inherent onomkeerbaar proces veroorzaken. Daarom wordt verondersteld dat niet alle fysica aanwezig is in het theoretische model, zoals moleculaire effecten, aangezien het model voor de *disjoining pressure* een relatief eenvoudig model is. Dit is gebaseerd op literatuur bevindingen waar contactlijn hysterese het resultaat is van energiedissipatie in vooruitgaande en terugtrekkende contactlijnen.

Hoofdstuk 7 beschrijft een studie naar de precursorfilm van een meniscus van een bevochtigende vloeistof in een microkanaal. Tot op heden zijn alleen precursorfilms van een druppel experimenteel onderzocht. Het profiel van een precursorfilm is gemeten in een microkanaal voor verschillende kanaaldieptes, met als doel het bestuderen van enig effect van kanaalgeometrie op het profiel van de precursorfilm. De resultaten tonen aan dat de lokale hydrodynamica een effect heeft op de bevochtigbaarheid.

Het onderzoek geeft inzicht in het fundamentele gedrag van vloeistofspreiding en geeft aan dat niet alle fysica in de theoretische modellen aanwezig is.

Chapter 1

Introduction

1.1 Droplets

Droplets in daily life

Droplets are daily present in our life. Nothing is as common as rain in the Netherlands, meaning that everyone should have observed moving droplets on e.g. a car windscreen or a plant leaf during rainfall, as shown in Figure 1.1a. In these cases, a droplet is moving over a surface, referred to as contact line dynamics. Despite the fact that this is such a common phenomenon, it is a long-standing fundamental challenge in the field of fluid mechanics.

Not only in our daily life wetting phenomena are encountered, but also in industrial processes, such as coating, printing, painting, lubrication and oil recovery. In these situations, a liquid and a solid surface are brought together and maintain contact with each other. For example, in ASML immersion lithography equipment, shown in Figure 1.1b, a layer of liquid is used to enhance the optical performance.

Immersion lithography

In semiconductor industry, photolithography is used for patterning a substrate, whereby a photoresist is exposed to light (see e.g. Mack, 2007). A photoresist is a light-sensitive material needed for the process of photolithography and is deposited on a thin slice of semiconductor based material, referred to as a wafer. The wafer is typically made of silicon crystal and forms the basis of an integrated circuit.

Integrated circuits (often referred to as IC's, chips, or microchips) are basically present in all our electronic equipment. One simply cannot think of a world without any electronic devices, such as computers, tablets, smart phones, and cameras.

Integrated circuits are electronic circuits manufactured by repeated application of the photolithography process mentioned above. In such a process, different layers of photoresist are patterned by light amongst other processes, such as etching, ion implantation,

(a) (b)

Figure 1.1: (a) Rain droplets on a leaf (photograph taken in Kiev, Ukraine), (b) state-of-the-art ASML immersion lithography equipment: TWINSCAN NXT:1950i (www.asml.com). The inset shows a schematic of the immersion lens of the lithography system.

developing and removing of layers. These processes make it possible to create structures or features (hence functionality) and form interconnections leading to a well-designed integrated electronic circuit.

In high-end applications, the performance of a microchip is mainly determined by the size of the smallest features on a chip. This means that the performance of chips can be enhanced when the resolution of the pattern is increased, thereby reducing the dimensions of features.

In conventional lithography equipment, the medium between the projection lens and the wafer is air. Though in immersion lithography, air is replaced by a liquid (typically water) between the projection lens and the wafer (see the inset of Figure 1.1b), enabling an increase in numerical aperture. This enhances the optical performance of the system and makes it possible to reduce the dimensions of the features on a chip. The performance of integrated circuits is therefore directly dependent on the resolving power of the optical system used.

Challenges

Besides the enhanced optical performance by the introduction of a liquid in between the lens and wafer, new challenges arise due to the presence of this immersion liquid. In particular, the throughput (number of wafers per unit of time) is limited by the speed at which the wafer can be scanned without having detrimental effects of losing fluid, usually referred to as the critical speed.

In an immersion lithography system, a thin layer of liquid is formed between the wafer and the projection lens by supplying and extracting liquid below the projection lens. This thin layer of liquid is referred to as the immersion lens.

Due to the high-speed scanning motion of the wafer, the liquid-air-wafer interface (the so-called contact line) can be deformed. This deformation can result in loss of immersion liquid in the form of small droplets. These droplets can remain fixed to the wafer and in turn cause imaging defects, and thus affecting the production yield.

A good understanding of contact line dynamics is therefore essential for the development of advanced immersion lithography tools.

Contact line instabilities are dominantly influenced by surface properties of the substrate as well as critical local hydrodynamic flow conditions. In order to improve the performance (e.g. production yield and throughput) of these machines, a fundamental understanding of the behavior of the contact line is crucial.

1.2 Contact line dynamics

The instabilities that limit the performance of ASML immersion lithography equipment, occur at the contact line of the immersion lens (Riepen et al., 2008). Although, the immersion lens is very complex, this system can be reduced to a single moving droplet. In that case the dynamic contact line provides fundamental insight into the behavior of such a complex system.

For moving contact lines, the assumption of a simple wedge profile leads to a non-integrable stress singularity at the contact line, as described by Huh and Scriven (1971) and Dussan V (1979). Although, the dynamic contact line has been extensively studied theoretically, numerically, as well as experimentally, many issues regarding contact line motion remain (Popescu et al., 2012; Snoeijer and Andreotti, 2013).

In order to overcome this predicted singularity, long-range van der Waals forces and slip velocities have been introduced in models by de Gennes (1985) and Haley and Miksis (1991) respectively. However, up to now there is no physical justification of relaxing the no-slip boundary condition in order to relieve the stress singularity by introducing slip at the solid surface (Navier, 1823; Huh and Mason, 1977; Hocking, 1977).

The shape of a spreading droplet that (partially) wets a surface is described by the macroscopic contact angle. However, a microscopically thin precursor film is formed ahead of a macroscopic droplet, as first observed by Hardy (1919). This precursor film is formed by a disjoining pressure originating from van der Waals forces.

de Gennes (1985) emphasized the specific role of the precursor film for droplet spreading. He showed that all the free energy is dissipated in the precursor film. Because of the presence of the precursor film, the velocity field does not diverge, since its thickness does not vanish. As a result, the viscous force at the contact line is finite, which eliminates the singularity at the macroscopic contact line.

At the nanoscale, the theoretically predicted interface varies logarithmically with the distance from the contact line, and a local contact angle needs to be defined, as shown by Joanny and de Gennes (1986). How the van der Waals forces influence the droplet spreading and how these affect the singularity removal remains unclear. According to Cazabat (1987), the answer to the question *How does a droplet spread?* should be found at the microscopic level.

To determine the shape of a spreading drop, light interference patterns have been used by Chen and Wada (1989). From these interference patterns, the meniscus shape of the droplet edge was reconstructed, and the advancing dynamic contact angle was measured. However, the effect of van der Waals forces on the shape of the interface has not been observed in the measurement range attainable by interference due to inherent limitation of the wavelength of light.

Heslot et al. (1992) used ellipsometry by looking at the change of polarization of light, which is reflected off a sample. Ellipsometry can yield information about thin films that have a thickness smaller than the wavelength of the probing light itself, and thus has a sub-wavelength resolution for the measurement. However, the spatial resolution in the plane of the substrate is typically much less and therefore their technique was not adequate to fully explore the characteristics of a moving contact line at nanoscale level.

In order to overcome the limitation of the wavelength of light, a phasemodulated interference microscopy technique was used by Kavehpour et al. (2003). This technique enabled them to simultaneously measure both the inner (microscopic) length scale and the outer (macroscopic) flow scale of a nonvolatile viscous liquid spreading on a smooth horizontal substrate. Their results for the macroscopic contact angle and the lateral scale of the precursor film agree quantitatively with theoretical predictions. However, the sensitivity in combination with the out-of-plane resolution was not sufficient to determine the shape of the precursor film in case of a moving contact line.

Epifluorescence inverted microscopy was more recently used by Hoang and Kavehpour (2011) to study the evolution of a nanoscale precursor film. Although the shape of the interface of a completely wetting fluid was measured, they were limited to a very long time scale of the order of seconds. Therefore, only a diffusive precursor film (described in detail in Chapter 2), instead of an adiabatic precursor film could be measured. The diffusive precursor film is developed in later stages of spreading, and is the result of a gradient of the disjoining pressure, whereas the adiabatic precursor film moves with a constant velocity and is developed in shorter times, and thus requires sufficient temporal resolution as well.

In contrast to complete wetting, which is relatively well understood, many unresolved issues about partial wetting still exist (Ralston et al., 2008; Popescu et al., 2012). For example, the dynamic nanoscale interface shape is undetermined below a film thickness of about 1 μm for a partially wetting fluid. In order to obtain information on the interface of the droplet below 1 μm, a new technique is required for doing these near-wall measurements.

A technique that is capable of doing near-wall measurements is total internal reflection fluorescence microscopy, which is not limited to the wavelength of the light in the direction perpendicular to the substrate, and therefore has the required sub-wavelength resolution to accurately measure film thickness.

1.3 Research objectives

This thesis focuses on the development and application of a new optical measurement technique that is suitable for the study of dynamic contact lines at nanoscale level. From a review of methods for the measurement of contact lines and their suitability for measuring dynamic contact lines, it can be concluded that the key for achieving this goal is to develop a new technique based on fluorescence microscopy.

Total internal reflection fluorescence microscopy is currently the most promising technique to achieve the required out-of-plane resolution and signal-to-noise ratio. However, this microscopy technique requires special considerations and methodologies in order to be utilized for the study of nanoscale contact line dynamics.

The adaptation and characterization of total internal reflection fluorescence microscopy, the validation by an other measurement technique, as well as the study of contact line dynamics at nanoscale level are the main subjects of this thesis.

The study on nanoscale contact lines addresses the following three key subjects: (i) development and validation of an optical measurement technique suitable for the study of contact lines at nanoscale level, (ii) moving contact lines of a droplet measured at nanoscale level, (iii) effect of geometry and surroundings on the behavior of a contact line at nanoscale level.

First, total internal reflection fluorescence microscopy forms the basis of the measurement technique. Furthermore, non-disturbing imaging by atomic force microscopy is used to validate the measured droplet interface. While the second step concerns the development of an experimental setup to actuate a droplet such that an advancing and a receding contact line can be studied at nanoscale level and gives direction to droplet coalescence. The third step was addressed by considering the wetting inside a microfluidic channel.

1.4 Outline of thesis

The thesis concludes the entire development of a measurement technique that can measure contact lines at nanoscale level and demonstrates its applicability for dynamic contact lines.

In Chapter 2, an overview of theoretical and numerical work in the literature is given. Furthermore, a description is given of the problem under investigation, whereas the relevant equations are derived in Appendix A.

Chapter 3 covers the basics of Total Internal Reflection Fluorescence Microscopy (TIRFM). Furthermore, the required characterization of the evanescent excitation field by a combined TIRFM-AFM calibration is dealt with in this chapter. The required experimental setup is elucidated as well as the importance of several parameters in this calibration procedure.

The developed method to obtain the shape of a droplet interface at nanoscale level, as well as a validation by non-disturbing imaging by Atomic Force Microscopy (AFM) are described in Chapter 4. For this, the basics of AFM are described, and further related issues for the application, including several accuracy and sensitivity aspects for the measurement of a droplet interface at nanoscale level are discussed.

Chapter 5 describes the measurement of a non-equilibrium or dynamic contact line of a droplet at nanoscale level. The results are obtained for droplets of different working fluids and contact line velocities. The results are discussed and compared with a developed theoretical model and data available in literature for larger length scales. In addition, the difference between an advancing and a receding precursor film, referred to as contact line hysteresis, is discussed in Chapter 6.

Chapter 7 describes the effect of geometry on the shape of the nanoscale interface by studying the dynamics of it in a microfluidic channel. The results are compared with the results obtained for a moving droplet interface.

This thesis ends with the conclusions and several recommendations for further research in Chapter 8. These recommendations should form the basis for a better understanding of contact line motion by measuring the flow field at the edge of a moving droplet.

Moreover, the enhancement of existing Total Internal Reflection Velocimetry (TIRV) techniques in combination with required modifications, and an extention of the existing experimental setup are described in Appendix B and C.

Chapter 2

Physical Background of Wetting Phenomena

This chapter describes droplet spreading, the regime of partial wetting and the different types of precursor films that can exist. Furthermore, a review of experimentally obtained results for the precursor film is given. A more thorough review, covering more aspects of wetting and dewetting phenomena of different systems is provided in a recent review paper by Popescu et al. (2012). In this chapter only the relevant subjects are described.

2.1 Wetting phenomena

When a droplet is in contact with a surface it makes a certain (apparent) contact angle. Hence, when $\theta = 0$ the system is referred to as complete wetting. In the case when $0 < \theta \leq 180\,^{\circ}$, the system is referred to as partial wetting. The contact angle θ thus characterizes the wettability of the system, and is defined as the angle between the solid/liquid and the liquid/gas interfaces, as illustrated in Figure 2.1 for a droplet in equilibrium.

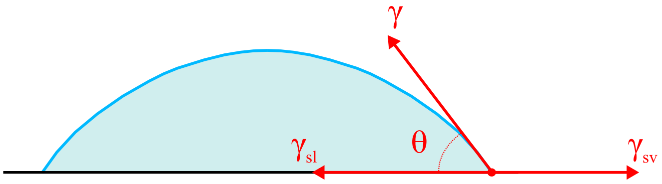

Figure 2.1: Schematic of force balance of a macroscopic droplet in static (mechanical) equilibrium, where θ is the contact angle the droplet makes with the solid. The surface tension between liquid and vapor, solid and vapor, and solid and liquid is denoted by γ, γ_{sv}, and γ_{sl}, respectively.

By balancing the forces related to the surface tensions in the horizontal direction, the Young's equation is found

$$\cos\theta = \frac{\gamma_{sv} - \gamma_{sl}}{\gamma}\,, \tag{2.1}$$

The contact angle θ in Equation 2.1 is a macroscopic or apparent contact angle, and is measured relatively far away (tens of micrometers) from the surface, such that the effect of long-range molecular forces (such as van der Waals forces that act until tens of nanometers) is not observed. It should be noted that the vertical component of the force related to the surface tension is unbalanced.

In order to distinguish between partial and complete wetting, a spreading coefficient S is introduced in Equation 2.1, and is rewritten to

$$\cos\theta = 1 + \frac{S}{\gamma}\,, \tag{2.2}$$

by using the spreading coefficient

$$S = \gamma_{sv} - \gamma - \gamma_{sl}\,, \tag{2.3}$$

which can be either 0 or negative depending on the contact angle of the droplet with the substrate. For a partial wetting droplet S is negative.

2.2 Spreading of liquids in a continuum picture

A complete overview of the different regimes including complete wetting is described by Brochard-Wyart et al. (1991); here only the regime of partial wetting is discussed. de Gennes (1985) describes a relatively simple model for the disjoining pressure (see Section 2.3.1) that can be used as a model for the disjoining pressure. De Gennes assumed that the long-range interaction is not oscillating and can be described by the effective Hamaker constant A (which is the difference between A_{sl} and A_{ll}, as described by Israelachvili, 1997; de Gennes, 1985). Here A_{sl} is the Hamaker constant for the interaction of a liquid film with a solid surface, and A_{ll} is the Hamaker constant for the interaction of two liquid films. The key parameters are then the spreading coeffient S (see Equation 2.3) and the effective Hamaker constant A, such that wetting can be discussed in terms of the free energy F (Brochard-Wyart et al., 1991)

$$F(h) = \gamma_{sl} + \gamma + \frac{A}{12\pi\, h^2}\,, \tag{2.4}$$

where h is the film thickness.

In partial wetting, the droplet makes a finite contact angle given by the Young equation (Equation 2.1) with the dry substrate, as illustrated in Figure 2.1. The spreading parameter S is smaller than zero, and the effective Hamaker constant larger than zero (i.e. $S < 0$ and $A > 0$). When $A > 0$, the liquid layer tends to be thickened by the van der Waals interaction, referred to as the repulsive case. An out-of-equilibrium situation is present when the contact line is moving, and is characterized by the capillary number

$$Ca = \frac{\mu U_{CL}}{\gamma}, \tag{2.5}$$

where U_{CL} is the contact line velocity. The capillary numuber is the ratio of viscous forces over capillary forces.

Contact line dynamics

Huh and Scriven (1971) showed that a no-slip boundary condition for a moving contact line is incompatible from a kinematic point of view, and is discussed by Dussan V and Davis (1974). As illustrated in Figure 2.2, the streamlines make a sharp turn to satisfy conservation of mass, resulting in a diverging velocity gradient when approaching $h = 0$. As a consequence, the shear stress diverges and a mathematical singularity arises. Hence, it requires an infinitely large force to move a contact line over a solid surface, which means that the contact line is no longer allowed to move along the substrate. However, from daily life observations it is obvious that droplets are able to move, and suggests that the model of Huh and Scriven (1971) does not provide a complete description of the moving contact line.

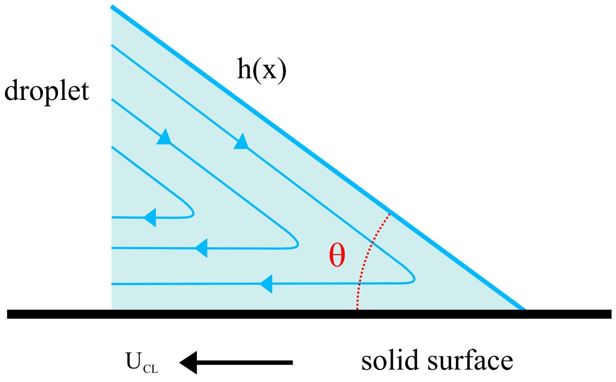

Figure 2.2: Streamlines in a wedge for an advancing contact line (analytical solutions are given by Huh and Scriven, 1971), where θ and U_{CL} are the contact angle and contact line velocity respectively.

Several mechanisms are proposed to remove the singularity in the shear stress at the solid surface, e.g. by relaxing the no-slip boundary condition. Such a slip condition was introduced by Navier (1823). The approach to use a slip condition at the solid surface instead of a no-slip condition has been used by many others (Huh and Scriven, 1971; Hocking, 1976; Dussan V, 1976; Hocking, 1977; Huh and Mason, 1977; Greenspan, 1978; Lowndes, 1980; Durbin, 1988; Liao et al., 2013). It should be noted that the no-slip boundary condition (i.e. the liquid adjacent to the solid surface does not slip relative to the solid surface) is a generally accepted boundary condition in fluid mechanics. It is worth mentioning that it is completely deduced from experimental observations.

Slip at solid surfaces

Slip is characterized by the distance to the surface at which the velocity extrapolates to zero, and is referred to as the slip length L_{slip}. Figure 2.3 illustrates two cases of slip, namely no slip and partial slip.

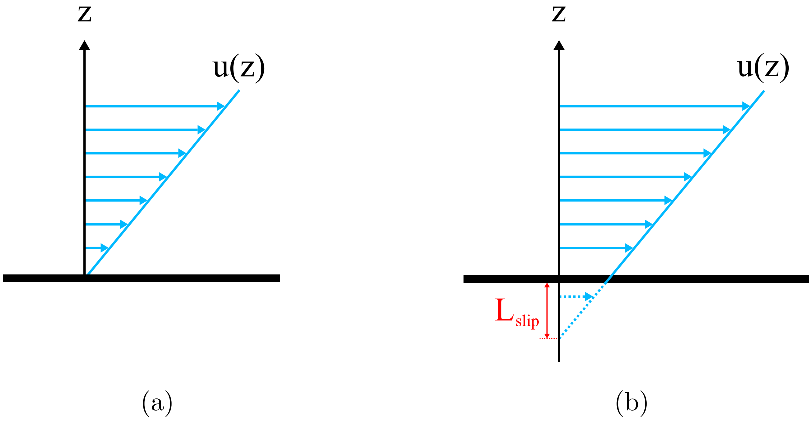

Figure 2.3: Schematic of slip in the case of viscous flow near a solid surface: (a) no slip, (b) a finite L_{slip}.

An other option to relieve the stress singularity is to include a precursor film, such that the wedge is treated as a nearly flat film close to the substrate. The precursor film is a multi-scale feature of a droplet of submicron thickness, and arises due to the effect of intermolecular forces via the so-called disjoining pressure. Popescu et al. (2012) described that in the case of complete wetting a macroscopic nonvolatile drop spreads very slowly due to the balance between the hydrodynamic viscous dissipation in the bulk and the Young force (which drives the droplet spreading). In this process, the stress singularity is removed because the precursor film serves as a lubricant for the macroscopic contact line.

2.3 Precursor films

In 1919, a precursor film of a wetting liquid on glass was first observed by Hardy (1919). Furthermore, most of the theoretical work regarding the behavior of precursor films was done by or in cooperation with de Gennes (see e.g. de Gennes, 1985). de Gennes (1985) assumed that a continuum approach of the contact line still holds up to 3 nm. Moreover, his theoretical analysis focuses on a region ranging from about 1 μm up to 3 nm, referred to as the mesoscopic region as shown in Figure 2.4. In this region long-ranged forces start to play a relevant role, and are taken into account by the disjoining pressure.

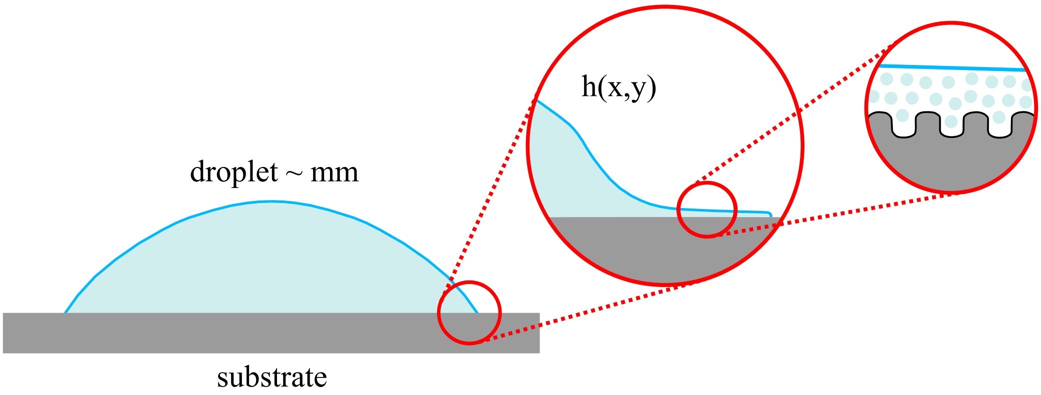

Figure 2.4: Schematic of different droplet regions. The first inset shows the mesoscopic region where the precursor film of thickness $h(x, y)$ formed ahead of the macroscopic contact line. Whereas, the second inset shows the molecular region of the precursor film of the droplet. It should be noted that this figure is a schematic representation of the different regions, and therefore not drawn to scale.

2.3.1 Disjoining pressure

The disjoining pressure Π arises from an attractive interaction between two surfaces and was introduced by Derjaguin in 1936 (see e.g. Derjaguin et al., 1954), and equals the difference in pressure within a film between two surfaces and the pressure in the bulk phase (Butt et al., 2003). It provides a description of the intermolecular forces responsible for the finite equilibrium contact angle, and tend to disjoin thin films in the case of repulsive surface forces (or cojoin if negative in the case of attractive surface forces). Teletzke et al. (1988) described that the disjoining pressure is commonly divided in a molecular component Π_m, an electrostatic component Π_e, and a structural component Π_s. For relatively thick films, the molecular component predominates the disjoining pressure, but when the film thickness becomes smaller this assumption is likely to break down. The effect of the disjoining pressure was not observed above approximately 100 nm on the interface of a droplet of silicone oil on mica (due to a limitation in spatial resolution of their measurement technique), as shown by the first explicit measurements of a droplet profile by Chen and Wada (1989).

Two limiting cases exist for the description of the precursor film, namely a stationary case when the contact line is slowly moving (i.e. $U_{CL} \neq 0$), and a non-stationary case. In these cases the precursor film is called adiabatic and diffusive respectively, and are described below.

2.3.2 Adiabatic precursor film

An adiabatic precursor film is formed ahead of a slowly moving macroscopic contact line with a relatively low constant (or slowly varying) velocity U_{CL}. In case of a stationary moving interface it is assumed that the timescale in which the shape of the moving interface settles is much shorter than the scale at which the contact line velocity U_{CL} varies. In case of an adiabatic film, the interface profile $h(x)$ scales as $1/x$ based on a no-slip condition at the solid surface (Joanny and de Gennes, 1986; Hervet and de Gennes, 1984; de Gennes, 1985). However, de Gennes (1985), Bruinsma (1990) and Brochard-Wyart et al. (1994) showed that a scaling of the precursor film profile $h(x)$ of $1/\sqrt{x}$ arises based on a slip condition at the solid surface. This means that the precursor film slipping over a solid surface thins more slowly compared with the case of no-slip. Although they described precursor films encountered during the spreading of polymer melts on semi-ideal surfaces, it is assumed that their theory based on slip also holds for general cases where slip is present. Furthermore, Brochard-Wyart et al. (1994) noted that for the slipping case the profile of the macroscopic foot and the precursor become independent of the velocity U_{CL}. When slip at the solid surface is assumed, Equation A.22 is written as (Bruinsma, 1990; Brochard-Wyart et al., 1994)

$$-\frac{3\mu U_{CL}}{h + 3L_{slip}} = -\gamma\, h\,\frac{\partial^3 h}{\partial x^3} + \frac{A}{2\pi\, h^3}\frac{\partial h}{\partial x}\,, \tag{2.6}$$

and describes the force balance in the dynamic precursor film.

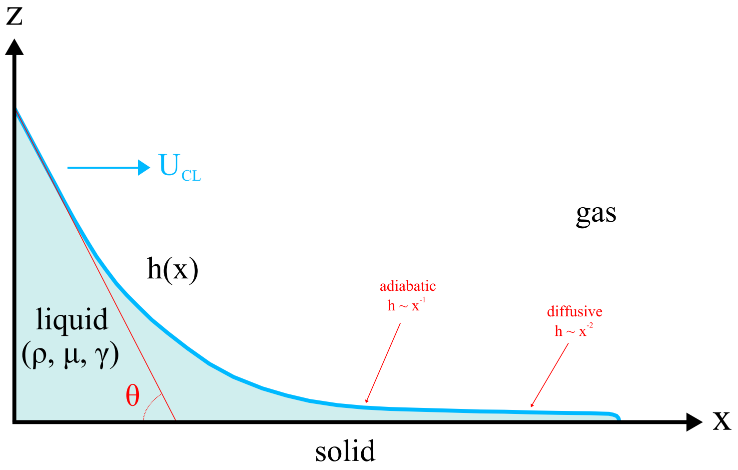

Figure 2.5: Sketch of the precursor film of the droplet, where U_{CL} is the contact line velocity, ρ is the density of the liquid, μ is the dynamic viscosity of the liquid, and γ is the surface tension between liquid and gas.

2.3.3 Diffusive precursor film

The diffusive precursor film is formed due to a gradient of the disjoining pressure along the film ahead of an adiabatic film (Joanny and de Gennes, 1986). This gradient arises because the thickness of the film is not constant, even though the precursor film is nearly flat (e.g. in the case of complete wetting). However, it requires very long times for diffusion to develop this film. By balancing the viscous forces against van der Waals forces (Hervet and de Gennes, 1984; Joanny and de Gennes, 1986), Equation A.21 reduces to a differential equation that describes the spreading of a diffusive film

$$\frac{\partial h}{\partial t} = \frac{\partial}{\partial x}\left[D(h)\frac{\partial h}{\partial x}\right] , \tag{2.7}$$

where the effective diffusion coefficient $D(h)$ is written as

$$D(h) = -\frac{h^3}{3\mu}\frac{\partial \Pi}{\partial h} . \tag{2.8}$$

The development of the diffusive precursor film is controlled by the gradient of the disjoining pressure. Furthermore, a scaling for the shape of the precursor film $h(x)$ of $1/x^2$ is expected for this regime (Joanny and de Gennes, 1986; Ralston et al., 2008; Popescu et al., 2012), and is illustrated in Figure 2.5. Hoang and Kavehpour (2011) provided experimental evidence of the scaling of $1/x^2$ for the precursor film profile $h(x)$. They were able to measure the quasi-static diffusive film by fluorescence microscopy. However, the measurement was lacking sufficient temporal resolution in order to measure an adiabatic precursor film.

Huh and Mason (1977) developed a complete theory for macroscopic droplets, which is characterized by three regions, namely a central region or macroscopic region, a wedge, and a mesoscopic region where finite slippage dominates. Additionallly, Huh and Mason (1977) pointed out that the measurements of the dynamic contact angle were obtained with low optical resolution close to the surface. Therefore the reliability of the experimental data close to the surface is arguable, meaning that the dynamic contact angle can have a different value close to the surface, e.g. close to 180 ° such that liquid elements would roll on the solid. Furthermore, near the contact line there is a possibility of the existence of a region where the continuum hydrodynamics break down (Popescu et al., 2012). This was concluded by Hansen and Toong (1971) as well, but were unable to specify the exact region. This indicates that many open questions exist as stated by Popescu et al. (2012) (and references therein).

2.4 Review of experimental work

Popescu et al. (2012) (as well as Ralston et al., 2008; Bonn et al., 2009) give a review of precursor films in wetting phenomena. Here, only the relevant results are discussed for liquid-on-solid systems.

2.4.1 Introduction

Theoretical studies by e.g. de Gennes (1985) and Hervet and de Gennes (1984) have shown that the precursor film appears to be very important for droplet spreading, whereas its existence depends on van der Waals forces. Due to the presence of the precursor film, the thickness of the droplet interface does not go to zero, and it was shown that all the excess free energy is dissipated in the precursor film, and so the total energy dissipated from the apparent contact line motion is finite. Hence, the stress singularity at the macroscopic contact line is eliminated. Therefore, contact line motion cannot be discussed without incorporating these van der Waals forces. Since Hardy (1919) many attempts have been made to quantitatively measure the precursor film. As described, the scaling of the precursor film profile can provide valuable information regarding the boundary condition at the solid surface, in particular for the case of a moving contact line.

2.4.2 Overview of experiments

Hardy (1919) was the first one to provide evidence of the existence of a precursor film, whereas the first precise characterization of the profile of the precursor film was done by Léger et al. (1988a,b). They used an ellipsometer with a spatial resolution of approximately 10 μm. They found a precursor film, but the profile was in clear disagreement with calculated precursor film profiles by Hervet and de Gennes (1984) and de Gennes (1985).

Beaglehole (1989) found remarkable agreement with de Gennes' predictions concerning the growth and the mass dependence of the precursor film using a microscopic imaging ellipsometer (Beaglehole, 1988). However, the film profile showed consistently different features as well. More recent, ellipsometry was used by Maymoudi et al. (2013) to study electrostatic precursor films.

Kavehpour et al. (2003) used a phase-modulated interference microscopy technique. This technique enabled them to simultaneously measure both the inner length scale and the outer flow scale of a nonvolatile viscous liquid spreading on a smooth horizontal substrate. Their results for the macroscopic contact angle and the lateral scale of the precursor film (i.e. the *length* of the precursor film) agree quantitatively with theoretical predictions by Joanny and de Gennes (1986). However, the sensitivity in combination with the out-of-plane resolution was not adequate to determine the shape of the precursor film in case of a moving contact line.

Xu et al. (2004) used AFM-imaging to monitor the spreading of a polymer drop with molecular resolution, and showed that the mass transport in the precursor film is due to plug flow of polymer chains with minor contribution from molecular diffusion. They confirmed the sliding of a monolayer with the translational and rotational diffusion of molecules within the precursor film of a quasi-stationary drop. AFM-imaging has also been used by Glynos et al. (2011), who found a precursor film protruding from the contact line of a small drop consisting of star-shaped macromolecules.

A technique based on interferometry was used by Konisho and Ueno (2009) to study the advancing edge of a precursor film. They were able to estimate the length of an adiabatic precursor film, but a profile was however not obtained.

Hoang and Kavehpour (2011) studied the precursor film as it evolved over time using a technique based on epifluorescence microscopy. Although their technique (Hoang et al., 2012) had sufficient spatial resolution, temporal resolution was however lacking. Therefore they were not able to characterize an adiabatic precursor film, but a diffusive film instead. The diffusive precursor film took several days to develop, and showed very good agreement with the predictions of the scaling of the profile with $1/x^2$.

2.5 Conclusion and outlook

In conclusion, the existing experimental results demonstrate the existence of a precursor film, but remain only qualitative in case of a moving precursor film. Therefore, there is no adequate comparison of experimental results with the complete theory (de Gennes, 1985). Furthermore, from the paper by Popescu et al. (2012) (and references therein) it is clear that conflicting results exist regarding the existence of a precursor film in a partial wetting situation. These findings are based on experimental observations and Molecular Dynamics (MD) simulations. Nevertheless, a good understanding of the behavior of precursor films in the case of complete wetting is present, and the experimental results for the diffusive precursor film are in good agreement with theory. However, there is no experimental data regarding (the film thickness profile of) adiabatic precursor films. This is related to the inherent difficulty of probing the region of a precursor film due to the great disparity of length and time scales involved. However, understanding the behavior of adiabatic films is the key to understanding moving contact lines. Therefore, a measurement technique with sufficient spatial as well as temporal resolution is required to probe this region.

In the following chapters a measurement technique is described that is capable of measuring adiabatic precursor films. The developed technique pushes the limits of what is currently possible in order to precisely characterize the profile of an adiabatic precursor film and study its dynamics.

Chapter 3

Total Internal Reflection Fluorescence Microscopy and its Characterization*

This chapter describes Total Internal Reflection Fluorescence Microscopy and a study into the characterization of an evanescent wave. This study is done using combined total internal reflection fluorescence microscopy and atomic force microscopy. A review of methods to characterize an evanescent wave experimentally is given. Whereas, the emphasis of this review is on the perturbation of the evanescent field and the accuracy of determination. Our approach to characterize an evanescent excitation field produced by total internal reflection of light, is by atomic force microscopy. This method uses particle-attached probes equipped with a single fluorescent particle to determine the exponentially decaying intensity versus distance curve of the evanescent wave. The results confirm an exponential behavior of the evanescent field, and validate the assumption of a minimum penetration depth for the maximum incident angle setting.

3.1 Total internal reflection fluorescence microscopy

The principle of TIRFM is based on the generation of an evanescent excitation field at the interface of two media with different refractive indices (Axelrod et al., 1984; de Fornel, 2001). When the incident light is beyond the critical angle, the light undergoes total internal reflection and generates a thin electromagnetic field perpendicular to the surface, as illustrated in Figure 3.1a. This electromagnetic field is called an evanescent wave and has a frequency identical to the incident light. Furthermore, the intensity of the evanescent wave decays exponentially with the distance from the substrate along the optical axis,

---

*The content of this chapter has been published in modified form in *Optics Express* (Franken et al., 2013).

as illustrated in the inset of Figure 3.1a. This exponential decay of the intensity of the evanescent wave can be utilized to extend existing techniques, e.g. by recovering height information of fluorescent particles in multilayer nano-particle image velocimetry, as done by Li et al. (2006). By limiting the illumination to a very thin layer at the substrate, this offers the advantage of an unprecedented signal-to-noise ratio since only the particles or fluorophores within the penetration depth of the evanescent wave are producing signal towards the detector.

The critical angle for total internal reflection (TIR) is given by Snell's law

$$\theta_c = \sin^{-1}(n_2/n_1)\,, \tag{3.1}$$

where n_1 and n_2 ($n_2 < n_1$) are the refractive indices of the substrate and medium respectively. The evanescent field intensity has an exponential decay with normal wall distance z from the substrate

$$I(z) = I_0\, e^{-z/d}\,, \tag{3.2}$$

where I_0 is the intensity of the evanescent field at the surface of the substrate ($z = 0$) that depends on the intensity of the incident beam, the incident angle and the polarization (Axelrod et al., 1984; de Fornel, 2001).

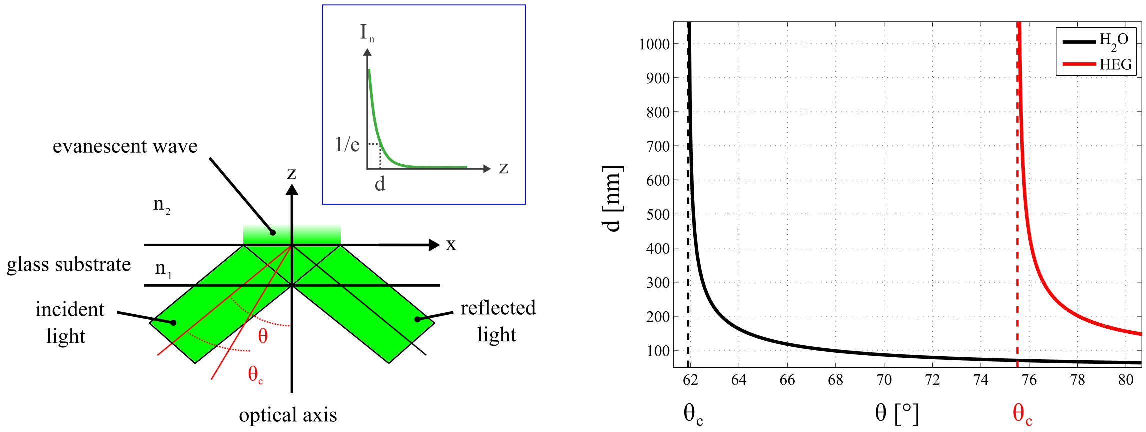

(a) (b)

Figure 3.1: (a) Illumination scheme and coordinate system used, (b) theoretical penetration depth as a function of incident angle for different working fluids (water (H_2O) and hexaethylene glycol (HEG)).

The penetration depth d is defined as the distance from the substrate where the intensity of the evanescent wave decays to $1/e$ of its original value, as illustrated in the inset of Figure 3.1a. It can be calculated using (Axelrod et al., 1984; de Fornel, 2001):

$$d = \frac{\lambda}{4\pi}\left[n_1^2 \sin^2\theta - n_2^2\right]^{-1/2} , \tag{3.3}$$

where λ and θ are the wavelength and incident angle of the light respectively. The penetration depth is in the order of λ or smaller, as shown in Figure 3.1b.

TIRFM is a near-field microscopy technique that operates less than one λ away from the image plane, which typically lies on the surface of the substrate. Its resolution in z is higher than a far-field technique can attain in a near-wall region. This is because the evanescent excitation field contains information beyond the diffraction limit. Therefore, a result is obtained with a higher out-of-plane resolution. However, similar to a far-field technique, the in-plane resolution is represented by the Point Spread Function (PSF), and is described in Section 3.4.

3.2 Overview of methods

The penetration depth of an evanescent excitation field can be estimated using Equation 3.3 and by the geometry of the microscope. However, this cannot be done accurately and reliably (Harlepp et al., 2004). In order to obtain accurate information about the penetration depth, direct calibration of the evanescent wave is necessary. One of the first measurements of evanescent field intensity were obtained using a scanning tunneling optical microscope described by Marti et al. (1993). Several examples of methods to determine the penetration depth of an evanescent wave exist in the literature.

Harlepp et al. (2004) used fluorescence correlation spectroscopy to calibrate the penetration depth of a TIRM setup. Their measured values for the penetration depth are in good agreement with the theoretical ones. However, the maximum penetration depth calibrated was limited to approximately 45 *nm*.

Steyer and Almers (1999) determined the thickness of an illuminating layer in vitro by looking at fluorescent beads adsorbed at the coverslip and to a microscope objective. The microscopice objective was placed on the coverslip with its curved side down, such that it could be moved up and down by a calibrated piezoelectric drive with a resolution of 50 *nm*. They used TIR excitation and epifluorescence in order to determine the intensity versus height profile, which showed a linear relation between fluorescence intensity and distance.

Kanda et al. (2007) used a piezo-stage to calibrate the depth of the evanescent wave, in order to obtain information about the particle distribution in a microchannel flow. They employed 100 *nm* fluorescent particles attached to a 2 *mm* steel sphere in water and found that the particle brightness was almost proportional with distance from the glass substrate. Both of these approaches strongly relied on the accuracy of the piezo-electric stepper.

Mattheyses and Axelrod (2006) directly measured the evanescent field profile by microscopic observation of fluorescently labeled beads attached to a glass substrate in an index-matched solution. The authors obtained double-exponential curves of the evanescent field intensity, in which the majority (90%) of the signal corresponds to a fast exponential, whereas 10% corresponds to a slow exponential. The authors attributed the existence of this slow exponential component to light scattering in the objective.

Gell et al. (2009) used a solution consisting of fluorescently labelled microtubules to characterize the illumination in total internal reflection fluorescence microscopy. One end of the fluorescently labeled microtubule was at or near the surface of the coverglass with some degree of tilt. The tilt angle was determined by epifluorescence microscopy and provides information for the profile of the illuminated light by TIR due to the microtubule tilt. The fluorescence intensity versus distance curves were described by a single-exponential function.

Sarkar et al. (2004) used a combined AFM and TIRF microscope in order to obtain a nanometer-scale-calibrated evanescent wave with sub-nanometer resolution. The experiments were done with quantum dots attached to a cantilever and show single exponential intensity curves for different incident angles.

More recent, Antognozzi et al. (2008) presented a new technique based on scattered evanescent electromagnetic waves that can detect the displacement of the extreme end of a vertically mounted cantilever in a combined TIRFM-AFM setup. In this technique, a tipless AFM cantilever is lowered inside an evanescent field and becomes a scattering point. The cantilever scattered light from a very well defined area while it was positioned inside the evanescent field. By fitting the experimental data to an exponential function with a decay length, they were able to characterize the evanescent field.

However, not all of the methods described above leave the evanescent field unperturbed by e.g. introducing a steel sphere or a cantilever in the evanescent excitation field, or do not provide sufficient accuracy (in the desired measurement range).

Our approach to determine the penetration depth of the evanescent wave uses micrometer sized fluorescent particles in order to minimize the perturbation of the evanescent field by the cantilever of the AFM-head due to refractive index mismatching or scattering of incident light. The AFM-head is capable of approaching the surface of the glass substrate with sub-nanometer accuracy and of lifting the cantilever from the surface with steps of typically 20 nm. The penetration depth was determined by recording the intensity of the particle at various known distances from the surface within a liquid. For this purpose, a liquid-scanner was used to create a liquid-bath of de-mineralized water, as shown in Figure 3.2a.

3.3 Experimental setup

The experiments were conducted with an inverted TIRF-microscope (Eclipse Ti, Nikon Inc, Tokyo, Japan) combined with an AFM-head (CombiScope 1000, AIST-NT BV, Apeldoorn, the Netherlands) positioned on an optical table (Newport RS 4000, Irvine, CA, USA). The inverted microscope was equipped with an oil-immersion objective with a magnification of 60× and a numerical aperture of 1.49 (Nikon APO60×/1.49), and created an evanescent

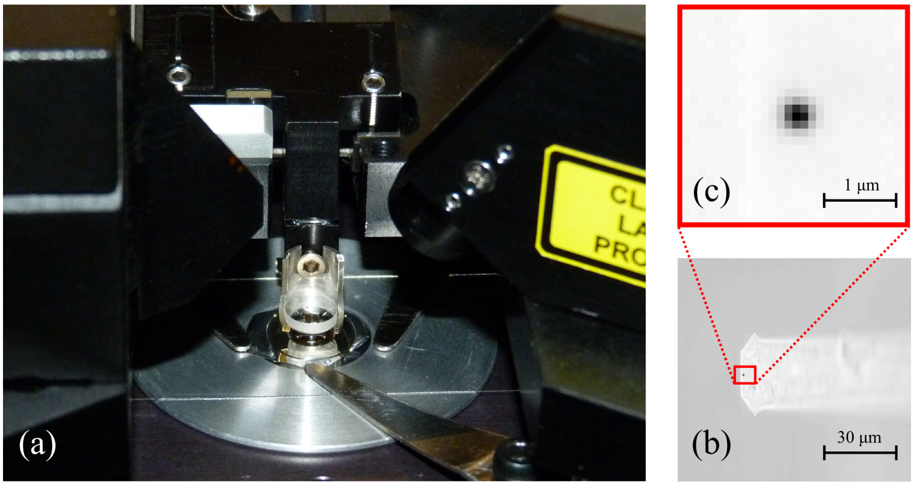

Figure 3.2: (a) Liquid scanner of the AFM-head used for the evanescent wave calibration, and a 0.545 μm fluorescent particle within the field-of-view providing signal towards the CCD: (b) with background light, and (c) close-up of fluorescent particle (without background light).

excitation field by a through-the-objective method (e.g. Sarkar et al., 2004; Huang et al., 2006; Gumpp et al., 2009). In this method (see Figure 3.3) the incident light is directed through the objective, and is reflected back into the objective, while creating an evanescent field. Consequently, a refractive index-matched immersion oil (type NF, refractive index = 1.515; Nikon Inc, Tokyo, Japan) is required for the standard glass substrates (Menzel-Gläser, Braunschweig, Germany). Furthermore, a correction collar was incorporated in the TIRF-objective in order to account for variations in coverslip thickness. After cleaning, the coverslips had a typical RMS surface roughness of less than 1 nm as measured by AFM. The evanescent excitation field was generated by a 150 mW continuous wave Nd:YAG laser (Coherent, Compass 315M; Santa Clara, CA, USA), which was coupled to the microscope using a monomode optical fiber.

The emitted light from the fluorophores passed through a 532 nm dichroic mirror (Chroma Technology, Bellows Falls, USA) and a 532 nm long-pass edge filter (RazorEdge, Semrock, Rochester, NY, USA). These filters separate the longer-wavelength fluorescence from the evanescent wave illumination so that only the fluorescent light was imaged. A cooled 12-bit dynamic range high resolution charged-coupled device (CCD) camera (FlowMaster, 1376 × 1040 pixels, individual pixel size 6.45 × 6.45 μm^2, LaVision GmbH, Goettingen, Germany) was used to capture the emitted light. This camera has a very linear response to incident light (non-linearity $\ll 1\%$ according to the supplier specifications), making it suitable for quantitative photometric analysis.

For the laserdiode of the AFM-head, which emits light with a wavelength of 1300 nm, no additional filters were necessary, since the CCD of the camera was not sensitive to light with a wavelength larger than 1100 nm. Physically decoupling the camera from the microscope, in order to minimize vibrations from the camera fan, reduced the amplitude of the vibrations to less than 1 nm. In addition, an identical camera equipped with a

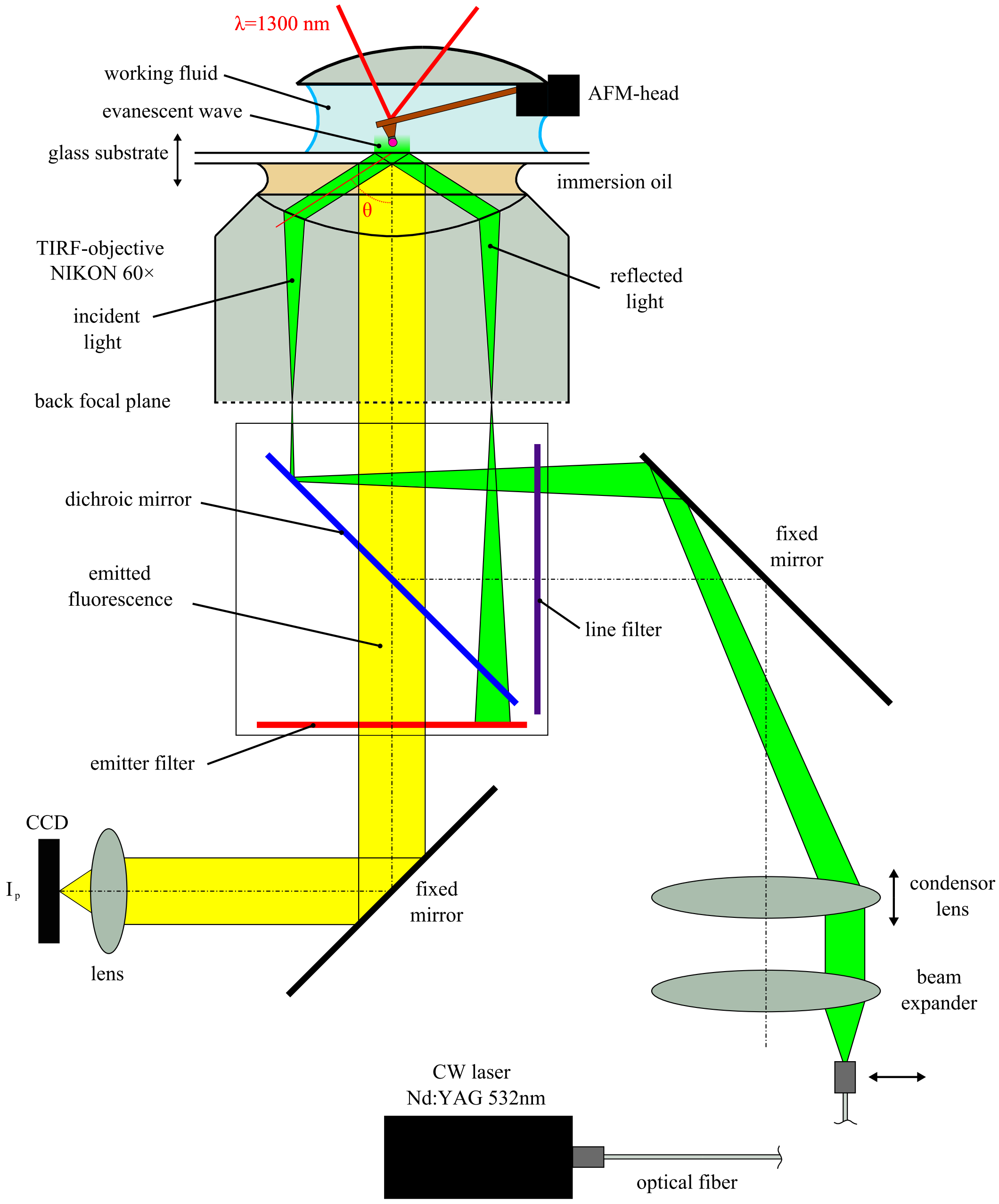

Figure 3.3: Schematic of experimental setup. The actual setup is shown in Figure 3.4.

long-distance microscope with magnifications between 0.8× and 4× (Macro Vario Lens, LINOS Photonics GmbH, Munich, Germany) was used for the side view measurements of the macroscopic contact angle. The images were recorded using DaVis 7.2 (LaVision GmbH, Goettingen, Germany). The detailed schematics and an overview of the experimental setup are shown in Figure 3.3 and 3.4, respectively.

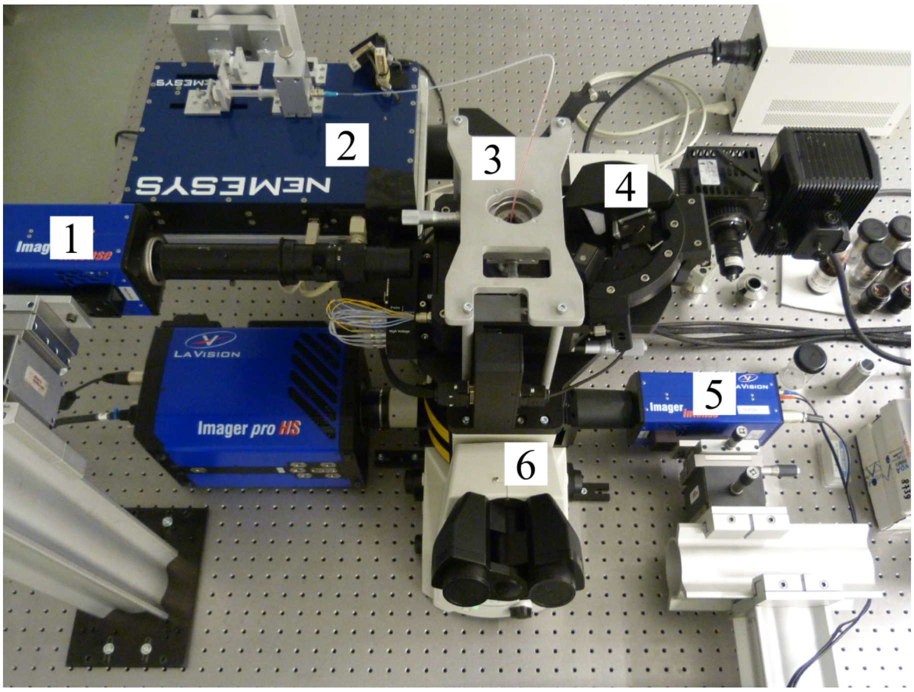

Figure 3.4: Overview of experimental setup, where the different components are indicated with: **1** - side view camera, **2** - syringe pump, **3** - needle positioner, **4** - AFM-head, **5** - bottom view camera, **6** - inverted microscope.

3.4 Spatial resolution of imaging system

As noted, TIRFM can obtain sub-wavelength resolution in the out-of-plane direction, whereas the in-plane resolution is limited by diffraction. The in-plane resolution is commonly characterized by the Point Spread Function (PSF), and provides a description of the optical performance of the imaging system. The PSF describes a response of the imaging system to a point source. In microscopy, a point source is usually the (fluorescent) light emitted by or scattered from a very small (sub-) micron sized bead.

For a high-magnification objective in combination with a very small pixel size of the CCD (here it is $6.45 \times 6.45\ \mu m^2$, as described in Section 3.3), a very small fluorescent bead or quantum dot is required to act as a point source. Therefore, the characterization of the optical system was done by taking an image of a microsphere with a diameter of $40\ nm$ (FluoSpheres, Invitrogen, Eugene, Oregon, USA). The diameter of the fluorescent bead is actually much smaller than the pixel size in the particle image (approximately $110\ nm$ for the combination of objective and CCD), and therefore it can be effectively considered to act as a point source. However, the particle spreads out over several pixels, typically 5×5 (inset of Figure 3.5a). Figure 3.5a shows the fitted intensity plot with a 2D Gaussian profile, and is used to estimate the PSF. For an ideal thin lens the PSF is an Airy function. The central lobe of an Airy function is well approximated by a Gaussian (Adrian and Westerweel, 2010).

The width of the Gaussian profile at half the intensity of the particle image is defined as the PSF, and is approximately 3 pixels, which corresponds to approximately 300 *nm*. In conclusion, the PSF is experimentally determined to be approximately 300 *nm* in diameter, which is slightly larger than the theoretical diffraction limit for an ideal thin lens: the diffraction limit is estimated to be $\lambda/2$NA, which is approximately 200 *nm* for the objective and fluorescent dye (peak emitted at a wavelength of 585 *nm*, see Figure 3.5b) used.

3.5 Characterization by combined TIRFM-AFM

The calibration procedure of the evanescent wave was started by moving the substrate upwards, towards the particle-attached probe. This differs from the approach described by Sarkar et al. (2004), because our AFM-head consists of a sample-scanner instead of a tip-scanner. In a sample-scanner the substrate (and consequently the evanescent field) is moved towards the fluorescent particle attached to the cantilever, whereas the fluorescent particle is moved towards the substrate in a tip-scanner. An automated approach was used to detect the bottom surface of the fluorescent particle with the substrate. Once the particle touched the surface of the substrate, the focus-plane was set by adjusting the vertical position of the microscope objective and therefore bringing the particle into focus. At this position, the maximum intensity of the fluorescent particle was recorded, which was used to determine the intensity at the surface of the substrate I_0. By making small steps of 20 *nm* with the substrate in z-direction and averaging the particle intensity of a number of images (typically 30 images at a recording rate of 2 *Hz*, the particle intensity was determined for each vertical position. Before making a step, the substrate was lowered 500 *nm* in order to prevent the particle-attached probe remains attached to the surface. The intensity versus distance curve was obtained by normalizing the particle intensity with I_0. Hence, this intensity versus distance curve was used to determine the unknown penetration depth of the evanescent excitation field by fitting a single-exponential function.

The number of recordings was chosen to ensure the reconstructed curves are independent of the number of recorded images. This also holds for the selected threshold for the particle detection in the processing of the recorded images. Furthermore, an estimation of the measurement accuracy for the vertical position and the recorded particle intensity was obtained by determining the fluctuation around its position or mean intensity, respectively ± 1 *nm* and ± 5 gray values.

3.6 Materials and equipment

Particle-attached probes

For the calibration of the evanescent wave, custom-made single particle-attached probes were used, as shown in Figure 3.2b. Standard silicon tipless contact-mode AFM probes (Novascan Technologies, Ames, USA) with a spring constant of 0.95 N/m formed the basis

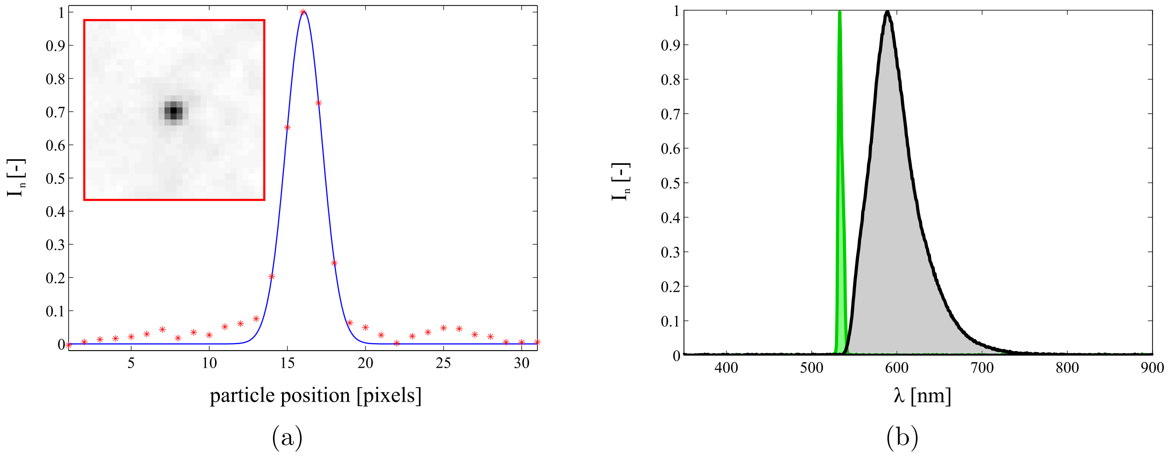

(a)

(b)

Figure 3.5: (a) Particle position of a 40 *nm* fluorescent bead, (b) measured emitted spectrum of Rhodamine B (black) when excited with a Nd:YAG laser (green) in hexaethylene glycol. The emitted spectra were measured with a spectrometer (Ocean Optics, Florida, USA).

of these particle-attached probes. A 545 *nm* polystyrene Rhodamine B labeled bead (Microparticles GmbH, Berlin, Germany) was attached to the cantilever, as shown in Figure 3.2c. The attachment of smaller particles by Novascan Technologies was not possible due to limitations of their equipment.

Working fluid

For the characterization of the evanescent field, a liquid-bath is created around the fluorescent particle as illustrated in Figure 3.2a. Water is chosen as a working fluid, because it is compatible with the particle material (and the adhesive attaching the particle to the cantilever), as well as the optics of the liquid scanner of the AFM-head. An Abbe refractometer is used to determine the refractive index of demineralized water, and equals 1.3320 ± 0.0005. By assuming the system operates at its maximum incident angle ($\theta_{max} = \sin^{-1}(\mathrm{NA}/n_1)$), the penetration depth d of the evanescent field can be estimated using Equation 3.3, and equals 63 *nm*. Note that all the measurements were performed in ambient conditions at room temperature (around 22 °C) and a relative humidity of about 40%.

3.7 Intensity versus distance curve

Simultaneous measurements of the position along the optical axis and the fluorescence intensity emitted by the particle are done by TIRFM and AFM. Equation 3.2 relates the

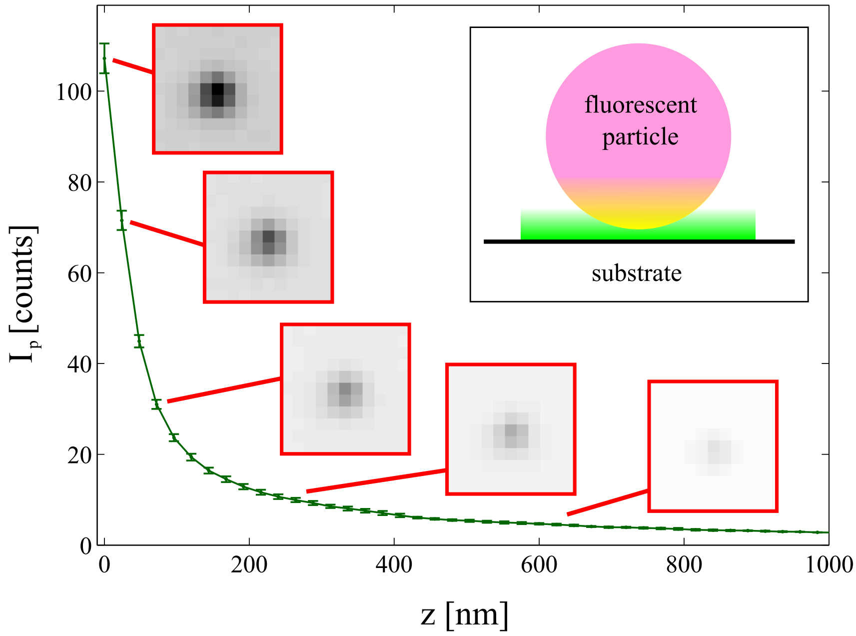

Figure 3.6: Fluorescent particle intensity I_p as a function of distance z of the evanescent field in TIR excitation as measured by a combined TIRFM-AFM setup. The curve was obtained by moving a fluorescent particle in the evanescent field while recording its intensity in water (similar to Sarkar et al., 2004) in order to validate the minimum penetration depth for this incident angle setting. The insets illustrate the particle image at various z-positions (NB: the particle images are inverted for clarity). The inset shows a schematic of a 0.545 μm fluorescent particle (attached to a cantilever) in an evanescent field, in which there is a distance between the particle and the substrate.

particle intensity and distance z. The results averaged over several subsequent measurements are shown in Figure 3.6.

Figure 3.6 displays an exponential decay of the image intensity of a fluorescent particle with respect to z. The insets show the particle image at various locations along the optical axis. The intensity of the particle is obtained by a Gaussian fit of a particle image. This particle image is the average of a number of recordings. In order to compare the experimentally determined intensity versus distance, the particle intensity I_p is normalized with I_0, and is shown in Figure 3.7. The experimentally determined penetration depth of the evanescent wave equals 58 ± 4 nm, and is close to the theoretical penetration depth of 63 nm in water.

Figure 3.7 illustrates the normalized particle intensity I_n as a function of distance normal to the substrate z. As can be seen, the experimental results are in good agreement with the theoretical value. However, the results start to deviate after approximately 150 nm, which is likely caused by the remaining background noise or scattering.

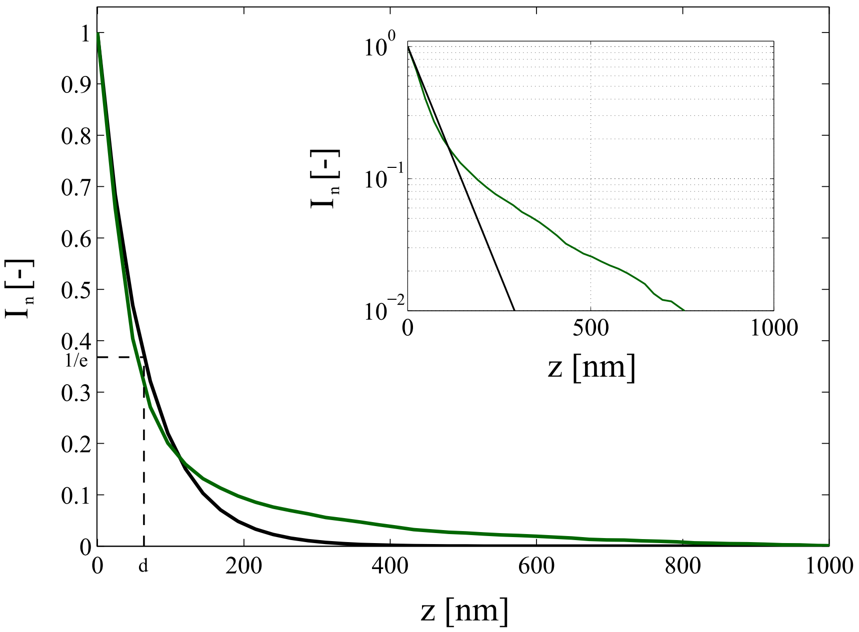

Figure 3.7: Normalized intensity I_n as a function of distance z of the evanescent field in TIR excitation as measured by a combined TIRFM-AFM setup (green). The curve was obtained by moving a fluorescent particle in the evanescent field while recording its intensity in water (similar to Sarkar et al., 2004) in order to validate the penetration depth for the incident angle setting. For the first 200 nm the agreement between experiment and theory (black) is good, however beyond 200 nm deviations arise which is likely due to background noise of the camera.

3.8 Conclusion and recommendations

Although, the results were very difficult to obtain, the assumption of operating at the maximum incident angle setting for the laser was validated. However, a point of concern remains, namely the reproducibility of the intensity versus distance curves.

Many attempts have been made to improve these results (e.g. using slightly thicker coverslips, an immersion oil with a lower viscosity, and improved clamping of the coverslip including preloading it), however a complete discussion is beyond the scope of the thesis. Nevertheless, the sample-scanner is likely the cause of the irreproducibility. As explained earlier, the intensity of the fluorescent particle is a function of its distance between the substrate for a given system. This distance can be controlled by either moving the substrate (as in a sample-scanner) or the particle (as in the case of a tip-scanner) up and down. Since the AFM-head of the AIST-NT system is equipped with a sample-scanner, the intensity field is also moved when making steps in z-direction, while the particle remains in the focus-plane of the objective. Although, the displacement is in the order of 1 μm, it is likely that the system is not fully decoupled due to the presence of the immersion lens.

To fully decouple the sample and the immersion lens a tip-scanner instead of a sample-scanner is recommended.

Chapter 4

Measurement Technique and Validation*

Up to now, no experimental technique exists that is capable of performing measurements of a dynamic contact line at nanoscale level. In this chapter, a measurement method that is based on Total Internal Reflection Fluorescence Microscopy (TIRFM) in order to study a nanoscale contact line is described. The method uses the intensity distribution resulting from total internal reflection of incident light, and the value for the penetration depth of the evanescent wave. The methodology and data processing to reconstruct the nanoscale interface from the obtained intensity distributions are described. It is demonstrated that the reconstructed interface of a droplet based on TIRFM is in good agreement with the interface obtained from non-disturbing AFM-imaging and conventional contact angle measurement. Moreover, the range of TIRFM in combination with sufficient temporal resolution, makes it possible to study moving contact lines at nanoscale level.

4.1 Interface reconstruction by TIRFM

The novel approach that is proposed here for obtaining the contact angle of a partial wetting droplet at a nanoscale is based on TIRFM (Franken et al., 2010, 2013). In particular, the technique relies on the fact that the illumination, confined to the region close to the surface, has a well-defined intensity decay. This particular kind of illumination is explained in the previous chapter, whereas a more detailed description of this microscopy technique and several applications for cell imaging are given by Axelrod et al. (1984). By adding a fluorescent dye to a droplet, the local fluorescent signal can be used to determine the local droplet height. This technique requires exact knowledge of the penetration depth. For a given system, the penetration depth is a function of incident angle only (Equation 3.3).

---

*The content of this chapter has been published in modified form in *Optics Express* (Franken et al., 2013).

Since the incident angle is difficult to obtain accurately, the penetration depth is calibrated by combined TIRFM-AFM (see Chapter 3). This characterization was done in order to validate the maximum incident angle setting in demineralized water (refractive index equals 1.3320 ± 0.0005 at 22 °C). Water is chosen as a working fluid for this calibration, because it is compatible with the fluorescent particle (and the adhesive attaching the particle to the cantilever), as well as the optics of the liquid scanner of the AFM-head.

The result for the experimentally determined penetration depth $58 \pm 4\ nm$ (see Figure 3.7) is in good agreement with a theoretically predicted penetration depth of $63\ nm$ for θ_{max} in water (estimated using the effective NA of the system). During the experiments, we keep the incident angle at this maximum angle (θ_{max}), yet replace the fluid. As we know the value of the refractive index of the fluid (hexaethylene glycol (HEG), $n = 1.4620 \pm 0.0005$), we can use Equation 3.3 to determine the value of the penetration depth of this medium ($d = 147\ nm$), and for the experiments in different working fluids described in the remainder of the thesis.

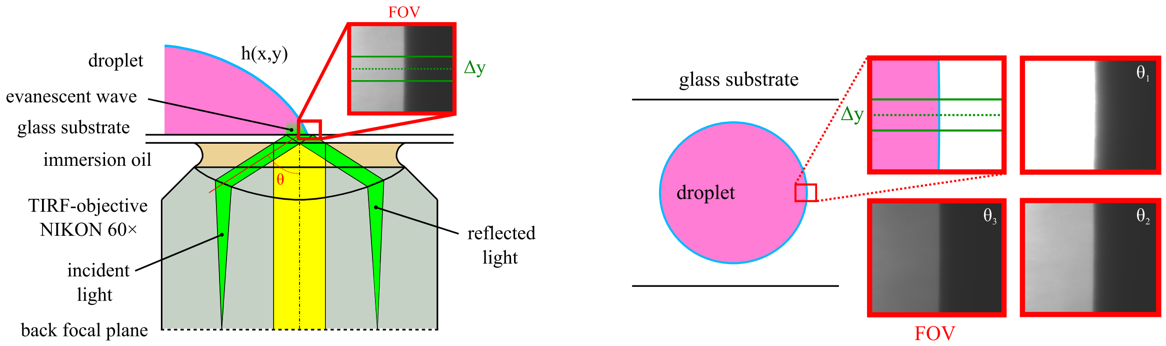

(a) (b)

Figure 4.1: (a) Schematic of the measurement of the intensity profile at the interface of a partial wetting droplet, (b) contour of illuminated millimeter-sized hexaethylene glycol droplet with field of view (FOV), not to scale.

By using a high-magnification objective, the field of view (FOV) is small compared to the radius of the droplet. This allows us to average the intensity distribution over a number of pixels (typically 10) along Δy, without the need for introducing a polar coordinate system, as illustrated in Figure 4.1a. The recorded images (typically 250, see Section 4.4) of the edge of a HEG droplet were processed in order to obtain a curve of the intensity profile along the edge of the droplet, as shown in Figure 4.1b. At the edge of the droplet, the imaged intensity profile is a function of spatial coordinates (x, y). The imaged or recorded intensity in gray values (per pixel) $I_{im}(x, y)$ is used together with the nominal value of the penetration depth of the evanescent field to convert this intensity profile to an interface height $h(x, y)$. The recorded intensity follows from the integral of the evanescent intensity (that excites fluorescence) along the optical (z-) axis at each (x, y) point. For clarity, we omit the dependence on (x, y), it follows

$$I_{im} = \int_0^{\infty} \mathcal{I}(z)\, dz\,, \tag{4.1}$$

where $\mathcal{I}$ is the intensity per unit length integrated over the pixel area, and is proportional to the image gray value. By substituting Equation 3.2 and splitting the integral at the local surface height $h(x,y)$ at the edge of the droplet, it follows

$$I_{im,edge} = \int_0^{h(x,y)} \mathcal{I}_0\, e^{-z/d}\, dz + \int_{h(x,y)}^{\infty} \mathcal{I}_0\, e^{-z/d}\, dz\,. \tag{4.2}$$

Any light collected on the CCD of the camera can only result from fluorophores, which are only present in the droplet (see Figure 4.2a). The second term on the right-hand side is therefore zero. Evaluating the integral in Equation 4.2 gives an expression for the imaged intensity at the droplet edge

$$I_{im,edge} = \mathcal{I}_0\, d\left[1 - e^{-h(x,y)/d}\right] + I_{im,background}\,, \tag{4.3}$$

with d the penetration depth of the evanescent field and $I_{im,background}$ the equivalent intensity due to dark background current of the image sensor of the camera. The $I_{im,background}$ term originates from the conversion of light intensity on the CCD to a gray value (Adrian and Westerweel, 2010). The value for $I_{im,background}$ can be obtained from parts of the image that are known to be sufficiently far away from the droplet edge (e.g. the far right in the images of Figure 4.1b) or by recording a separate set of images. By recording the intensity in the bulk of the droplet $I_{im,bulk}$, which is the region where the interface h is much larger than the penetration depth d (i.e. $h \to \infty$ effectively), $\mathcal{I}_0$ can be determined using

$$\mathcal{I}_0 = \frac{I_{im,bulk} - I_{im,background}}{d}\,. \tag{4.4}$$

Note that $\mathcal{I}_0$ is a function of (x,y) and Equation 4.4 thus takes care of non-uniform illumination effects; in a correctly aligned TIRF-microscope, the evanescent illumination has an elliptical Gaussian intensity profile (Axelrod et al., 1984). The interface of the droplet $h(x,y)$ is determined by substituting Equation 4.4 in Equation 4.3 and rewriting this to

$$h(x,y) = -d\,\ln\left[1 - \frac{I_{im,edge} - I_{im,background}}{I_{im,bulk} - I_{im,background}}\right]\,. \tag{4.5}$$

By measuring this intensity profile and the change in intensity of fluorophores in a partial wetting droplet, as illustrated in Figure 4.2b (for different incident angles), the nanoscale interface can be determined using Equation 4.5. When $I_{im,edge} = I_{im,bulk}$ Equation 4.5 diverges.

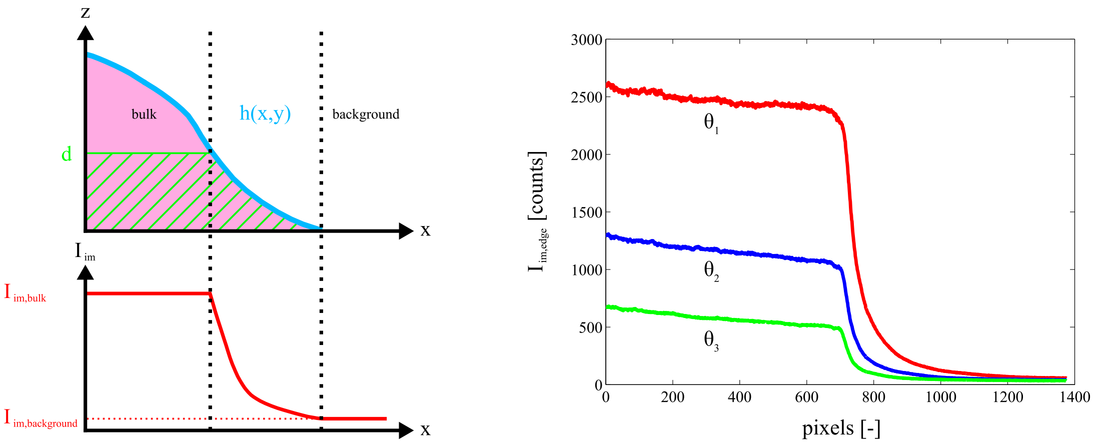

(a) (b)

Figure 4.2: (a) Interface detection of a partial wetting droplet using an evanescent excitation field and the resulting intensity profile, (b) intensity profiles $I_{im,edge}$ averaged over a number of pixels along Δy for different incident angles ($\theta_1 < \theta_2 < \theta_3$) ranging from small to large angles (beyond the critical angle).

4.2 Validation by non-disturbing AFM-imaging

Imaging by Atomic Force Microscopy (AFM) is well known for its unprecedented resolution and accuracy in the scanning of surfaces. The scanning range attainable in z is in the order of μm with nm accuracy, and therefore suitable as a reference for the TIRFM measurements. The following subsections briefly explain the principles of AFM.

4.2.1 Atomic Force Microscopy

AFM has the ability to image details at the atomic and molecular level, and is widely applied in research fields such as materials science, life science, polymer science, nanotechnology and biotechnology.

An AFM-head consists of a tip- or sample-scanner (a combination of these two is possible as well), a laser-feedback system, and a probe holder, as shown in Figure 4.3.

Operating principles

Atomic Force Microscopy relies on the detection of attractive and repulsive forces (long and short range respectively) in different operating modi. These forces are detected with the sharp tip of a sensor called an AFM-probe, and allow to determine a three-dimensional image of the surface topography while scanning the surface using the tip-surface interaction.

The probe is basically a micro-sized cantilever with a very small tip underneath it. Such an AFM-probe comes in different tip shapes (e.g. sharp or spherical) and cantilever geometries (e.g. triangular or rectangular), properties (e.g. length, stiffness, and resonance frequency), and can be provided with a reflex coating (e.g. gold or aluminum) to enhance the signal.

A laser diode (typically with a red visible wavelength) is focused on the back of the cantilever and reflected towards the photo-detector of a Position Sensitive Device (PSD). The laser light is used to measure the deflection of the cantilever while it scans the surface. By operating the system in a feedback control loop, it is possible to maintain a constant distance between tip and surface or a constant force (which is explained below).

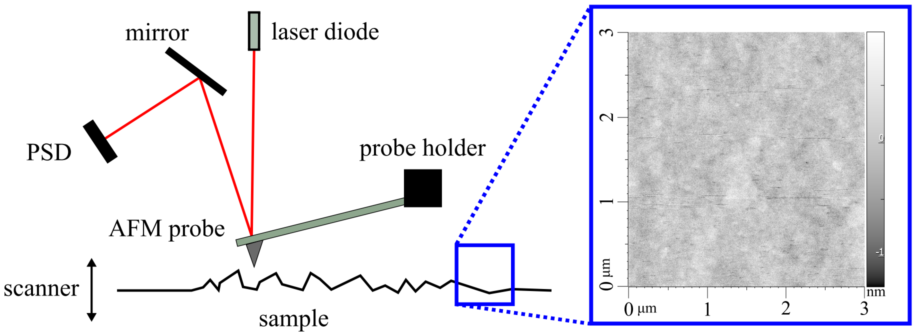

Figure 4.3: Schematic of atomic force microscopy. The inset shows the surface topology (with gray value proportional to surface height) of a glass surface (see text).

Using the above described approaches, surfaces can be imaged or characterized down to a molecular level. Depending on the characteristics of the sample, different operating modi can be chosen in order to characterize the surface. Each operating modi has its own characteristics, and each is briefly described below. A more detailed and complete description of AFM techniques is given by Eaton and West (2010).

Contact mode

In contact mode AFM, the tip makes soft physical contact with the surface of the sample. This contact causes a deflection of the cantilever, which is measured by the change in voltage of the PSD in the feedback system of the AFM-head. The deflection of the cantilever can be related to the spring force via Hooke's law, making it possible to measure surface forces. For this it is important to choose a cantilever that is soft enough to be deflected by small forces, but is strong enough to be resistant against vibrational instabilities (when scanning at relatively high rates).

Surface topography can be obtained in either a constant-height mode or constant-force mode. In the constant-height mode, the tip-sample distance is kept constant by controlling the motion of the scanner in z-direction. Whereas, in the constant-force mode, the force is kept constant during a surface scan by maintaining a constant deflection of the cantilever.

Non-contact mode

In contrast to contact mode, the tip does not contact the sample surface in non-contact mode. In this mode, the cantilever is driven to oscillate at a frequency equal to or slightly higher than its resonant frequency. This excitation causes the cantilever to oscillate with a certain amplitude of typically 10 nm. When the tip-sample-distance is large enough, the tip oscillates with a constant amplitude. However, when the tip approaches the surface of the sample, long or short-range forces cause the resonant frequency to decrease. The feedback loop of the system detects this decrease in resonant frequency, and tries to maintain a constant oscillation amplitude or frequency by adjusting the tip-to-sample distance. By measuring the displacement required to maintain a constant oscillation amplitude or frequency at each data point (x, y), a topographic image of the sample surface is reconstructed. For example, a 3×3 μm^2 surface scan of a glass substrate is shown in the inset of Figure 4.3.

The advantage of non-contact mode AFM is that the sample does not suffer from degradation, making non-contact mode AFM preferable for soft samples such as a droplet. Furthermore, contamination and wear of the tip do not occur, since there is no contact between tip and sample. However, significant differences in results can arise between contact and non-contact AFM. For example, when a wetted surface is scanned in non-contact mode, the tip will oscillate above the surface and therefore not penetrate the surface. Whereas, in contact-mode the tip will penetrate the liquid layer and touches the surface, instead of forming a small meniscus due to surface tension. This meniscus formation is a distortion of the liquid surface, and was estimated to be less than 5 nm by Mugele et al. (2002).

Tapping mode

In tapping or intermittent contact mode surface topography is obtained by gently tapping the surface with an oscillating tip. The tip contacts the surface at the end of the deflection of the cantilever, and therefore exerting less force on the sample. This causes less damage to the surface compared to contact mode.

4.2.2 AFM-imaging of droplet interface

AFM-imaging of liquid droplets deposited on a substrate is only possible under strict conditions, such as a pinned contact line (hence a non-moving droplet interface) of a viscous droplet with high surface tension. By operating the AFM-head in non-contact mode, the interface of a partially wetting droplet can be measured without perturbing it. In non-contact mode, the cantilever is driven to oscillate at its resonance frequency. The oscillating amplitude is kept constant in a feedback loop of the system, by changing the distance between tip and sample as it scans the interface of the droplet. A detailed procedure of AFM-imaging of very small droplets is provided by Fery et al. (1999); Herminghaus et al. (2000); Mugele et al. (2002); Checco et al. (2003).

4.2.3 AFM probes

The shape of the droplet interface was determined using commercial ATEC-NCAu ($160 \times 46 \times 4.6\ \mu m^3$) non-contact (or tapping) mode cantilevers with a tetrahedral tip (with a height of $\approx 15\ \mu m$) that protrudes from the very end of the cantilever. This particular kind of tip-geometry was required in order to avoid cantilever-sample interaction, as illustrated in Figure 4.4. The cantilevers had a typical resonance frequency of 335 kHz and a tip radius of about 63 nm according to the supplier (NanoAndMore GmbH, Wetzlar, Germany). Furthermore, the geometry of the tip has the advantage that acoustic effects due to viscous damping are minimized. These effects can cause additional damping and thus affect the amplitude of oscillation, and therefore the accuracy of surface determination (Fontaine et al., 1997).

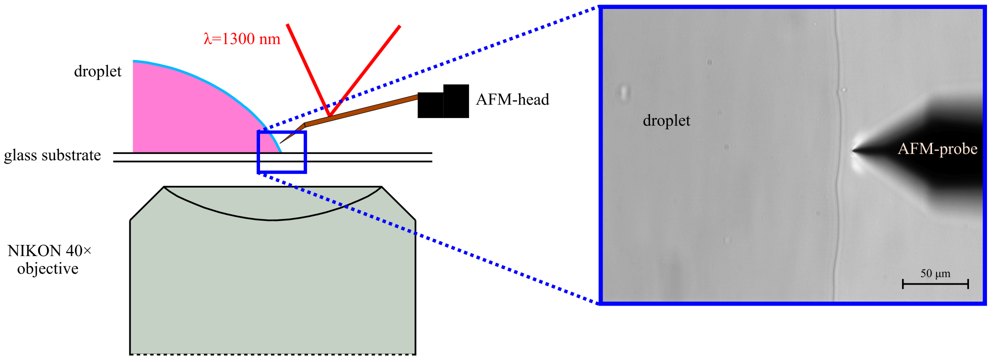

Figure 4.4: Schematic of non-disturbing AFM-imaging of a droplet interface.

The tip at the cantilever is positioned with respect to the droplet edge with the aid of an imaging system, as shown in the inset of Figure 4.4. For this purpose, an objective with a magnification of 40× (Nikon APO40×/0.60) was used.

4.2.4 Working fluid

In order to avoid significant evaporation of the droplet in the timescale of the set of experiments (typically less than a hour), a liquid is required that has a sufficiently low vapor pressure at room temperature (i.e. non-volatile under ambient conditions). Furthermore, high surface energy is desirable in order to have stable AFM-imaging conditions for the validation study, as noted by Mugele et al. (2002).

The TIRFM measurements, that are the focus of the overall project, do not require these strict conditions, because the time required for the measurement is much shorter than AFM-imaging, and it uses the intensity distributions instead of tip-sample interaction. Any fluid with a fluorescent dye will work for TIRFM as long as the refractive index is smaller than that of the glass substrate. The intensity distributions as well as the interface scans are obtained from a HEG droplet (Sigma-Aldrich, Saint Louis, MO, USA) with a Rhodamine B fluorescent dye (Sigma-Aldrich, Saint Louis, MO, USA). It should be noted that for the interface determination with both methods, the same droplet is used.

The fluorescent dye has a concentration of $O(10^{-4}\ mol/liter)$. The concentration is adjusted in such a way that for large incident angles sufficient intensity remains, but self-absorption remains negligible. Therefore, measurements with sufficient signal-to-noise ratio were possible. Furthermore, an Abbe refractometer is used to determine the refractive index of HEG with and without Rhodamine B and equals 1.4620 ± 0.0005 in both cases. Note that all the measurements were performed in ambient conditions at room temperature (around 22 °C) and a relative humidity of about 40%.

4.3 Results

The experiments were done for different partial wetting conditions, which were obtained by preparing the glass substrates differently, such that two different macroscopic contact angles were measured. The reconstructed interface of a partial wetting droplet by TIRFM is shown in Figure 4.5, and clearly shows the different length scales involved (note that we have a ratio of 1000 between the scales of the axes). The results were obtained by illuminating a partial wetting droplet by an evanescent excitation field with a nominal penetration depth of 147 nm (see Figure 3.1b). This value was obtained using Equation 3.3 for the maximum incident angle (θ_{max}) validated using a calibrated intensity versus distance curve in water, as described in Section 3.7. A clear saturation of the fluorescent signal is represented as the horizontal part (i.e. $x = 0$ to 2.1 μm in Figure 4.5a) of the interface that approaches the penetration depth.

Photobleaching is expected to have a negligible effect on the results (as explained in detail in Section 4.4), because only a fraction of the 150 mW laser power is used for excitation due to the fiber coupling and nature of the evanescent wave. Furthermore, the results from non-disturbing AFM-imaging and conventional contact angle measurement using the side view of the droplet (CA_{macro}) are also plotted in Figure 4.5. Multiple measurements on several sides of the droplet were conducted in order to ensure that the experimental data is representative. A direct comparison between the reconstructed interface with the different measurement techniques shows that these are in good agreement. Possible influence of, for example, reflections at the interface are therefore negligible. The scatter in the reconstructed interface by AFM-imaging is on the order of several nm, and is likely caused by the tip sticking to the droplet interface. The fluctuations in the measured values of the interface reconstructed by TIRFM are in the order of *nm* as well.

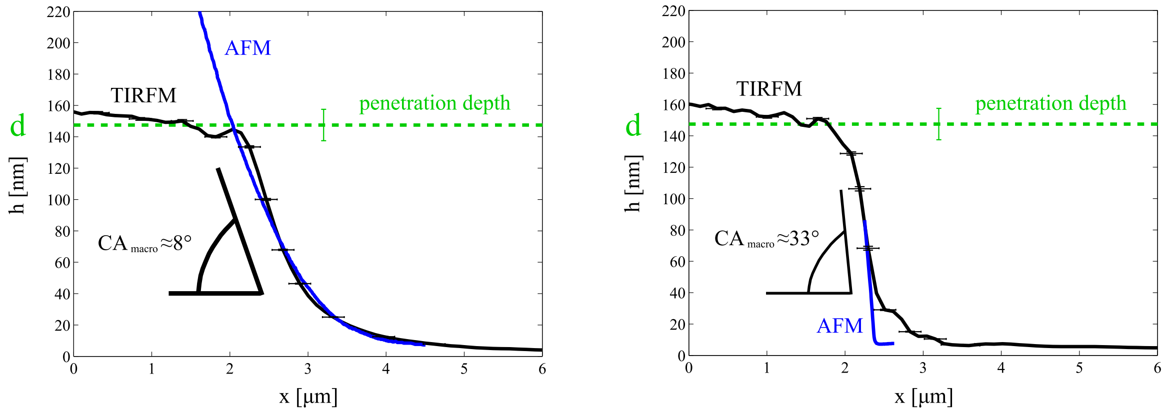

(a)

(b)

Figure 4.5: Nanoscale interface height h (as a function of the distance x with respect to an arbitrary reference point) of a partial wetting hexaethylene glycol droplet on different substrates with a macroscopic contact angle of (a) $8\,°$, (b) $33\,°$, as measured with a side view camera. In both cases the length of the precursor film is much larger than the PSF of the system (which is approximately 300 nm, see Section 3.4). An error of about 7% is expected for h due to the uncertainty in determination of the penetration depth d.

Figure 4.5a demonstrates that contact line visualization by TIRFM is in good agreement with AFM-imaging. Both techniques capture the shape of the nanoscale interface well at a relatively small macroscopic contact angle. However, at large contact angles AFM-imaging has difficulties following the interface of the droplet due to the transition from a very soft, inclined surface to a flat, hard surface, as can be seen in Figure 4.5b. Consequently, for larger contact angles the near-wall results deviate from TIRFM (i.e. $x = 2.4$ to 3.5 μm in Figure 4.5b), because TIRFM does not suffer from this transition since it relies on the fluorescent signal. As can be seen in Figure 4.5b, at approximately $h = 30$ nm the droplet interface changes from straight to curved due to perturbation by van der Waals interaction. This occurs for both contact angles, and is consistent between both TIRFM measurements. However, no direct comparison with other experimental data for a partial wetting fluid is currently possible. This is because there is no data available of the measured interface below 30 nm for a partial wetting fluid.

Similar to Hoang and Kavehpour (2011), the precursor film profile was measured using fluorescence microscopy. However, the deviations in the effect of van der Waals forces on the measured interface are contributed to a different working fluid, partial wetting and an adiabatic instead of a diffusive regime. It should be noted that the purpose of this chapter is the description of the developed measurement technique and its validation by AFM-imaging. Further discussion of wetting phenomena is beyond the scope of this chapter, and will be discussed in the following chapters.

4.4 Sensitivity analysis

This section describes a sensitivity analysis of several parameters on the reconstructed nanoscale interface by the developed measurement technique for the case of a non-moving droplet.

Image averaging is done in order to improve the signal-to-noise ratio on the images due to noise of the CCD (photon noise, dark noise and read noise). This works only on the assumption that the noise in the images is truly random. In this way, random fluctuations above and below actual image data will gradually even out when averaged over more and more images. Figure 4.6a illustrates that averaging significantly reduces the fluctuations on the nanoscale interface. Furthermore, the results show that a nanoscale interface reconstructed using an average of 250 images does not significantly differ (i.e. less than 0.1 *nm*) from a reconstructed interface averaged over 500 images, meaning that 250 images is sufficient for the present purposes. All the recordings were obtained with an exposure time of 30 *ms* and without pixel binning (i.e. 1×1), unless specified otherwise.

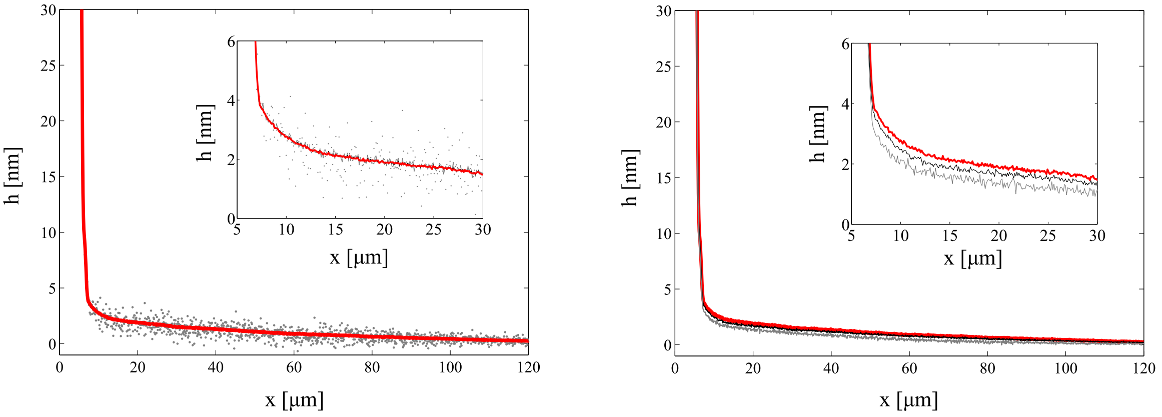

(a)

(b)

Figure 4.6: Nanoscale interface height h (as a function of the distance x with respect to an arbitrary reference point) of a partial wetting hexaethylene glycol droplet (a) averaged over different numbers of images: 1 image (dots), 50 images (gray), 250 images (black) and 500 images (red), (b) obtained with different camera exposure times of 30 *ms* (red), 20 *ms* (black) and 10 *ms* (gray).

By increasing the exposure time, more light is collected on the CCD which improves the signal-to-noise ratio. However, long exposure times (in combination with a continuous wave laser) also reduce the recording rate. In particular, the recording rate is of importance for moving droplet interfaces, which are described in Chapter 5. Figure 4.6b illustrates no significant difference (approximately 0.4 nm as shown in the inset of Figure 4.6b) exists between an interface recorded with exposure times of 20 and 30 ms respectively. However, at an exposure time of 10 ms results of the interface height h start to deviate more, namely approximately 0.8 nm, and increase the noise level slightly. Therefore, a 10 ms exposure time is considered too short to accurately measure the droplet interface.

In the context of image processing, pixel binning is the procedure of combining a cluster of adjacent pixels into a single pixel. For instance, in 4×4 binning an array of 4 pixels becomes a single larger pixel and increases the intensity in the resulting with a factor of (about) 4. Binning therefore increases the signal-to-noise ratio (SNR) at the cost of spatial resolution. Figure 4.7a compares the nanoscale interface of a droplet when 4×4 pixel binning is applied (in combination with a reduction of laser intensity by a factor of 16) with an interface obtained when no binning (i.e 1×1) is applied.

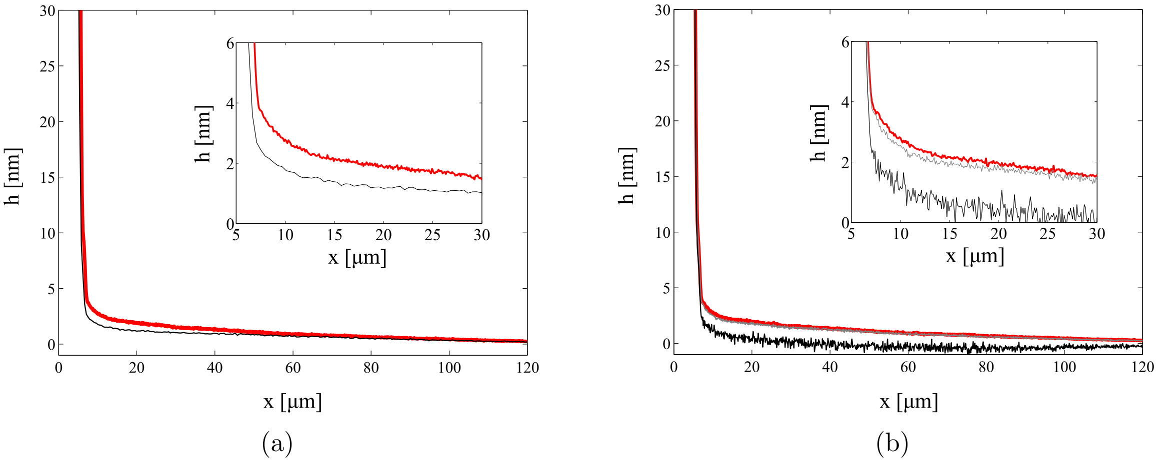

Figure 4.7: Nanoscale interface height h (as a function of the distance x with respect to an arbitrary reference point) of a partial wetting hexaethylene glycol droplet obtained with (a) different hardware binning: 1×1 (red) and 4×4 (black), and (b) different laser intensity levels of 100% (red), 50% (gray) and 12.5% (black) of the maximum laser output level for the excitation of the fluorescent dye.

Figure 4.7a demonstrates that a reduction in spatial resolution is not necessarily an issue, since the shape of the droplet interface is captured very well. For example, the droplet interface is not stretched, but deviations exist (approximately 0.8 nm) because the laser intensity was reduced by a factor of 16. This was done in order to maintain the same gray value in the image. Consequently, the reduction of the laser intensity by a factor of 16 causes a loss of information in the background noise of the CCD, which is beneficial to the accuracy of the final result.

When using fluorescence microscopy for quantitative measurements (of the nanoscale interface h, which is the purpose of the developed technique), it is crucial to avoid photobleaching. Photobleaching occurs when a fluorophore permanently loses its ability to fluoresce, which is typically caused by photon-induced destruction (Hoang and Kavehpour, 2011). When photobleaching is present, a quantitative measurement of a nanoscale interface is complicated, because the developed technique uses the intensity of the fluorescent dye for the interface reconstruction, as described in Section 4.1. Nevertheless, photobleaching can be reduced by limiting the exposure time of fluorophores to illumination, reducing the dye concentration, or by lowering the excitation energy of a laser source. However, these precautions also reduce the signal-to-noise ratio (SNR) as evidenced by the previous tests. Another option, which is not considered in this study, is to use a more robust fluorescent dye that is less prone to photobleaching (see Hoang and Kavehpour, 2011).

In Figure 4.7b it can be seen that no significant difference in interface height h (i.e. smaller than 0.2 nm) exists between an interface reconstructed using the intensity profiles excited with a reduction of 50 percent in laser power. This means that the fluorophores still emit enough light to overcome the background noise level of the camera, and thus a significant valu for the interface height h is measured. However, when only 12.5 percent laser power intensity is used, the fluorophores do not emit enough light to overcome the background noise.

In order to see if any effect on the measured droplet interface h due to photobleaching is present, a very long recording of 1000 images at a recording rate of 1 Hz is done (i.e. about 20 minutes). This is illustrated in Figure 4.8 in which a comparison of a nanoscale interface height h based on the first and last image of a recording of 1000 images in total is made. Both the nanoscale interface obtained from the first and last image agree very well with the interface averaged over the total amount of images. From this result it is evident that photobleaching does not occur or does not affect the measurements. This is expected, because in evanescent wave based illumination only a fraction of the laser intensity is used for the excitation of the fluorescent dye.

4.5 Conclusion and outlook

The results presented in this chapter demonstrate that TIRFM is able to reconstruct the interface of a partial wetting droplet at nanoscale level. Moreover, the results are in good agreement with the results from non-contact AFM-imaging. Furthermore, the sensitivity analysis indicates that the technique is not sensitive to photobleaching. By using short exposure times $O(ms)$ TIRFM is not limited to reconstructing static interfaces at nanoscale level in the case of a pinned droplet edge. Hence, with this technique it now becomes possible to study the fundamental behavior of a dynamic interface of a partial wetting droplet at nanoscale level. The study of a dynamic interface at mesoscopic level is dealt with in Chapter 5.

In the context of attainable measurement range and accuracy of the method, the surface determination also decreases with surface height, the use of multiple penetration depths for a single measurement enhances the dynamic range of the method. The use of variable beam incidence was proposed by e.g. Loerke et al. (2003) and Stock et al. (2003). For example, the penetration depth ranges from about 147 nm for hexaethylene glycol to about 500 nm

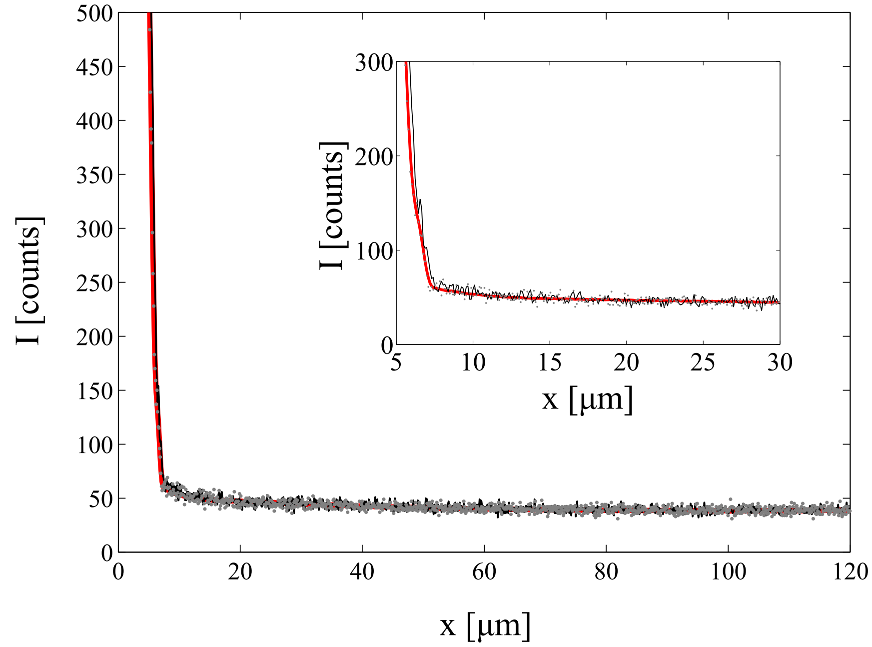

Figure 4.8: Intensity distribution $I_{im,edge}$ at the edge of a partial wetting hexaethylene glycol droplet (radius $\approx 1.5\ mm$) obtained with an average over 1000 images (red), whereas the first image ($t = 0$) and last image ($t = 20\ min$) of the recorded data set are plotted as a gray solid line and gray dots respectively. The inset shows a close-up of the fluorescence intensity at the edge of the droplet.

for small incident angles (beyond the critical angle), as shown in Figure 3.1b. In addition, the use of multiple incident angles (beyond the critical angle), hence illuminated sections, can be promising to improve current velocimetry techniques based on evanescent wave illumination, as explained in Appendix B. However, the penetration depth of the evanescent wave needs to be directly calibrated with nanometer accuracy in order to obtain quantitative information of these illuminated sections when the maximum incident angle is not used.

Chapter 5

Dynamics of Precursor Films of Partial Wetting Droplets[*]

This chapter describes the dynamics of precursor films of advancing and receding contact lines on smooth horizontal glass substrates using the developed measurement technique. This technique is based on total internal reflection fluorescence microscopy, and has sufficient spatial as well as temporal resolution to capture the interface at mesoscopic level at various contact line velocities (hence capillary numbers). A theoretical model has been developed and compared with the measurements of the advancing precursor film profile. Furthermore, the experimental results agree well with theoretical predictions based on a slip boundary condition at the solid surface. Moreover, the slip length is found to be proportional with the contact line velocity using the lubrication approximation.

5.1 Background of dynamics of precursor films

During the spreading of fluids, a microscopically thin film is formed ahead of the macroscopic contact line. This precursor film is formed by the so-called disjoining pressure that arises due to the presence of van der Waals forces (Derjaguin and Churaev, 1974).

Theoretical studies by e.g. de Gennes (1985) and Hervet and de Gennes (1984) have shown that the precursor film appears to be very important for droplet spreading, moreover its existence depends on van der Waals forces. Due to the presence of the precursor film, the thickness of the droplet interface does not go to zero, and it was shown that all the excess free energy is dissipated in the precursor film, and so the total energy dissipated from the apparent contact line motion is finite. Hence, the stress singularity at the macroscopic contact line is eliminated. Therefore, contact line motion cannot be discussed without incorporating these van der Waals forces.

---

[*] To be submitted in modified form as: M.J.Z. Franken, G. Ooms, C. Poelma, and J. Westerweel, *Precursor Films of Spreading Partial Wetting Droplets.*

The existing experimental results demonstrate the existence of a precursor film, but remain qualitative only in case of a moving precursor film. Therefore, there is no adequate comparison of experimental results with the complete theory for a moving droplet (de Gennes, 1985).

In case of an adiabatic precursor film, the lubrication approximation is used to derive a scaling of the film thickness of $1/x$ based on a no-slip condition at the solid surface (de Gennes, 1985). However, the no-slip boundary condition is incompatible from a kinematic point of view.

One way to relax the no-slip condition at the solid surface, is to introduce a slip velocity, which can also be characterized by a slip length. The scaling would then be $1/\sqrt{x}$ as proposed by Bruinsma (1990) and Brochard-Wyart et al. (1994). Hence, understanding the behavior of adiabatic films is key to understanding moving contact lines. In order to obtain more insight into the behavior of a moving precursor film, the developed measurement technique (as described in detail in Chapter 3) is utilized to assess the mesoscopic region of a droplet while it is spreading. For this purpose, the experimental setup for measuring the precursor film of a droplet (see Figure 3.4) is extended to be able to measure a moving contact line at mesoscopic level.

5.2 Experimental setup

In most macroscopic studies of the contact line or contact angle, the goniometer method is used, as shown in Figure 5.1a.

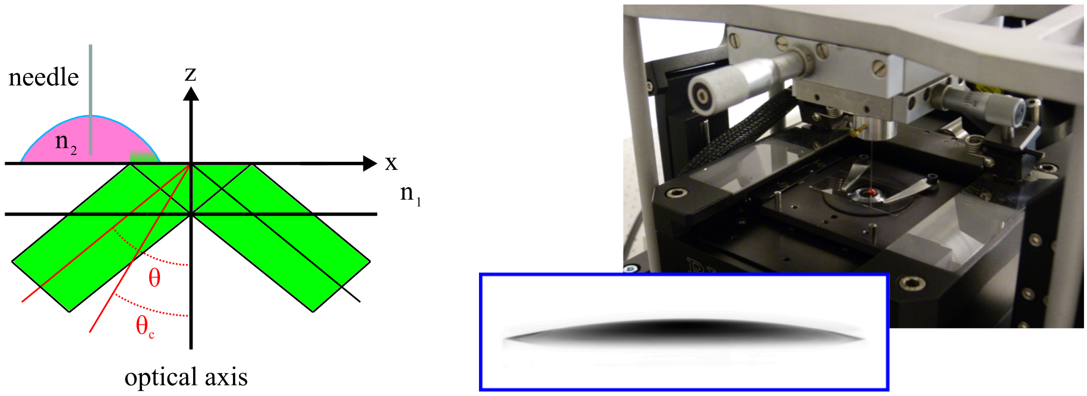

(a) (b)

Figure 5.1: (a) Schematic of droplet actuation and TIRF optical setup, (b) close-up of experimental setup showing the needle positioner. The inset shows the measurement of a partial wetting droplet (with $CA_{macro} \approx 12\,°$) by the side view camera.

In this method, an advancing contact angle is obtained by pushing a droplet out of a syringe onto a substrate. When more liquid is injected, the droplet will increase in volume, and the contact line obtains approximately a stationary motion when moving through the FOV.

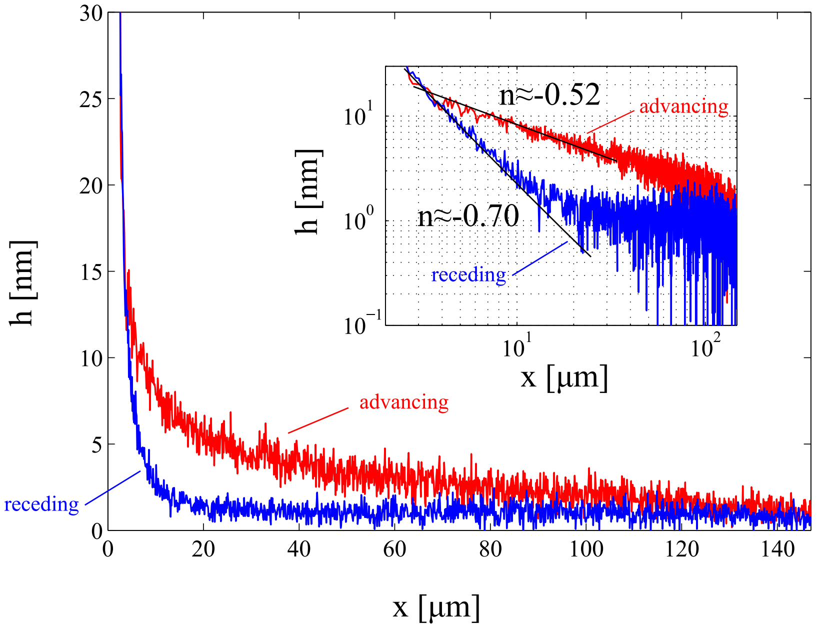

Figure 5.2: Snapshot of an advancing (red) and a receding (blue) precursor film profile of a stationary moving glycerol interface recorded at a rate of about 20 *Hz*.

The receding contact line is measured by extracting liquid out of the droplet through the needle into the syringe. The droplet will decrease in volume, while the contact line motion is stationary. An axisymmetric shape of the droplet is maintained by placing the needle in the center of the droplet, as a result the liquid profile is a function of coordinate x only. By using a very high magnification for imaging of the droplet edge, the field of view (FOV) is small compared to the radius of the droplet (see Figure 4.1b), which allows the reduction of the problem to two dimensions only, namely x and z (see Appendix A).

However, an extension of the setup was required to obtain an advancing and a receding contact line. The extension is mounted on top of the base-plate of the AFM-head, as shown in Figure 5.1b, and includes a xy-stage to position the needle in the droplet (glycerol with Rhodamine B, refractive index $n = 1.4340 \pm 0.0005$). The fluid was smoothly delivered by a syringe pump (neMESYS, cetoni GmbH, Korbussen, Germany) in combination with a 1 *ml* glass syringe (Fortuna Optima, Poulten & Graf GmbH, Wertheim, Germany), to prevent stick-slip effects of the piston inside of the syringe tube. The fluid was delivered via a hubless needle (Hamilton Bonaduz AG, Switserland) in the droplet. The needle had inner and outer diameters of 0.260 and 0.515 *mm* respectively, according to the supplier specifications. Furthermore, the presence of the needle did not affect the macroscopic shape of the droplet due to local curvature of the contact line.

It should be noted that the measurements are conducted within a relatively short time scale. Therefore, we assume that during the motion of the meniscus (hence contact line), only motion due to the applied pressure difference arises, and not due to evaporation of the liquid as well as the absorption of moisture from the environment by the working fluid (hygroscopicity).

Figure 5.2 shows the advancing and receding precursor film when it moves at an effectively steady rate through the FOV. The stationary motion of the contact line (for very small Reynolds numbers, such that $Re \ll 1$) is validated, and shown for an advancing contact line in the inset of Figure 5.3.

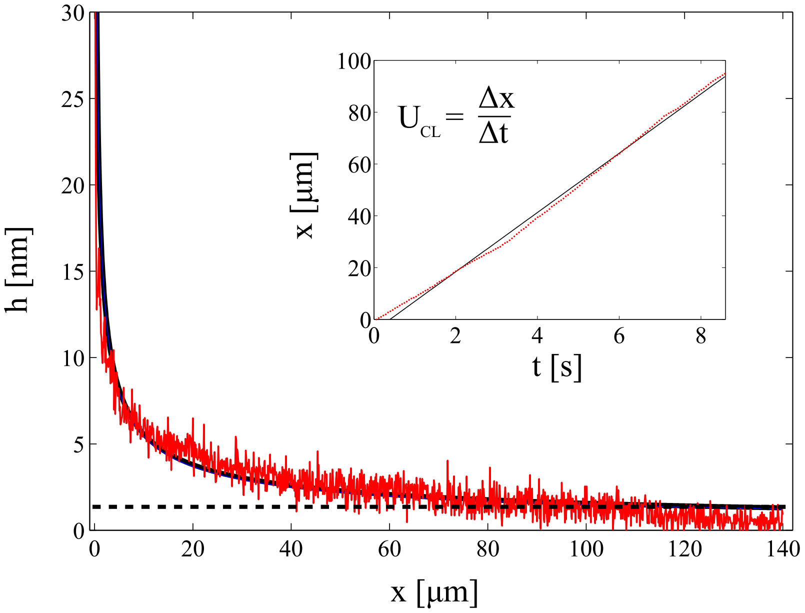

Figure 5.3: Advancing precursor film (red) moving with a contact line velocity $U_{CL} = 11.44 \pm 0.11\ \mu m/s$, and its power-law fit (black) with an exponent $n = -0.55 \pm 0.01$. The inset shows the displacement of the contact line over time, and indicates a constant motion.

5.3 Theoretical model

In partial wetting, the droplet makes a finite macroscopic contact angle with the dry solid in equilibrium, and the disjoining pressure Π as function of the precursor film thickness h can be written in the following form (Starov et al., 2007)

$$\Pi = \frac{A}{6\pi\, h^3} - C_1\, e^{-h/C_2}\,. \tag{5.1}$$

The first term on the right-hand side represents the long-range van der Waals force, whereas the second term represents the short-range force due to (for instance) steric or electrical interactions. A is the effective Hamaker constant, and C_1 and C_2 are constants. The physical meaning of C_2 is the correlation length of water molecules is aqueous solutions, and is $\sim 10\mathring{A}$, which is the characteristic thickness of the hydration layer (Starov et al., 2007). For $A = 2.8 \times 10^{-20}\,J$, $C_1 = 2.5 \times 10^5\,J/m^3$ and $C_2 = 5.0 \times 10^{-10}\,m$ the disjoining pressure is given in Figure 5.4. The van der Waals force is dominant from $h > 2.0 \times 10^{-9}\,m$. The short-range force is dominant between $h = 0$ and $h = 2.0 \times 10^{-9}\,m$ and negligible thereafter. A more detailed discussion of partial wetting at equilibrium is given by Brochard-Wyart et al. (1994) and de Gennes et al. (2004).

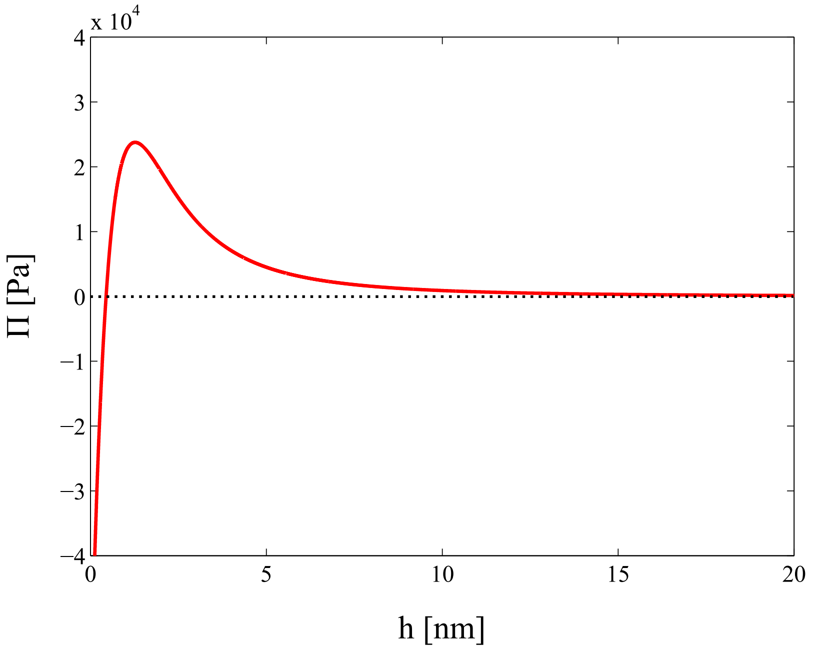

Figure 5.4: Disjoining pressure Π as a function of the precursor film thickness h.

A theoretical model is developed to predict the behavior of a mesoscopic contact line of a partially wetting droplet, and validated with the experimental results. This model is used to study this dynamic problem for the case that the contact line is advancing with a certain velocity U_{CL}. During the experiments, it is found that a precursor film is formed ahead of the spreading droplet. A sketch of the film up to the steep, rising part of the droplet is shown in Figure 5.5.

In the theoretical model a frame of reference is chosen, in which the droplet and precursor film are at rest. Thus the solid substrate is moving with a constant velocity U_{CL} to the left for the orientation shown in Figure 5.5, and exerts a viscous friction on the precursor film in that direction. The x-coordinate is chosen along the solid wall, and x increases to the right as defined in Figure 5.5. The z-coordinate is normal to the wall and $z = 0$ at the wall. Furthermore, it is assumed that the liquid flow in the precursor film can be treated as a continuum in order to solve the flow equations. Alder and Wainwright (1970) showed that the continuum hypothesis is already valid from 3 molecular distances. Close to the end part (the tip) of the precursor film the main forces that act on the film are the viscous

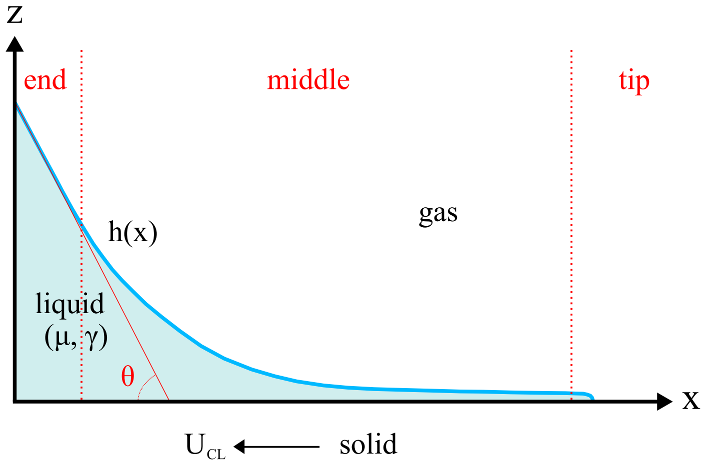

Figure 5.5: Sketch of the precursor film up to the steep, rising part of the droplet, where U_{CL} is the contact line velocity, μ is the dynamic viscosity of the liquid, and γ is the surface tension between liquid and gas.

force and the short-range force. In the middle part the viscous force and the van der Waals force are dominant. Close to the steep, rising part of the precursor film the viscous force, the van der Waals force and the force due to surface tension are important.

The following simplified equation of motion (see Appendix A for a complete derivation) is solved

$$\mu \frac{\partial^2 u}{\partial z^2} - \frac{\partial p}{\partial x} = 0\,. \tag{5.2}$$

The flow patterns are approximately parallel between the free surface and the solid substrate (Kim, 2013). Therefore, the cross-sectional flow structure as in Figure A.1a is assumed, hence a two-dimensional geometry. For $z = 0$ it is assumed that $u = U_{CL} - U_{slip}$. At the top of the film there is no viscous shear force, so for $z = h$ the following condition holds $\partial u/\partial z = 0$. Solving Equation 5.2 using these boundary conditions, yields the following expression for the velocity

$$u = \frac{1}{2\mu}\frac{\partial p}{\partial x} z^2 - \frac{1}{\mu}\frac{\partial p}{\partial x} h\, z + U_{CL} - U_{slip}\,. \tag{5.3}$$

The volume flux J through the precursor film is then found to be

$$J = -\frac{1}{3\mu}\frac{\partial p}{\partial x} h^3 + (U_{CL} - U_{slip})\, h\,. \tag{5.4}$$

The slip length L_{slip} is defined in the following way $L_{slip} = -U_{slip}/(\partial u/\partial z)_{z=0}$ (Brochard-Wyart et al., 1994). Substitution of u gives the following relation between the slip velocity and slip length $U_{slip} = \frac{1}{\mu}\frac{\partial p}{\partial x} h\, L_{slip}$. (As $U_{slip} < 0$ and $\frac{1}{\mu}\frac{\partial p}{\partial x} h < 0$, $L_{slip} > 0$.) Substitution of U_{slip} in J gives

$$J = -\frac{1}{\mu}\frac{\partial p}{\partial x}\, h^2\,(h/3 + L_{slip}) + U_{CL} h\,. \tag{5.5}$$

As can be seen in Figure 5.5, the precursor film is closed at its tip (which occurs as long as C_1 and C_2 in Equation 5.1 are positive), meaning that there is no net flux ($J = 0$). This leads to the following equation

$$\frac{\partial p}{\partial x} = \frac{\mu\, U_{CL}}{h(h/3 + L_{slip})}\,. \tag{5.6}$$

The pressure gradient in the film arises due to the gradient of the surface tension force and the gradient of the disjoining pressure

$$\frac{\partial p}{\partial x} = \frac{\partial}{\partial x}\left[-\gamma \frac{d^2 h}{dx^2} - \Pi\right]\,, \tag{5.7}$$

where γ is the interfacial tension between the liquid and the gas. Combining Equations 5.6 and 5.7 yields

$$\frac{\mu\, U_{CL}}{h(h/3 + L_{slip})} + \gamma \frac{d^3 h}{dx^3} + \left[-\frac{A}{2\pi h^4} + \frac{C_1}{C_2}\, e^{-h/C_2}\right]\frac{dh}{dx} = 0\,. \tag{5.8}$$

Following de Gennes' approach (de Gennes, 1985), Equation 5.8 is made dimensionless by means of $x = x_0\,\tilde{x}$ and $h = h_0\,\tilde{h}$ with the scaling parameters $x_0 = 3^{-1/6} a\, Ca^{-2/3}$ and $h_0 = 3^{1/6} a\, Ca^{-1/3}$. $Ca = -\mu\, U_{CL}/\gamma$ is the capillary number and $a = [A/(6\pi\gamma)]^{1/2}$ is a molecular length scale ($O(10^{-10}\ m)$). After some straightforward mathematical operations the following equation is found

$$\frac{d^3\tilde{h}}{d\tilde{x}^3} = \frac{1}{\tilde{h}^2 + \alpha\, L_{slip}\,\tilde{h}} + \frac{1}{\tilde{h}^4}\frac{d\tilde{h}}{d\tilde{x}} - K_1\, e^{-\tilde{h}/K_2}\frac{d\tilde{h}}{d\tilde{x}}\,, \tag{5.9}$$

with $\alpha = 3^{5/6}\, a^{-1}\, Ca^{1/3}$, $K_1 = C_1\, a^2\,/(3^{1/3}\, C_2\, \gamma\, Ca^{4/3})$ and $K_2 = C_2\, Ca^{1/3}/(3^{1/6}\, a)$.

When the short-range force and the slip of the precursor film over the solid wall are not taken into account, Equation 5.9 reduces to the equation studied by (de Gennes, 1985). Equation 5.9 is solved by following his approach. Namely, the precursor film is divided into three parts, since each region has its own dominating forces. The middle part is the starting point, where Equation 5.9 can be approximated by

$$0 = \frac{1}{\tilde{h}^2 + \alpha\, L_{slip}\,\tilde{h}} + \frac{1}{\tilde{h}^4}\frac{d\tilde{h}}{d\tilde{x}}\,. \tag{5.10}$$

This equation has the following analytical solution

$$\tilde{h} = \frac{1 + (1 + 2\, L_{slip}\, \alpha\, \tilde{x})^{1/2}}{2\, \tilde{x}} \,. \tag{5.11}$$

After choosing the length of the x-region for the middle part, the thickness of the precursor film as a function of the coordinate $\tilde{x}$ can be calculated with Equation 5.11.

Furthermore,

- the middle part is by far the largest part of the precursor film. In that part the change in film thickness is so small that the force due to surface tension is negligible. Moreover, the short-range force is negligible, because the thickness of the precursor film is still too large (when compared with the range of the short-range force);
- Only in the tip part the thickness has decreased so much, that the short-range force becomes important and the thickness decreases quickly to zero.
- In the end part the film thickness increases with decreasing x. The van der Waals force decreases and the capillary force becomes dominant. The film thickness increases quickly with decreasing x and gradually goes over into the bulk of the droplet and leads to a macroscopic contact angle.

No analytical solutions are available for the equations in the tip part and the end part. In the tip part the following equation holds

$$0 = \frac{1}{\tilde{h}^2 + \alpha\, L_{slip}\, \tilde{h}} - K_1\, e^{-\tilde{h}/K_2} \frac{d\tilde{h}}{d\tilde{x}} \,, \tag{5.12}$$

and in the end part

$$\frac{d^3\tilde{h}}{d\tilde{x}^3} = \frac{1}{\tilde{h}^2 + \alpha\, L_{slip}\, \tilde{h}} + \frac{1}{\tilde{h}^4} \frac{d\tilde{h}}{d\tilde{x}} \,. \tag{5.13}$$

Equations (5.12) and (5.13) are solved numerically starting from the thickness of the middle part at one of the two end points of the middle part. The value of $A = 2.8 \times 10^{-20}\, J$ is obtained from a comparison between experiment and model predictions for the **middle part** ($1.5\, nm \leq h \leq 15\, nm$, see Figure 5.3). Although the measurement technique has sufficient resolution and accuracy to determine the shape of the precursor film, the tip cannot be attained. As a consequence, the *length* of the precursor film is left undetermined quantitatively, though the order (approximately $150\, \mu m$, see e.g. Figure 5.7) equals the one found by Kavehpour et al. (2003).

Furthermore, the measurement limit in film thickness is approximately $1.5\, nm$ (see dotted line in Figure 5.3), which is very close to a molecular limit. Therefore, it is estimated that this is the limit of the middle part of the precursor film. This limit is used as a basis for the disjoining pressure isotherm (see Figure 5.4), and thus the constants C_1 and C_2. It should be noted that this cutoff did not have a significant effect on the results, since these are part of the short-range term, and thus only closes the tip.

The constants $C_1 = 2.5 \times 10^5\ J/m^3$ and $C_2 = 5.0 \times 10^{-10}\ m$ have been chosen in such a way, that the transition from the long-range region to the short-range region in the disjoining pressure isotherm (Equation (5.1)) occurs at a film thickness h of the middle part takes place at $h \approx 1.5\ nm$.

Furthermore, the surface tension $\gamma = 0.0655\, N/m$ and viscosity $\mu = 0.0204\, Pas$ are experimentally determined using the Wilhelmy-plate method and a rheometer respectively. The contact line velocity $U_{CL} = 5.13 \times 10^{-6}\ m/s$ followed from image-analysis. The result is the dimensionless solution for the precursor film thickness $\tilde{h}$. Figure 5.7 shows the solution with dimensions, i.e. $h(x)$.

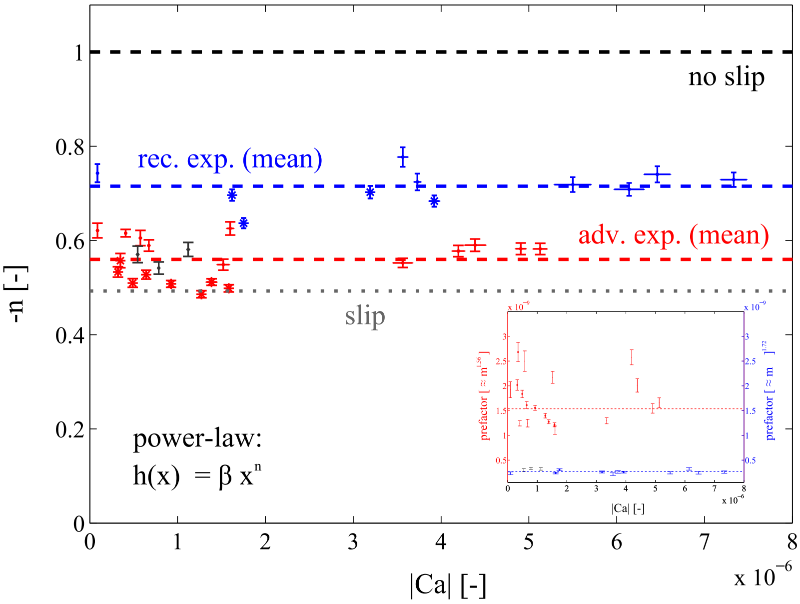

Figure 5.6: Fitted exponent (see Section 2.3) as a function of the magnitude of the capillary number ($|Ca|$) for advancing (red and black) and receding (blue) precursor film profiles for different working liquids (red and blue dots/asterisks are for glycerol, black dots are for 1-octanol). The inset shows the fitted prefactor as a function of capillary number for both the advancing and receding precursor film. The mean value of the prefactor of the advancing film profiles, is approximately 6 times as large as the value for the prefactor of the receding precursor films.

5.4 Results and discussion

Similar to Hoang and Kavehpour (2011), the precursor film was characterized by a nonlinear curve fit. In fact, a power-law fit was used with the prefactor and the exponent as fit parameters. In Figure 5.3, a typical result of a fitted curve to the precursor film of a glycerol droplet is shown. The precursor was obtained for the case of a contact line that moves stationary through the FOV, and thus Figure 5.3 represents a snapshot of this motion. It should be noted that stick-slip effects of the nanoscale contact line were not observed during the experiments.

Furthermore, Figure 5.2 illustrates a clear difference between the advancing and receding precursor film profile, and is the topic of Chapter 6.

The fit parameters provide more insight in the behavior of the moving precursor film, moreover the fitted exponent n is shown in Figure 5.6, and illustrates that the behavior is independent of contact line velocity, hence capillary number. These different capillary numbers were obtained by operating the syringe pump at different flow rates.

The mean value for the fitted exponent n of the advancing interface is -0.56 ± 0.04, and differs from the mean value of the receding interface, which is -0.72 ± 0.03. Furthermore, two different liquids (glycerol and 1-octanol dyed with Rhodamine B) were used to see whether the working fluid had an effect on the results, and verify that the fitted exponent n is independent of material properties, as shown in Figure 5.6.

As noted in Section 5.1, a scaling of $1/x$ or $1/\sqrt{x}$ of the interface $h(x)$ is predicted based on a no slip or slip boundary condition at the solid surface respectively. The experimentally obtained exponent $n = -0.56 \pm 0.04$ agrees very well with the theory based on a slip velocity, meaning that it is plausible to assume that (molecular) slip is present at the solid surface.

For the fitted value of $L_{slip} = 12.0 \times 10^{-9}\, m$ the agreement between model prediction and experimental data for the precursor film moving with a contact line velocity of $U_{CL} = 5.13 \times 10^{-6}\, m/s$ is shown in Figure 5.7.
If the value of U_{CL} (see above) is changed and the value of L_{slip} is kept the same, the model prediction and experimental data disagree. The model prediction changes significantly with a changing value of U_{CL}, whereas the experimental precursor film thickness is nearly independent of the velocity (as shown in Figure 5.6). However, there are indications given in the literature that L_{slip} is proportional to U_{slip} (see Li and Yoda, 2010; Brochard-Wyart et al., 1994). So in our calculations, L_{slip} with respect to U_{CL} is changed in such a way, that the ratio L_{slip}/U_{CL} remains constant. It is then found, that indeed the predicted precursor film thickness is nearly independent of velocity (in accordance with the experiments). This can be understood by studying Equation 5.11 for the middle part in more detail. In a dimensional form it is written as

$$h = \frac{1 + (1 + 6\, L_{slip}\, Ca\, x/a^2)^{1/2}}{2\, Ca\, x/a^2}\,. \tag{5.14}$$

For the largest part of the precursor film $6\, L_{slip}\, Ca\, x/a^2 >> 1$ holds, and h can then be approximated by

$$h = \frac{6^{1/2}}{2}\, a \left[-\frac{L_{slip}\, \gamma}{\mu\, U_{CL}\, x} \right]^{1/2}\,. \tag{5.15}$$

Indeed, when L_{slip} is proportional to U_{CL}, the scaling of h is independent of U_{CL}, as also illustrated by the fitted exponent n in Figure 5.6. Furthermore, the experimental data

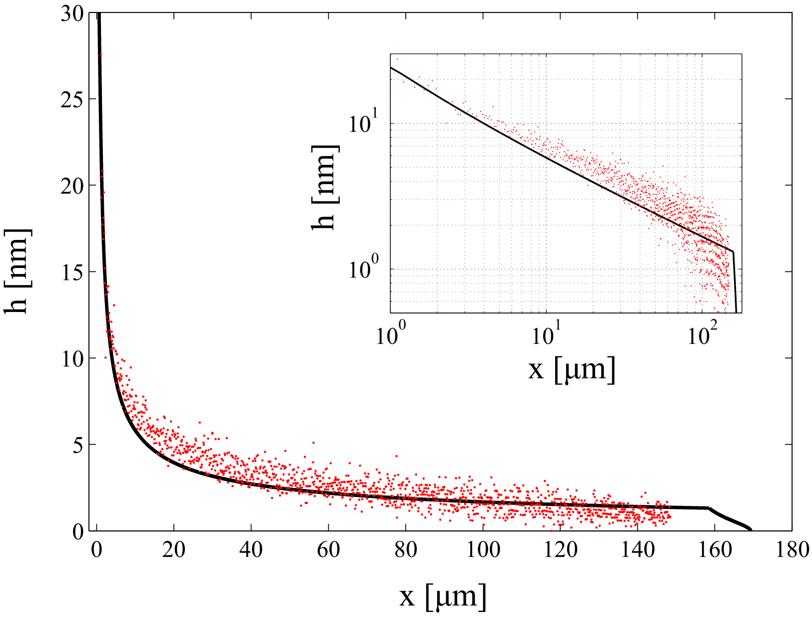

Figure 5.7: Precursor film thickness h as a function of the distance to the droplet x for an advancing contact line with velocity $U_{CL} = 5.13 \pm 0.04$ $\mu m/s$. Both theoretical results (solid black line) and experimental results (red dots) are plotted.

matches the theoretical prediction of a scaling of the film height h proportional to $1/\sqrt{x}$, as shown in Figure 5.8.
Figure 5.9 shows the values of the slip length L_{slip} to obtain the best fit between predicted and measured profiles for the precursor film for different contact line velocities. Although the last decade remarkable attention has been given to fluid slip at surfaces, it remains a highly debated topic. For example, the most recent measurements addressing the boundary condition and its different wetting properties, are performed by Li and Yoda (2010). They used a method, in which the displacements of submicron-sized fluorescent tracer particles were determined in a near-wall region in order to estimate the velocity field $\bar{u}$. The difficulty with these evanescent wave based methods is to determine the distance z from the wall where each velocity measurement should be appointed to. The registration uncertainty in z directly affects the estimation accuracy of the slip length.

Li and Yoda (2010) reported slip lengths close to 0 nm, however a significant uncertainty (± 40 nm) in slip length remains for both the hydrophilic and the hydrophobic surfaces. Furthermore, the slip lengths for the hydrophilic surface (0 to 8 nm) are slightly smaller compared with slip lengths for the hydrophobic surface (0 to 23 nm), and appear to increase slightly as shear rate increases.

The value for the slip length reported by Li and Yoda (2010) is somewhat smaller than the ones reported in previous research with a similar technique (Huang et al., 2006; Huang and Breuer, 2007; Lasne et al., 2008), which range from 0 to 100 nm.

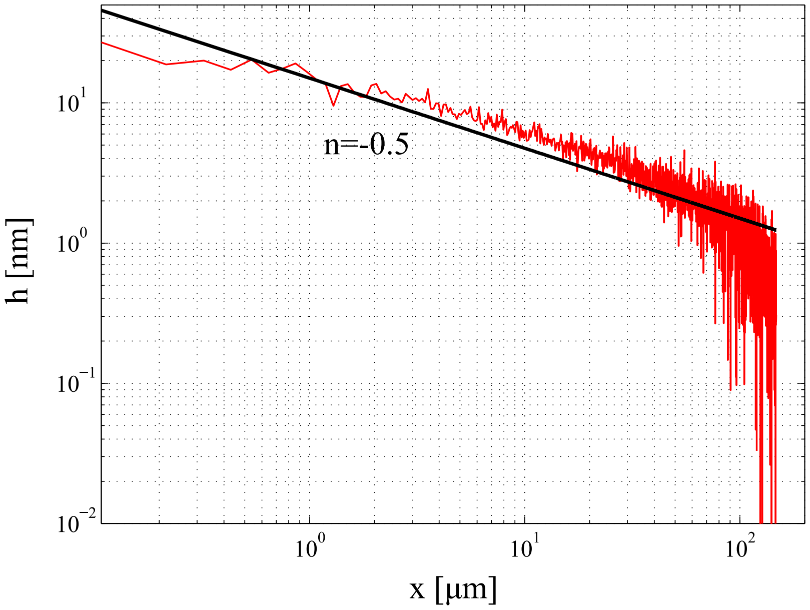

Figure 5.8: Precursor film thickness h as a function of the distance to the droplet x for an advancing contact line with velocity $U_{CL} = 5.13 \pm 0.04\ \mu m/s$ on a logarithmic scale.

In addition, MD simulations have been utilized as well to investigate the continuum boundary condition at a solid surface. The cases studied range from complete wetting to non-wetting, and the numerically obtained slip lengths range from 0 to 100 nm (Jabbarzadeh et al., 2000; Sokhan et al., 2002; Nagayama and Cheng, 2004; Cottin-Bizonne et al., 2004; Voronov et al., 2007).

5.5 Conclusion

Although Hardy provided the first evidence of the existence of the precursor film in 1919, the shape of a moving precursor film is now measured for the very first time in the adiabatic regime in the case of a partially wetting droplet, which provides valuable information for numerical simulations.

Furthermore, the results for the precursor film profile of both advancing and receding precursor films were characterized by a power-law fit, where the fitted exponent was used to characterize the precursor film. The fitted exponent (representing the shape of the precursor film) for the advancing as well as the receding situation is independent of contact line velocity.

Moreover, the mesoscopic film profile h scales approximately with $1/\sqrt{x}$. This result is in agreement with theory based on slip at the solid surface, as suggested by Bruinsma (1990) and Brochard-Wyart et al. (1994). Moreover, based on the lubrication approximation, the slip length is found to be proportional with the contact line velocity. Our findings

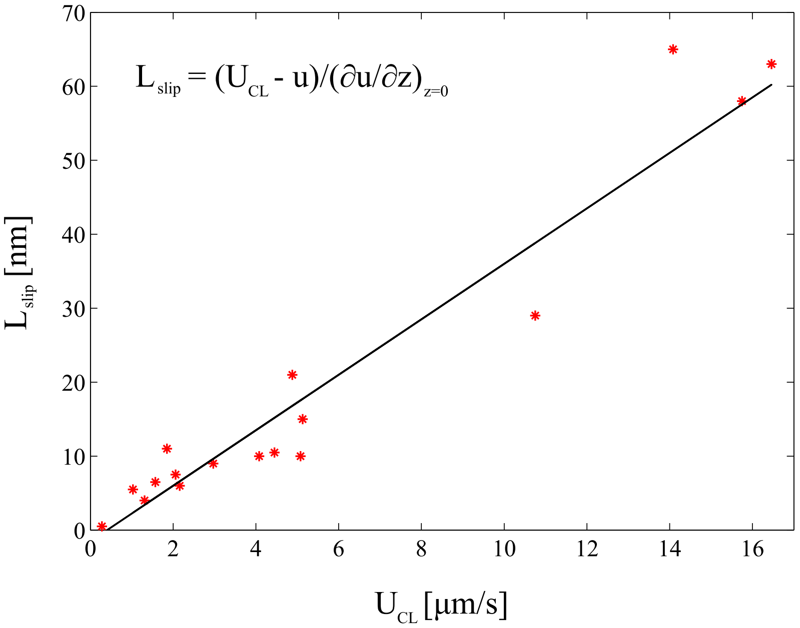

Figure 5.9: Slip length L_{slip} as a function of contact line velocity U_{CL} for an effective Hamaker constant $A = 2.8 \times 10^{-20} J$. The experimental data (red asterisks) is fitted with a linear fit (solid black line).

indicate that slip exists, and is consistent with both experimental as numerical work for the advancing contact line.

Although contact line hysteresis has been studied extensively at larger length scales, it has now for the first time been observed at a mesoscopic scale. The experimental results for the precursor film profile showed that a clear difference between advancing and receding contact lines is present at a mesoscopic scale. A possible explanation for the difference in precursor film profile of an advancing and a receding contact line is described in detail in Chapter 6.

Chapter 6

Contact Line Hysteresis from a Microscopic Point of View*

The difference in shape and behavior between an advancing and a receding contact line is commonly referred to as contact line hysteresis. In the previous chapter, it is experimentally shown for the first time that contact line hysteresis is present at a mesoscopic scale as well. In this chapter, contact line hysteresis is explained by a change in the disjoining pressure. This is shown by comparing the experimental results for the receding precursor film with theoretical results from a model that includes a correction term for the disjoining pressure.

6.1 Components of the disjoining pressure

Additional intermolecular forces noticeably affect the interface of a droplet when its thickness is less than 100 *nm*, as shown in Chapter 4 and 5. As explained by de Gennes (1985), the effect of several intermolecular forces on the contact line is lumped into the disjoining pressure Π, since the total value of the disjoining pressure consists of a structural, an electrostatic and a molecular component (Derjaguin and Churaev, 1974; Teletzke et al., 1988). In particular, the effect of electrostatic forces is likely to become important when the fluid film thickness becomes less than 100 *nm*. Furthermore, since thin films are generally flat, the disjoining pressure can be taken as a function of film thickness only, thus $\Pi = \Pi(h)$ (de Gennes, 1985). Moreover, a model for the disjoining pressure that is inversely proportional to the cube of the film thickness h is proposed for precursor films. Starov et al. (2007) concluded that the mechanism of contact angle hysteresis on smooth homogeneous surfaces as well as heterogeneous surfaces is related to the disjoining pressure.

In the previous chapter a theoretical description of the film thickness for an advancing

---

*To be submitted in modified form as: M.J.Z. Franken, G. Ooms, C. Poelma, and J. Westerweel, *Contact Line Hysteresis from a Microscopic Point of View.*

contact line was described and validated against experimental results. The theory adequately described the experimental data for an advancing contact line by including a finite slip length for the flow in the advancing precursor film. The experimental data also showed a different shape for the receding contact line. The theory did not explain this shape. In this chapter a numerical model is developed that describes receding precursor films, and is compared with experimental results. In this model the disjoining pressure term is modified to predict the precursor film thickness of a receding contact line.

In a frame of reference in which the droplet and precursor film are at rest, the solid wall is moving with velocity U_{CL} in the right-hand side direction for the case of a receding contact line (see inset of Figure 6.1). Moreover, the contact line exerts a viscous force on the precursor film in that direction. When the derivation given in the previous chapter is repeated, a negative sign appears for the viscous friction term in Equation 5.9

$$\frac{d^3\tilde{h}}{d\tilde{x}^3} = -\frac{1}{\tilde{h}^2 + \alpha\, L_{slip}\, \tilde{h}} + \frac{1}{\tilde{h}^4}\frac{d\tilde{h}}{d\tilde{x}} - K_1\, e^{-\tilde{h}/K_2}\frac{d\tilde{h}}{d\tilde{x}}\,. \tag{6.1}$$

Again, the precursor film is divided into three parts: the tip part, the middle part, and the steep rising part. The right-hand side of the middle part is the starting point for our numerical solution. Furthermore, as the viscous force is acting in the positive x-direction, the van der Waals force in the middle part must act in the negative x-direction, and so the film thickness decreases with decreasing x. However, with decreasing film thickness the short-range force starts to become important and acts in the opposite direction, leading to a nearly constant film thickness. So for the middle part the following equation can be solved numerically

$$0 = -\frac{1}{\tilde{h}^2 + \alpha\, L_{slip}\, \tilde{h}} + \frac{1}{\tilde{h}^4}\frac{d\tilde{h}}{d\tilde{x}} - K_1\, e^{-\tilde{h}/K_2}\frac{d\tilde{h}}{d\tilde{x}}\,. \tag{6.2}$$

The following equation is solved for the tip part

$$0 = -\frac{1}{\tilde{h}^2 + \alpha\, L_{slip}\, \tilde{h}} - K_1\, e^{-\tilde{h}/K_2}\frac{d\tilde{h}}{d\tilde{x}}\,, \tag{6.3}$$

and in the end part

$$\frac{d^3\tilde{h}}{d\tilde{x}^3} = -\frac{1}{\tilde{h}^2 + \alpha\, L_{slip}\, \tilde{h}} + \frac{1}{\tilde{h}^4}\frac{d\tilde{h}}{d\tilde{x}}\,. \tag{6.4}$$

The last two equations are the same as for the previous case of an advancing contact line. Only the viscous force has obtained an opposite sign. The result is shown in Figure 6.1. As explained, the film thickness h in the middle part is now practically constant. This

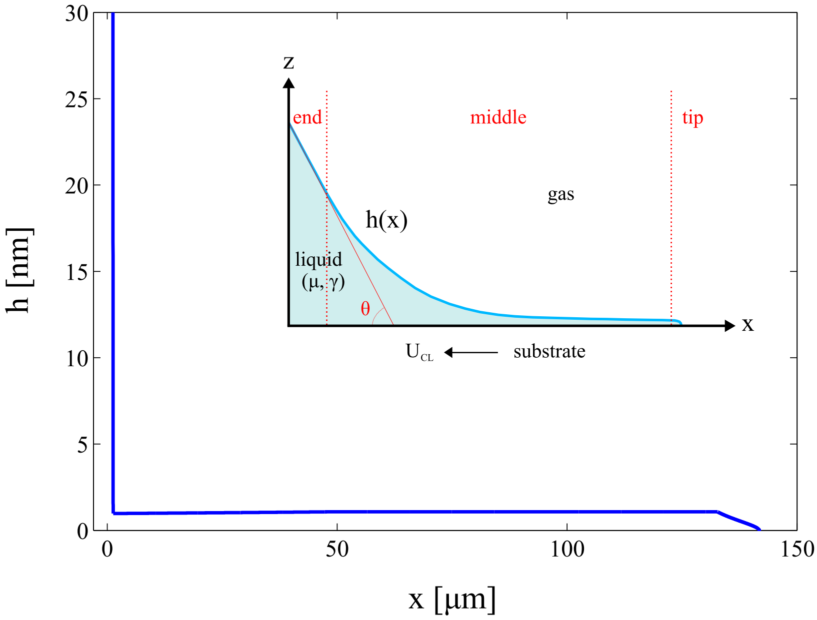

Figure 6.1: Precursor film thickness h as a function of the distance to the droplet x for a receding contact line with velocity $U_{CL} = -5.20\ \mu m/s$.

leads to an unphysical sharp transition from the middle part to the end part of the film thickness close to the droplet, whereas the experimental data show a gradual transition from the middle part to the steep rising part.

To understand the theoretical sharp transition, the force balance in the middle part is changed, and a procedure proposed by Teletzke et al. (1988) is applied. It is assumed that in this region the influence of capillary forces is already present and has to be taken into account. First, Equation 6.1 is rewritten by using the fact that the flux through the film at an arbitrary cross-section of the film (where $h = h(x)$) is the same as at the entrance of the region (where $\tilde{h} = \tilde{h}_\infty$ at $\tilde{x} = 20$)

$$\int_0^{h(x)} u\, dz = \int_0^{h_\infty} u\, dz\,, \tag{6.5}$$

such that Equation 6.1 can be written as

$$\frac{d^3\tilde{h}}{d\tilde{x}^3} = -\frac{\tilde{h}-\tilde{h}_\infty}{\tilde{h}^3 + \alpha\, L_{slip}\, \tilde{h}^2} + \frac{1}{\tilde{h}^4}\frac{d\tilde{h}}{d\tilde{x}} - K_1\, e^{-\tilde{h}/K_2}\frac{d\tilde{h}}{d\tilde{x}}\,. \tag{6.6}$$

To take into account effects by surface tension γ for small deviations, the dimensionless film thickness $\tilde{h}$ is written in the following form

$$\tilde{h} = \tilde{h}_\infty + \beta\, \tilde{h}_1(x) + O(\beta^2)\,, \tag{6.7}$$

where β is the perturbation paramater, which is much smaller than 1 (i.e. $\beta \ll 1$).

By inserting Equation 6.7 into the thin film profile equation (Equation 6.6), and equating the terms with the coefficient β to zero, a linear third-order differential equation with constant coefficients for $\tilde{h}_1$ is obtained

$$\frac{d^3\tilde{h}_1}{d\tilde{x}^3} + p\,\frac{d\tilde{h}_1}{d\tilde{x}} + q\,\tilde{h}_1 = 0\,, \tag{6.8}$$

where $p = -1/\tilde{h}_\infty^4 + K_1\, e^{-\tilde{h}_\infty/K_2}$ and $q = 1/(\tilde{h}_\infty^3 + \alpha\, L_{slip}\, \tilde{h}_\infty^2)$. The solution is

$$\tilde{h}_1(x) = L\, e^{\zeta_1 \tilde{x}} + M\, e^{\zeta_2 \tilde{x}} + N\, e^{\zeta_3 \tilde{x}}\,, \tag{6.9}$$

where L, M and N are constants and the ζ_k are the roots of the characteristic equation

$$\zeta_k^3 + p\,\zeta_k + q = 0\,. \tag{6.10}$$

As $\tilde{h}_\infty << 1$, the discriminant $R = (p/3)^3 + (q/2)^2 < 0$ and there are three real roots of the characteristic equation given by

$$\gamma_k = 2\left(\frac{-p}{3}\right)^{1/2} \cos\left[\frac{1}{3}\cos^{-1}\left(\frac{3\,q}{2\,p}\left(\frac{-3}{p}\right)^{1/2}\right) - k\,\frac{2\pi}{3}\right] \qquad \text{for} \qquad k = 0, 1, 2\,. \tag{6.11}$$

From Equation 6.11 it is directly clear that the roots are of the following order of magnitude $\zeta_k = O(-p)^{1/2} = O(\tilde{h}_\infty^{-2})$. As $\tilde{h}_\infty << 1$ the roots $\zeta_k >> 1$. As $\zeta_k >> 1$, this explains the sharp transition from the middle part to the end part of the precursor film, as illustrated in Figure 6.1.

However, the experimental results for both advancing and receding precursor film profiles show a gradual transition from the middle part to the steep rising end part, as illustrated in Figure 6.2. Our experiments show that for a receding precursor film this gradual transition occurs for the region $2 < \tilde{x} < 20$. To correct our model for this effect, an additional term for the precursor film equation in the region $2 < \tilde{x} < 20$ is introduced.

$$0 \;=\; -\frac{1}{\tilde{h}^2 + \alpha\, L_{slip}\, \tilde{h}} + \frac{1}{\tilde{h}^4}\frac{d\tilde{h}}{d\tilde{x}} - K_1\, e^{-\tilde{h}/K_2}\frac{d\tilde{h}}{d\tilde{x}} + \tilde{C}\,, \tag{6.12}$$

in which $\tilde{C}$ is the correction term. The result presented in Figure 6.2 does not show the sharp transition anymore for a chosen value of $\tilde{C} = 25.6$. Furthermore, the value of $\tilde{C}$ is almost independent of U_{CL}.

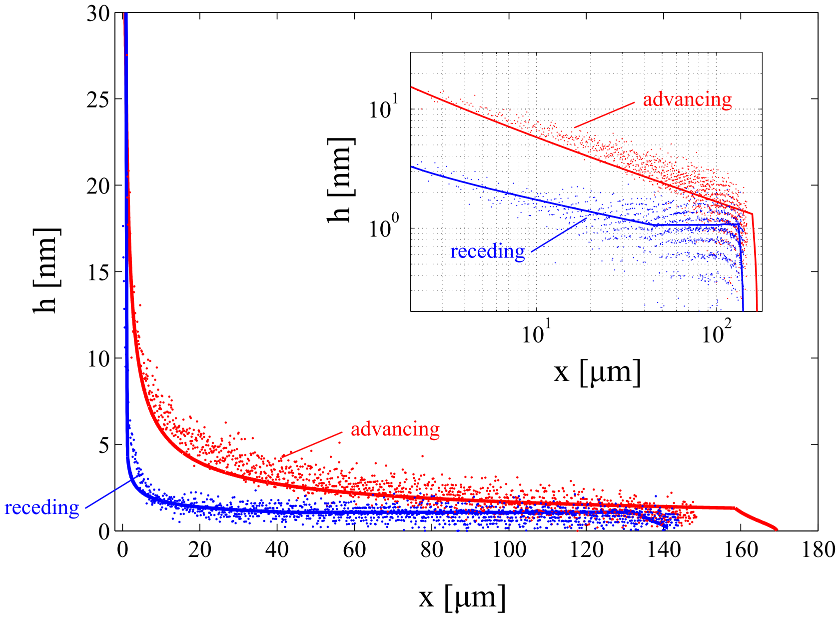

Figure 6.2: Precursor film profiles for advancing (red) and receding (blue) precursor films moving with a contact line velocity of $U_{CL} = 5.13 \pm 0.04\ \mu m/s$ and $U_{CL} = -5.20 \pm 0.02\ \mu m/s$ respectively. The solid lines and dots represent the results from the theoretical model and experiments respectively.

The presence of the correction term $\tilde{C}$ is understood by the following: as the experiments show a decreasing film thickness h with increasing x, both the frictional force on the film (due to wall friction) and the van der Waals force exert a force on the precursor film in the positive x-direction. By assuming a stationary situation, a force in the negative x-direction has to be present in order to compensate for these forces (and will be discussed in the next section). This compensation is represented by the $\tilde{C}$-term in Equation 6.12. The experimentally obtained results for the precursor film profile as well as the results of the theoretical model are shown in Figure 6.2, and show good agreement.

6.2 Discussion

The experimentally obtained results for the precursor film profile as well as the results of the theoretical model are shown in Figure 6.2, and show good agreement. This holds for the shape of the precursor film, since the *length* of the precursor film is difficult to attain quantitatively due to the resolution and sensitivity in combination with the FOV of the measurement.

Furthermore, the agreement for the receding contact line is only obtained when a correction term is introduced into the force balance. Because the contact line velocity U_{CL} for the advancing and receding contact line is almost equal (though opposite in sign), the viscous force is equal as well (but has an opposite sign). As a result, the slip length for the receding precursor film is considered to be equal to the one of the advancing precursor film, hence $L_{slip} = 12.0 \times 10^{-9}\, m$.

Furthermore, as noted by de Gennes (1985), the continuum hypothesis is assumed to be valid up to 3 nm (see also Alder and Wainwright, 1970). Since the deviations in the precursor film profile are approaching this continuum limit, molecular effects are likely to play a role in the hysteresis effect.

For example, Extrand (1998) assumed that wetting could be modeled as an adsorption-desorption process, without specifying the cause of contact angle hysteresis (which could be due to e.g. heterogeneity of the surface (either geometric or chemical) or irreversible interaction of the contact liquid and solid). In the case of an advancing contact line, a bond is created when the contact line advances over the solid. However, it requires additional work or energy to break the bond when the contact line is receding over the solid and causes the contact angle to decrease. Landman et al. (1990) showed by MD simulations and AFM measurements of the adhesion of a nickel wire with a gold substrate, that the attraction force for making contact is less than the external force to separate them.

Furthermore, Yang (1995) treated wetting as an inherently irreversible process, and noted that wetting (or contact line) hysteresis is the result of energy dissipation occurring in advancing and receding contact lines (in the processes of wetting and dewetting respectively). This explains why a correction term is required.

More recent, Tadmor et al. (2009) demonstrated that lateral adhesion forces at the interface between a liquid drop and a substrate are higher for a pendant drop than for a sessile drop. Their results were obtained with a novel instrument that allowed for the first time measurements of the lateral adhesion forces at a solid-liquid interface. They suggested that this difference in adhesion forces at the solid surface molecular reorientation is facilitated both by pushing and pulling body forces (Israelachvili, 1997). Their suggestion is in agreement with the experimental results for the advancing and receding precursor film profiles of a droplet, since an additional force in the theoretical model is required to match the experimentally obtained results for the receding precursor film.

6.3 Conclusion

The experimental and theoretical results are in good agreement when a correction term is introduced into the force balance for the precursor film region of a receding contact line. It is therefore arguable that not all the physics are included in the theoretical model.

It is crucial that an accurate and complete model for contact line motion is developed. For example, MD simulations can perhaps provide valuable information regarding the behavior of advancing and receding precursor film profiles. However, this is beyond the scope of the thesis and is considered as future work.

Chapter 7

Precursor Films in Microfluidic Channels

This chapter describes a study into the precursor film formed ahead of a meniscus of a wetting fluid in a microfluidic channel. Up to now, only precursor films of a droplet are studied experimentally. The precursor film profile is measured for the very first time in a microfluidic channel for varying channel depths, in order to study the effect of channel geometry on the profile of the precursor film. The results demonstrate that local flow hydrodynamics have an effect on the precursor film profile.

7.1 Introduction

Besides being of fundamental interest, wetting plays an important role in microfluidic channels, as present in *Lab-on-a-Chip* applications. These systems make use of the fact that surface effects become dominant due to scaling in these microfluidic systems. Nowadays, technological developments result in even smaller microfluidic channels, hence the research field of nanofluidics. However, a fundamental understanding of the behavior of a fluid in nanofluidic channels is lacking, since the dimensions are approaching the limit of the continuum hypothesis.

In order to gain more insight in wetting in microfluidic channels, the precursor film of an advancing meniscus in a microfluidic channel is studied. By comparing the results for the precursor film profile for varying channel depths with the results for a droplet, we gain more insight in the physics of wetting phenomena.

7.2 Experimental setup

The precursor film profile of a meniscus in a microfluidic channel is studied using the experimental setup as described in detail in Chapter 3. The working fluid (glycerol dyed with

Rhodamine B) is driven by a syringe pump (neMESYS, cetoni GmbH, Korbussen, Germany) in combination with a 1 *ml* glass syringe (Fortuna Optima, Poulten & Graf GmbH, Wertheim, Germany). The meniscus moves in a stationary way through a microchannel (Glycotech, Maryland, USA). This microchannel has an interchangeable gasket, and therefore has flexibility in channel geometry. Two gasket thicknesses D were used, namely 130 μm and 260 μm, whereas the channel width was fixed on 2.5 *mm*. Figure 7.1a shows a schematic of the experimental setup, while Figure 7.1b shows a close-up of the microfluidic channel. The Glycotech microfluidic system has the advantage that standard glass substrates (Menzel-Gläser, Braunschweig, Germany) could be used, making it possible to directly compare the results with the ones of droplet spreading (see Chapter 5). Furthermore, the measurements are conducted near the center of the microchannel in order to ensure that the curvature of the meniscus in the xy-plane does not affect the results.

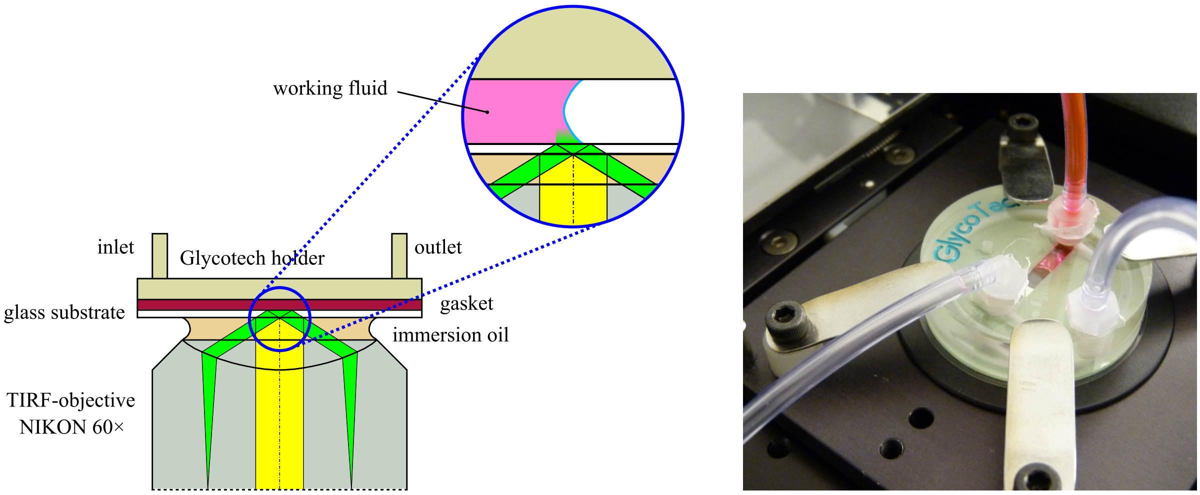

(a)

(b)

Figure 7.1: (a) Schematic of measurement of precursor film of the meniscus in a microfluidic channel, (b) close-up of experimental setup.

The measurements, similar to the ones in Chapter 5, are conducted within a relatively short period. Therefore, we assume that during the motion of the meniscus (hence contact line), only motion due to the applied pressure difference arises.

7.3 Results and discussion

In Figure 7.2, different precursor film profiles are shown for different experiments, and show remarkable reproducibility. The results illustrate that the precursor film profiles are independent of contact line velocity U_{CL}, hence capillary number Ca. This finding for the advancing precursor film profile in a microfluidic channel is in agreement with the results for an advancing precursor film of a partial wetting droplet (see Chapter 5). However, a significant difference is noticeable between the precursor film profile measured in a microchannel of depth $D = 130\ \mu m$ and $D = 260\ \mu m$.

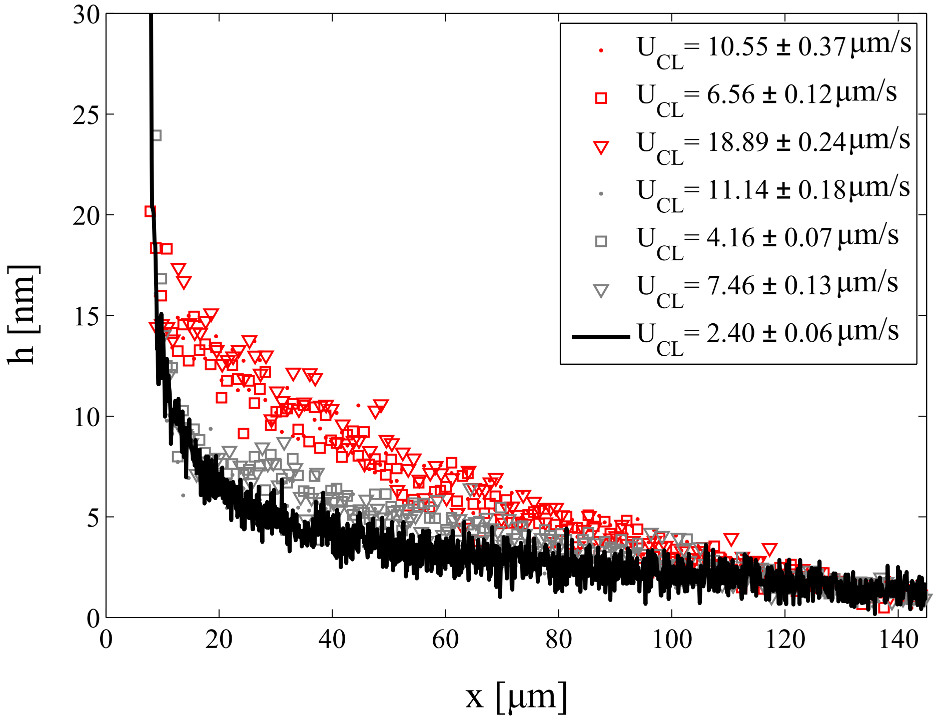

Figure 7.2: Advancing precursor film profile of a stationary moving meniscus of glycerol on glass for different contact line velocities in a microfluidic channel of depth $D = 130\ \mu m$ (red markers) and $D = 260\ \mu m$ (grey markers), compared with a precursor film of a droplet on a dry substrate (solid black line). For clarity, only one ninth of the number of data points of the precursor film profiles in the microfluidic channel (red and grey markers) are plotted.

This difference can be explained by the velocity field in the vicinity of the contact line, which is such that the fluid flows downwards along the contact line, and back into the bulk along the glass substrate (Huh and Scriven, 1971; Kim et al., 2006). Therefore, the flow profile in the vicinity of the contact line is far from being a Poiseuille flow profile. By decreasing the thickness of the microchannel, the point of maximum velocity is shifted towards the substrate, which apparently causes the precursor film to be thicker due to a different boundary condition for the lubrication flow equations. Geometric considerations (the symmetry of the problem) forces a curvature, which leads to a large contribution due to $\gamma\, \partial^3 h/\partial x^3$.

7.4 Conclusion

From the experimental data it is clear that the depth of a microfluidic channel has an effect on the precursor film profile. Namely, the precursor film profile of the meniscus is not fully decoupled from the macroscopic wetting properties. An explanation for the difference in precursor film profile, is that the flow field in the vicinity of the contact line is different for varying microchannel depths. Therefore, wettability in microfluidic systems is not so obvious.

Unfortunately, experimental data regarding detailed measurements of the flow field in the vicinity of the contact line is lacking in the mesoscopic region of the contact line, meaning that no other data exists that supports our findings. In order to understand the flow in the vicinity of the meniscus in a microfluidic channel, Kim et al. (2006) used a micro-PIV system with a high-speed camera to measure the flow field near the advancing meniscus in a microchannel. The meniscus moving through a hydrophilic and hydrophobic rectangular microchannel was studied in a moving reference frame. A clear difference in velocity field in the vicinity of the contact line was found. However, due to limitations in (out-of-plane as well as in-plane) resolution of their technique, the mesoscopic region of a contact line could not be attained. Furthermore, the effect of microchannel geometry on the velocity filed was not studied, and this would be interesting to clarify the results for the presented experimental results in this chapter.

Appendix B and C give a detailed description of the required measurement technique Total Internal Reflection Velocimetry (TIRV) to extract the velocity field from particle displacements, and (a modification of) the experimental setup to perform these measurements of the velocity field close (within the wavelength of the light) to the contact line, respectively.

However, probing the velocity field in the vicinity of the contact line is beyond the scope of the thesis, and therefore considered as future work.

Chapter 8

Conclusion and Future Work

The aim of this work was the precise characterization of the precursor film of dynamic contact lines. The results are concluded in this chapter and several recommendations for future work are given.

8.1 Conclusion

The main research objectives, as stated in Section 1.3, were twofold. Firstly, a measurement technique was developed that allowed the study of dynamic precursor films. In order to precisely characterize the precursor film profile one needs to deal with the great disparity of time and length scales. Hence, the spatial and temporal resolution were pushed to the limit of what is currently possible in order to study the dynamics of precursor films. Secondly, the dynamics of precursor films of advancing and receding contact lines were studied with the developed technique. A theoretical model for both the advancing and receding contact lines was developed in order to predict the behavior and explain contact line hysteresis.

Measurement technique

Special considerations were required to employ total internal reflection fluorescence microscopy in order to quantitatively measure the precursor film of a droplet. Total internal reflection fluorescence microscopy is not limited to a scale larger than the wavelength of the light and therefore has the required sub-wavelength resolution perpendicular to the substrate. This property is essential to precisely characterize the thickness of the precursor film.

The thickness of the precursor film was determined using the intensity distribution at the edge of the droplet. This was possible due to the unique property of the evanescent excitation field (resulting from total internal reflection of incident light), namely an exponentially decaying intensity from the substrate. However, the evanescent field required characterization of its penetration depth, which was done by combined TIRFM-AFM. By simultaneously moving a sub-micron sized particle through the evanescent field and measuring its fluorescence intensity, an intensity versus distance curve was obtained. The penetration depth of the evanescent field was eventually determined from this curve, and showed very good agreement with a theoretical prediction of the penetration depth based on the maximum incident angle.

Furthermore, non-disturbing AFM-imaging was used to validate the nanoscale interface obtained with TIRFM. The results for the nanoscale interface were in very good agreement for a droplet in equilibrium. Based on these results, it is conluded that the measurement technique is capable of precisely detecting and characterizing a precursor film.

Dynamics of precursor films

A precursor film is thought to be one of the mechanisms that relieves the shear stress singularity at the macroscopic contact line, and arises due to van der Waals interaction. This study gave more insight in how the precursor film (of a partially wetting droplet) behaves when the macroscopic contact line is moving. Firstly, the existence of a precursor film for a partial wetting droplet was shown by utilizing the developed technique. Secondly, by precisely measuring the profile of an adiabatic precursor film, the boundary condition at the solid surface was investigated. A scaling of $h(x) \sim 1/\sqrt{x}$ was found for an advancing precursor film by a power-law fit. Furthermore, the profile was found to be independent of contact line velocity. Both findings are in agreement with theory where slip at the solid surface is assumed. Because the profile of the precursor film was found to be independent of the contact line velocity, it was concluded that the slip length is proportional with the contact line velocity.

Contact line hysteresis

Although contact line hysteresis has been studied extensively at larger length scales, it has now for the first time been observed at a mesoscopic scale. The experimental results for the precursor film profile showed that a clear difference between advancing and receding contact lines is present at a mesoscopic scale. A theoretical model for the advancing and receding contact line is developed in order to explain this difference. When a correction term is introduced into the force balance for the precursor film region of a receding contact line, a good agreement with the experimental results appears. The correction term was interpreted as the result of molecular effects that cause wetting and dewetting to be an inherent irreversible process. Hence, it is argued that not all the physics are included in the theoretical model, such as molecular effects, since the model used for the disjoining pressure is a relatively simple model. This is based on literature findings where contact line hysteresis is the result of energy dissipation occuring in advancing and receding contact lines. It is therefore concluded that an accurate and complete model for contact line motion needs to be developed.

8.2 Future work

This section provides a number of ideas that should lead to a better understanding of the behavior of contact line dynamics in general and the dynamics of precursor films in particular.

Correction term in force balance of receding precursor film

In Chapter 6 it was shown that contact angle hysteresis is not in contradiction with the irreversibility of contact line dynamics. This was illustrated by introducing an additional force into the force balance via a correction term. Because the disjoining pressure is dependent on the properties of the media under consideration (which are taken into account by the effective Hamaker constant), it is expected that the correction term $\tilde{C}$ is different for various combinations of media. This can be validated by repeating the measurements of the precursor film profile of a receding contact line for a number of working liquids.

Effect of coatings on precursor film

Most studies regarding wetting and spreading include the effects of wettability (e.g. hydrophilic or hydrophobic surface properties). Although the effect of surface tension between liquid and solid is not directly included in the force balance for the precursor film, it is conjectured that this results in a change in the effective Hamaker constant. How this affects the behavior of the precursor film is unclear. However, special considerations need to be taken with respect to the evanescent field, since multiple layers can result in a change of refractive index, and thus a precise characterization is required for each coating.

Velocity field in the vicinity of the contact line

In previous chapters it is explained that a mathematical singularity arises due to a diverging velocity field towards the edge of the droplet, as noted by Huh and Scriven (1971). In Chapter 5 it was shown by precisely measuring the profile of dynamic precursor films, a scaling related to fluid slippage was found. So far, there is no quantitative information of the velocity field in the vicinity of the contact line. Although Kim et al. (2006) did do measurements of the velocity field in the vicinity of a moving meniscus through a microchannel, their technique did not have sufficient resolution to attain the precursor film region. Therefore, a method is proposed (including a modification of the existing experimental setup) to probe the near-wall velocities in the vicinity of the contact line, which is described in Appendix B and C.

Coalescence of liquid droplets

When two droplets touch, surface tension drives an initially singular motion which drives them into a bigger droplet (Eggers et al., 1999). This motion is always dominated by viscous effects at early times. However, it remains unclear when the droplets exactly "touch" each other. For example, how van der Waals interactions will cause the interfaces to connect and form a neck.

Up to now, it was not possible to measure the precursor film while it is moving or in the process of droplet merging. This is because the precursor film is very difficult to attain experimentally due to the presence of several different length and time scales involved in this microscopic droplet feature. Nevertheless, the developed measurement technique (as described in Chapter 4) is a promising one to use for the study of the precursor film in the process of coalescence. However, the measurements described in the previous chapters were done with a very sensitive high-resolution CCD only suitable for recording at relatively low frame rates (maximum approximately 20 *Hz*). Since this neck formation occurs on a very small timescale, high-speed imaging is required. For this purpose, a high-speed camera was connected to the Nikon microscope to see whether sufficient signal remains at high recording rates. The measurements were conducted in a similar way as described in Chapter 5, but now a second (non-moving) droplet was placed on the substrate. An advancing contact line was obtained by delivering fluid via a small needle (as described in Section 5.2) in one droplet, such that it coalesced with the second droplet.

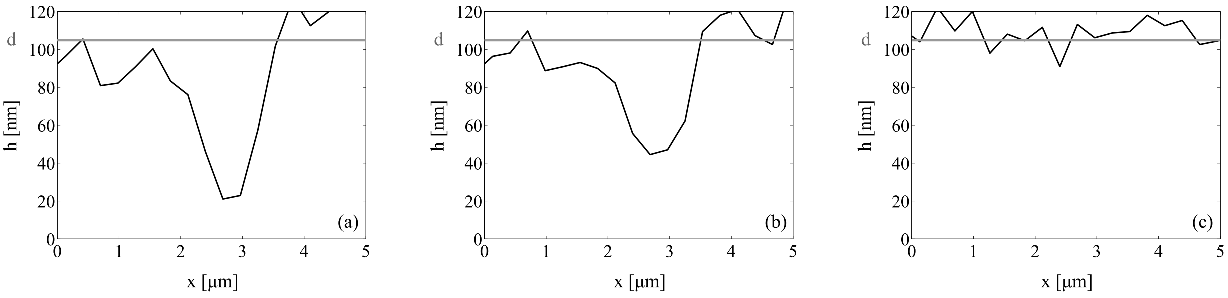

Figure 8.1: Merging of two interfaces of glycerol droplets recorded with a framerate of 500 *Hz* at (a) 0 *ms*, (b) 2 *ms*, and (c) 4 *ms* recorded with a Photron high-speed camera.

In Figure 8.1, the merging of two droplet interfaces at nanoscale level is illustrated. The process of coalescence was recorded with a standard high-speed camera (Fastcam RS, Photron, San Diego, CA, USA), and demonstrates that the developed measurement technique is able to reconstruct a moving droplet interface at nanoscale level. However, a short shutter time resulted in a low signal-to-noise ratio. In combination with a relatively high background noise of the CMOS sensor and low signal strength, information of the precursor film is lost (see also Section 4.4).

One way to increase the signal-to-noise ratio, is to use an image intensifier. In such a device the fluorescence signal is intensified to enhance the low light-level images. For this purpose, an intensified high-speed camera (HiCAM 5000, Lambert Instruments, Roden, the Netherlands) was used to enhance the signal. The CMOS sensor of this camera has an 8-bit dynamic range, and thus provided a limitation to the dynamic measurements.

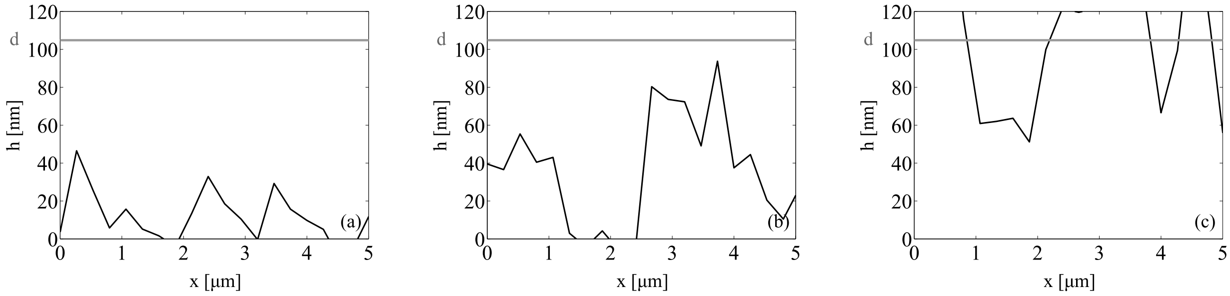

Figure 8.2: Merging of two interfaces of glycerol droplets at (a) 0 *ms*, (b) 4 *ms*, and (c) 8 *ms* recorded with a Lambert Instruments intensified high-speed camera at 5 *kHz*.

The results shown in Figure 8.1 and 8.2 illustrate that TIRFM is capable of capturing droplet-droplet coalescence at nanoscale level. However, the signal-to-noise ratio is not sufficient to completely capture the dynamics of the precursor film profile, and therefore the results remain illustrative only.

One possible way to improve this, is to increase the laser intensity (while taking into account photobleaching) by using a high-speed pulsed laser source. A drawback of using a pulsed laser source is that the energy per pulse can vary, which needs to be taken into account in order to quantitatively measure the nanoscale interface. Furthermore, the optics in the Nikon microscope are normally not used for high power lasers in combination with TIRF. Discussions with the manufacturer (Nikon Europe) have not been conclusive with respect to the question if it was safe to direct high intensity laser light through these optics. Although some difficulties exist, the technique is very promising (and so far the only technique that can be used) for the study of coalescence at nanoscale level.

Appendix A

Lubrication Theory for Thin Film Flows

Lubrication theory is commonly applied to describe fluid flow in bearings, and applies to very low Reynolds number flows. In a bearing, a thin fluid film exists between two rigid surfaces. In this case, the geometry allows the simplification of the Navier-Stokes equations to the so-called lubrication approximation. Furthermore, lubrication theory can be applied for the flow of a thin film with a free surface, such as a spreading droplet or the preparation of a coating. Although, the classical lubrication theory was described long time ago by Osborne Reynolds (Reynolds, 1886), the application where van der Waals forces come into play is not so straightforward. Therefore, the lubrication approximation is derived by starting with the classical lubrication theory, and the van der Waals interaction is included later on.

Governing equations

The lubrication approximation for thin film flows is derived from the two-dimensional Navier-Stokes equations for an incompressible fluid. The conservation of mass and momentum are written as

$$\frac{\partial \rho}{\partial t} + \nabla \cdot (\rho \bar{u}) = 0\,, \tag{A.1}$$

and

$$\rho \, \frac{D\bar{u}}{Dt} = -\nabla p + \nabla \cdot \bar{\tau} + \rho \, \bar{g}\,, \tag{A.2}$$

where $D/Dt = \partial/\partial t + \bar{u} \cdot \nabla$ is the material derivative. In case of a Newtonian fluid, the shear stress $\bar{\tau}$ is directly proportional to the strain rate, meaning that $\bar{\tau} = \mu \, \nabla \bar{u}$. Hence, the conservation of momentum is written as

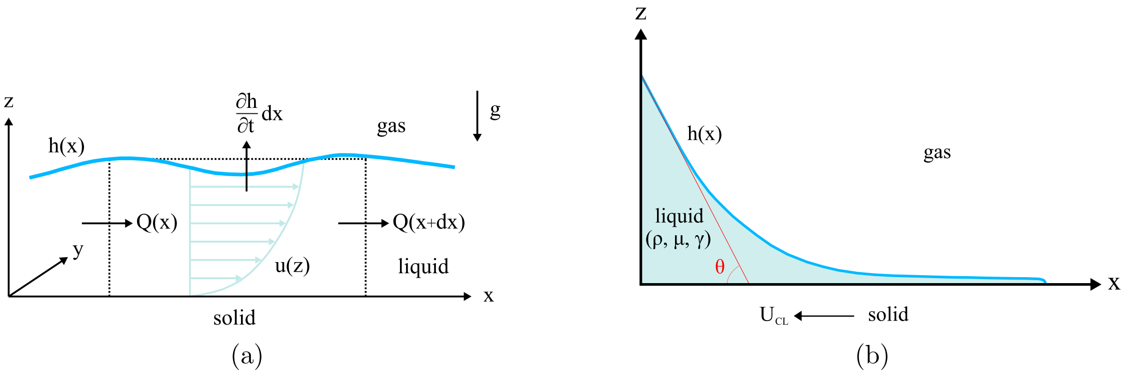

Figure A.1: (a) Schematic of thin film flow illustrating the scales involved and coordinate system used, (b) schematic of a stationary moving precursor film with contact line velocity U_{CL}, where ρ is the density of the liquid, μ is the dynamic viscosity of the liquid, and γ is the surface tension between liquid and gas.

$$\rho\left(\frac{\partial u}{\partial t}+u\,\frac{\partial u}{\partial x}+w\,\frac{\partial u}{\partial z}\right)=-\frac{\partial p}{\partial x}+\mu\left(\frac{\partial^2 u}{\partial x^2}+\frac{\partial^2 u}{\partial z^2}\right)\,, \tag{A.3}$$

$$\rho\left(\frac{\partial w}{\partial t}+u\,\frac{\partial w}{\partial x}+w\,\frac{\partial w}{\partial z}\right)=-\frac{\partial p}{\partial z}+\mu\left(\frac{\partial^2 w}{\partial x^2}+\frac{\partial^2 w}{\partial z^2}\right)+\rho\,g\,. \tag{A.4}$$

Stokes (or creeping) flow is applicable when the Reynolds number is very small ($Re \ll 1$), the acceleration (e.g. a change in inertia) of the fluid can then be neglected, meaning that $\partial\bar{u}/\partial t \approx 0$ (unsteady acceleration) and $\bar{u}\,\nabla\bar{u} \approx 0$ (convective acceleration). The Navier-Stokes equations then reduce to

$$\frac{\partial u}{\partial x}+\frac{\partial w}{\partial z}=0\,, \tag{A.5}$$

and

$$0=-\frac{\partial p}{\partial x}+\mu\left(\frac{\partial^2 u}{\partial x^2}+\frac{\partial^2 u}{\partial z^2}\right)\,, \tag{A.6}$$

$$0=-\frac{\partial p}{\partial z}+\mu\left(\frac{\partial^2 w}{\partial x^2}+\frac{\partial^2 w}{\partial z^2}\right)+\rho\,g\,. \tag{A.7}$$

The dominant terms in Equations A.6 and A.7 are derived by an order-of-magnitude estimation in terms of scales, by using the following scaling parameters for the coordinates and velocities:

$$\tilde{x}=\frac{x}{L},\;\;\tilde{z}=\frac{z}{H},\;\;\tilde{u}=\frac{u}{U},\;\;\tilde{w}=\frac{w}{W}\,. \tag{A.8}$$

Typically, in lubrication theory two length scales are involved: H for the film thickness, and L as a characteristic lateral length scale. The ratio of these two characteristic length scales is $\epsilon = H/L$. Furthermore, a reduction of film height results in an increase in velocity, meaning that $\frac{U}{L} - \frac{W}{H} = 0$ (conservation of mass, Equation A.5), it follows that $\widetilde{w} = \frac{w}{\epsilon U}$.

From the order-of-magnitude estimation it follows that

$$\frac{\partial p}{\partial x} = \mu \frac{U}{H^2} \left[\epsilon^2 \frac{\partial^2 \tilde{u}}{\partial \tilde{x}^2} + \frac{\partial^2 \tilde{u}}{\partial \tilde{z}^2} \right] , \tag{A.9}$$

$$\frac{\partial p}{\partial z} = \mu \frac{U}{H^2} \left[\epsilon^3 \frac{\partial^2 \tilde{w}}{\partial \tilde{x}^2} + \epsilon \frac{\partial^2 \tilde{w}}{\partial \tilde{z}^2} \right] + \rho \, g \, . \tag{A.10}$$

The key requirement for lubrication theory is that ϵ is small ($\epsilon \ll 1$), which allows the determination of the dominant terms in Equations A.9 and A.10. As a result, Equations A.6 and A.7 reduce to

$$\frac{\partial p}{\partial x} = \mu \frac{\partial^2 u}{\partial z^2} , \tag{A.11}$$

and

$$\frac{\partial p}{\partial z} = \rho \, g \, . \tag{A.12}$$

From Equations A.11 and A.12, the velocity in the fluid film $u(z)$ and the pressure across the fluid film $p(x, z)$ are derived respectively.

Pressure across the fluid film

The expression for the pressure across the fluid film is

$$p(x, z) = \int \frac{\partial p}{\partial z} dz = \int \rho \, g \, dz = \rho \, g \, z + C \, . \tag{A.13}$$

The integration constant in Equation A.13 takes into account surface effects. At the surface or fluid-gas interface ($z = h$, see Figure A.1a), pressure differences due to surface curvature exist. These pressure differences are accounted for by the capillary pressure, thus at the interface $p(z)$ equals $-\gamma \, \nabla^2 h$. Since the lubrication approximation is utilized for a small contact angle (θ, see Figure A.1b), it is valid to assume that the curvature is small ($\frac{\partial h}{\partial x} \ll 1$), hence $\frac{\partial^2 h}{\partial x^2}$ is used as the first order approximation to the curvature of the interface. Furthermore, when the film thickness h becomes very small ($O(\text{nm})$), intermolecular forces start to have an effect on the precursor film profile. This effect (of van der Waals forces) on the precursor film profile of a droplet causes a fluid to be attracted towards the solid surface by an unretarded interaction, and is lumped into a disjoining pressure $\Pi(h)$. In case of a van der Waals fluid, the disjoining pressure is written as

$$\Pi(h) = \frac{A}{6\pi h^3}\,, \tag{A.14}$$

where A is the (effective) Hamaker constant (de Gennes, 1985). As a result, the pressure across the fluid film is written as

$$p(x,z) = \underbrace{\rho\, g\,(h-z)}_{\text{hydrostatic pressure}} - \underbrace{\gamma\,\frac{\partial^2 h}{\partial x^2}}_{\text{capillary pressure}} - \underbrace{\Pi(h)}_{\text{disjoining pressure}}\ . \tag{A.15}$$

Velocity in the fluid film

By integrating Equation A.11 twice with respect to z, and using a no-slip boundary condition at the solid surface, and no shear stress at the interface (by assuming that the viscosity of the surrounding fluid vanishes with respect to the viscosity of the liquid, e.g. air versus liquid):

- $u = 0$ at $z = 0$;
- $\frac{\partial u}{\partial z} = 0$ at $z = h$;

the fluid velocity across the thin film $u(z)$ is written as

$$u(z) = \frac{1}{\mu}\,\frac{\partial p}{\partial x}\left(\frac{z^2}{2} - z\,h\right)\ . \tag{A.16}$$

In the lubrication approximation, the flow profile $u(z)$ of the stationary moving contact line with velocity U_{CL} (as illustrated in Figure A.1b) is the sum of plane Poiseuille and Couette flow.

Flux

The flux Q is obtained by integrating the fluid velocity, hence

$$Q = \int_0^h u(z)\,dz = -\frac{1}{3\mu}\,\frac{\partial p}{\partial x}\,h^3\,. \tag{A.17}$$

In case of a stationary moving contact line in the x-direction with velocity $-U_{CL}$ a reference frame is used, where the surface moves with a velocity U_{CL}. As a result, the flux Q for the uniform motion of this wedge equals $h\,U_{CL}$. From Equation A.17 it follows

$$-\frac{3\mu U_{CL}}{h^2} = \frac{\partial p}{\partial x}\,. \tag{A.18}$$

By substituting the expression for the pressure across the fluid film $p(x,z)$ (Equation A.15) into Equation A.18, and rewriting this, an expression for the film profile is obtained

$$-\frac{3\mu U_{CL}}{h^2} = \rho\, g\,\frac{\partial h}{\partial x} - \gamma\,\frac{\partial^3 h}{\partial x^3} + \frac{A}{2\pi h^4}\,\frac{\partial h}{\partial x}\,. \tag{A.19}$$

Equation A.19 shows that the viscous forces are balanced against hydrostatic forces, capillary forces, and van der Waals forces, and holds for a non-evaporating liquid in the absence of surface tension gradients, such as Marangoni effects.

From mass conservation ($Q(x) - Q(x+dx) - \frac{\partial h}{\partial t}\,dx = 0$), it follows

$$\frac{\partial h}{\partial t} + \frac{\partial Q}{\partial x} = 0\,, \tag{A.20}$$

which results in a partial differential equation for $h(x,t)$

$$\frac{\partial h}{\partial t} + \frac{\partial}{\partial x}\left[\frac{h^3}{3\mu}\left(-\rho\, g\,\frac{\partial h}{\partial x} + \gamma\,\frac{\partial^3 h}{\partial x^3} - \frac{A}{2\pi h^4}\,\frac{\partial h}{\partial x}\right)\right] = 0\,. \tag{A.21}$$

Since the thickness h of the precursor film is $O(nm)$, gravity does not influence the shape of the liquid-gas interface, and thus the effect of the hydrostatic pressure on the precursor film profile is negligible. Furthermore, in case of a stationary moving precursor film ($\frac{\partial h}{\partial t} = 0$), the expression for the precursor film reduces to

$$-\frac{3\mu U_{CL}}{h^2} = -\gamma\,\frac{\partial^3 h}{\partial x^3} + \frac{A}{2\pi h^4}\,\frac{\partial h}{\partial x}\,. \tag{A.22}$$

Equation (A.22) can be solved numerically in order to obtain the precursor film profile h as a function of x, and can be compared with experimental results (see Chapter 5 and 6).

Appendix B

Volumetric Averaging in Total Internal Reflection Velocimetry

Microfluidic devices, such as a Lab-on-a-Chip, take advantage of surface effects. For example, dielectrophoresis can be used for sorting specific particles (Pamme, 2007). These surface effects can be even more pronounced or advantageous in nanofluidic devices. Measurements at these very small scales are difficult and applications using standard micro-PIV are difficult to perform close to the wall due to a limited resolution. One special technique that is currently used to obtain information about near-wall flow velocities, is Total Internal Reflection Velocimetry (TIRV). This technique makes it possible to determine the velocity field $\bar{u}$ averaged over the first few hundred nanometer next to the wall along the optical axis, as illustrated in Figure B.1a.

B.1 Total internal reflection velocimetry

Total Internal Reflection Velocimetry was used by Jin et al. (2004) to measure near-wall flow velocities obtained in the near-wall region of a microfluidic system. The fluorescent tracer particles in water were very locally illuminated with an evanescent excitation field resulting from an incident laser pulse. Moreover, the resulting particle images were analyzed with a Particle Tracking Velocimetry (PTV) method. The near-wall flow velocities were inherently averaged over the first few hundred nanometer from the surface. Although, this approach did not give any information of particle locations along the optical axis, the statistical difference between velocities measured over hydrophilic and hydrophobic surfaces was found to be minimal. However, the uncertainty regarding the exact character of the illumination field prevented a more accurate measurement.

Sadr et al. (2004) used a similar approach to study fully developed and steady electroosmotic flow in a rectangular microchannel. The two components of the velocity field parallel to and within 100 nm of the channel wall were measured by nano-particle image velocimetry.

Huang et al. (2006) extended the technique in order to study the nature of slip velocities experimentally. This was done by using the intensity of the fluorescence emitted by tracer particles in order to also track the particle motion along the optical axis. Hence, three dimensional information was obtained using a PTV algoritm.

Another extension was done by Li et al. (2006) using the exponentially decaying nature of the evanescent wave. This non-uniform illumination caused tracers close to the wall to be brighter in particle images than those farther from the wall. Each particle image was divided into three sub-images based on tracer image intensity, and standard techniques were then used to extract temporally and spatially averaged velocities at three different z-locations. The feasibility of this multilayer nanoPIV was evaluated using artificial images. The results demonstrated that multilayer nanoPIV is feasible if appropriate classification techniques are developed and used to separate tracer images into different layers. The multiplane nanoPIV approach was used by Li and Yoda (2010) to determine slip lengths of steady Poiseuille flow at various Reynolds numbers in hydrophilic and hydrophobically coated microchannels experimentally.

However, current methods use information of the individual particle intensities, which require a very monodisperse seeding of tracer particles. The measurement bias involved with tracer size polydispersity on the fluid velocimetry measurements has been investigated by Wang et al. (2011).

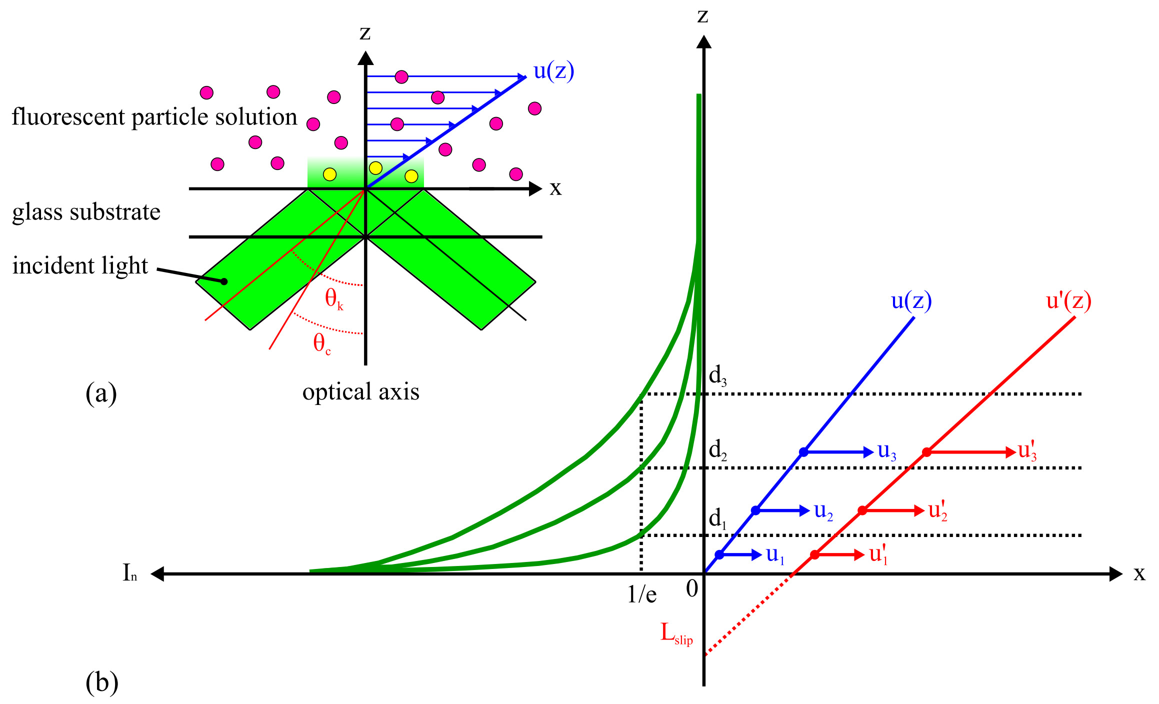

Figure B.1: (a) Schematic of TIRV, (b) concept of volumetric averaging in TIRV. Flow velocities u in case of a no-slip boundary condition, whereas a slip length L_{slip} is associated with a slip velocity u'.

B.2 Volumetric averaging

The novel approach is to obtain several data points along the optical axis (u_k) using several (k) illuminated sections while applying volumetric averaging. The illuminated volumes have an intensity that decays exponentially with distance z and make it possible to perform flow measurements at nanoscale level. By using several illuminated sections, characterized by d_1 to d_3 (for θ_1 to θ_3, Equation 3.3) in Figure B.1b, it should be possible to acquire several data points and recover the velocity profile $u(z)$. Namely, each data point represents a result from averaging over a different (known) depth.

As shown by Li and Yoda (2010) it is important to take into account the near wall concentration of particles via the particle number density $c(z)$. The mean velocity component tangential to the wall for different incident angles is written as

$$u_k = \int_0^{d_k} c(z)\, u(z)\, dz \quad \text{for}\, k = 1, 2, 3, \ldots \tag{B.1}$$

This velocity component represents the near wall velocity tangential to the wall at position $\bar{z}_k$. The particle concentration-weighted average z-position (Li and Yoda, 2010) is calculated with

$$\bar{z}_k = \frac{\int_0^{d_k} c(z)\, z\, dz}{\int_0^{d_k} c(z)\, dz} \quad \text{for}\, k = 1, 2, 3, \ldots \tag{B.2}$$

The characterization of the different illuminated sections for different incident angles (θ_k, see Figure B.1a) can be done by a combined TIRFM-AFM calibration, as described in Chapter 3. Similar to Li et al. (2006), the feasibility of this novel approach can be evaluated first using artificial images or synthetic data.

Appendix C

Combined LIF-TIRV at a Droplet Interface

Flow velocities within a droplet are diverging towards the contact line due to the no-slip boundary condition, which in turn causes a stress singularity at the edge of a droplet as found by Huh and Scriven (1971), and is described in detail in Chapter 2. In theory, this singularity causes infinitely large friction forces, meaning that droplets should not move at all. As illustrated in Figure 2.2, the streamlines indicate a strong recirculation in the wedge, however the flow field has not been attained experimentally very close to the contact line. In order to get insight in the singularity removal and understand its consequences for the flow field on a large scale, flow field measurements in combination with a droplet interface measurement can provide valuable information.

This appendix describes a method and the required modifications to the existing experimental setup (see Chapter 3) in order to perform simultaneous measurements of the droplet interface shape $h(x)$ and the velocity field $\bar{u}$ inside the moving droplet, by combining Laser Induced Fluorescence (LIF) and Total Internal Reflection Velocimetry (TIRV).

C.1 Method

Fluorescence microscopy that uses multiple signals or wavelengths is commonly used in live cell imaging. Furthermore, Kling and Mewes (2004) used two-color Planar Laser Induced Fluorescence (PLIF) to quantify the mixing inside a vessel. Two-color μPIV was used by Wang et al. (2003) in order to determine the fluid velocity field induced by AC electrokinetics. Two different sizes of tracer particles, that contained different fluorescent dyes, allowed them to distinguish the signals using fluorescent filter cubes. Two fluorescent signals are also necessary for a simultaneous measurement of the droplet interface shape $h(x)$ and the near-wall velocity field $\bar{u}$ inside the droplet. A fluorescent dye dissolved in the droplet provides a signal contrast to the outer region at the nanoscale interface, as described in detail in Chapter 4, whereas fluorescent particles can be used as neutrally buoyant fluid tracers for the velocity field determination by e.g. PTV. For the latter, tracer particles of sub-micron diameter have to be used in order to determine the velocity field very close to the droplet edge at nanoscale level. Ideally, the same light source or laser pulse should be used to excite both fluorescent dye and tracer particles. This requires an adequate selection of fluorescent dye and tracer particles as well as the optical filter sets, such that both signals can be adequately separated. It is therefore desired that both the (peak of the) adsorption spectrum of the fluorescent dye and as the tracer particles matches the excitation wavelength (i.e. the laser). This is in contrast to the emission spectra, which should lie as far apart from each other as possible in order to adequately separate these signals.

C.2 Experimental setup

Using only one laser for excitation is desirable for cost and triggering purpopes, but also of practical considerations, in particular for a TIRF-microscope. Therefore, the emitted signals from both fluorescent dye and tracer particles are excited by a 150 mW continuous wave Nd:YAG laser (Coherent, Compass 315M; Santa Clara, CA, USA). The feasibility of quantum dots as flow tracers was demonstrated by Guasto and Breuer (2009).

However, for this study, water soluble Trilite 630 fluorescent nanocrystals with a diameter of about 6 nm (Cytodiagnostics, Ontario, Canada) are carefully selected as tracer particles in combination with a Rhodamine B dye (Sigma-Aldrich, Saint Louis, MO, USA). These quantum dots can be excited by a Nd:YAG laser (532 nm wavelength) and (when excited at this wavelength) emit light at a wavelength of 630 nm (peak). In order to separate the different fluorescent signals, which are necessary to determine $h(x)$ and $\bar{u}$, a number of fluorescent filters need to be installed. The emitted light from the fluorescent dye as well as the tracer particles passes through a 532 nm dichroic mirror (Chroma Technology, Bellows Falls, USA) and a 532 nm long-pass filter (RazorEdge, Semrock, Rochester, NY, USA). A 594 nm dichroic mirror (Chroma Technology, Bellows Falls, USA) is used to separate the signals from each other, as illustrated in Figure C.1.

The limited wavelength separation efficiency of the 594 nm dichroic mirror can lead to additional background intensity in the particle image field, referred to as cross-talk, and therefore decreases the signal-to-noise ratio. Furthermore, it can lead to remaining particle signal in the droplet interface image. This can be overcome by installing additional long-pass and short-pass fluorescence filters in the bottom filter cube of the microscope (see Figure C.1).

As a result, particle displacements are measured by a camera mounted at a sideport of a TIRF-microscope (Eclipse Ti, Nikon Inc, Tokyo, Japan), while the signal required to determine the interface height $h(x, y)$ is measured by a camera mounted at the backport of the microscope. A cooled 12-bit dynamic range high resolution charged-coupled device (CCD) camera (FlowMaster, 1376 × 1040 pixels, individual pixel size 6.45 × 6.45 μm^2, LaVision GmbH, Goettingen, Germany) can be used to capture the emitted light by the Rhodamine B dye.

The signal strength of the dye can e.g. be increased by increasing the dye concentration, while keeping in mind fluorescence self-quenching. The emitted signal by the tracer particles can be collected on a cooled 14-bit dynamic low light EMCCD (iXon3 885, 1004×1002 pixels, individual pixel size 8×8 μm^2, Andor, Belfast, Northern Ireland). Both CCD and EMCCD have their peak quantum efficiency matched at the emitted wavelength by the fluorescent dye and particles respectively. The CCD has its peak quantum efficiency ranging from about 450 nm to 550 nm, whereas the EMCCD has its peak quantum efficiency ranging from about 600 nm to 700 nm.

C.3 Challenges

Besides the technical implications and required modifications to the experimental setup, many other challenges remain. For example, the use of quantum dots has advantages, such as a significant Stokes shift, a narrow emission spectrum, and no photobleaching. However, the use of small tracer particles also has disadvantages, namely small tracer particles give rise to Brownian motion. This random temperature induced motion leads to out-of-plane motion of particles. This can eventually lead to particle mismatch in e.g. a PTV approach and thus induces additional errors in the velocity field.

In order to suppress Brownian motion, a carrier fluid (e.g. glycerol) with a relatively high viscosity can be used (Bruus, 2008). Another concern of using quantum dots is intermittent blinking (Nirmal et al., 1996; Pouya et al., 2005; Guasto and Breuer, 2009). Blinking leads to particle dropout and additionally contributes to particle mismatch. Another concern is non-uniform tracer concentrations, which can greatly affect the near-wall velocity field measurements, as described by Li and Yoda (2010).

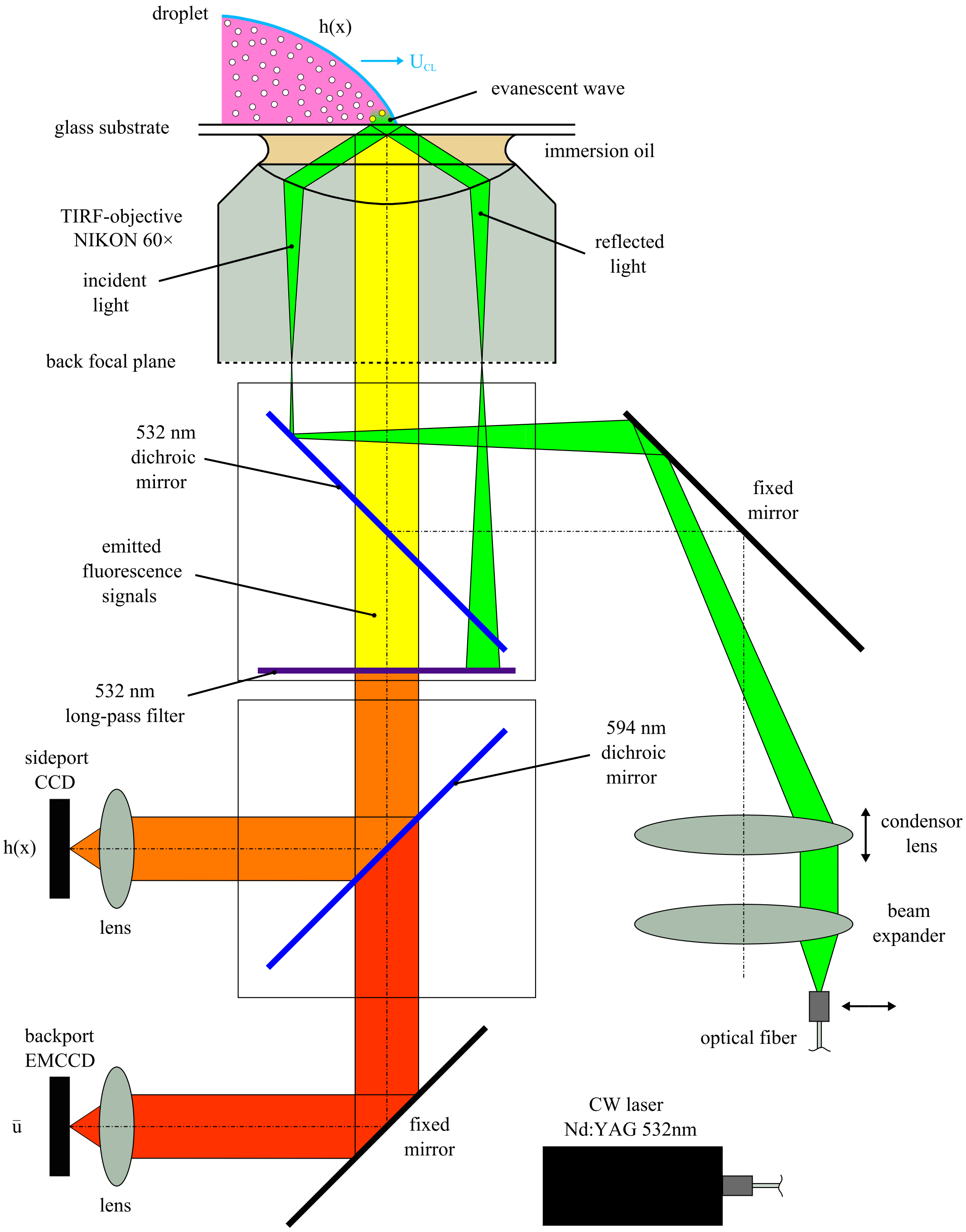

Figure C.1: Schematic of setup for combined LIF-TIRV.

Bibliography

R.J. Adrian and J. Westerweel. *Particle Image Velocimetry.* Cambridge University Press, 1st edition, 2010.

B.J. Alder and T.E. Wainwright. Decay of the velocity autocorrelation function. *Physical Review A*, **1**(1):18–21, 1970.

M. Antognozzi, A. Ulcinas, L. Picco, S.H. Simpson, P.J. Heard, M.D. Szczelkun, B. Brenner, and M.J. Miles. A new detection system for extremely small vertically mounted cantilevers. *Nanotechnology*, **19**(38), 2008.

D. Axelrod, T.P. Burghardt, and N.L. Thompson. Total internal reflection fluorescence. *Annual Review of Biophysics & Bioengineering*, **13**(1):247–268, 1984.

D. Beaglehole. Performance of a microscopic imaging ellipsometer. *Review of Scientific Instruments*, **59**(12):2557–2559, 1988.

D. Beaglehole. Profiles of the precursor of spreading drops of siloxane oil on glass, fused silica, and mica. *The Journal of Physical Chemistry*, **93**(2):893–899, 1989.

D. Bonn, J. Eggers, J. Indekeu, J. Meunier, and E. Rolley. Wetting and spreading. *Review of Modern Physics*, **81**(2):739–805, 2009.

F. Brochard-Wyart, P.G. de Gennes, H. Hervert, and C. Redon. Wetting and slippage of polymer melts on semi-ideal surfaces. *Langmuir*, **10**(5):1566–1572, 1994.

F. Brochard-Wyart, J.M. di Meglio, D. Quéré, and P.G. de Gennes. Spreading of nonvolatile liquids in a continuum picture. *Langmuir*, **7**(2):335–338, 1991.

R. Bruinsma. Slow spreading of polymer melts. *Macromolecules*, **23**(1):276–280, 1990.

H. Bruus. *Theoretical Microfluidics.* Oxford University Press, 1st edition, 2008.

H.-J. Butt, K. Graf, and M. Kappl. *Physics and Chemistry of Interfaces.* Wiley-VCH, 1st edition, 2003.

A.M. Cazabat. How does a droplet spread? *Contemporary Physics*, **28**(4):347–364, 1987.

A. Checco, P. Guenoun, and J. Daillant. Nonlinear dependence of the contact angle of nanodroplets on contact line curvature. *Physical Review Letters*, **91**, 186101, 2003.

J.-D. Chen and N. Wada. Wetting dynamics of the edge of a spreading drop. *Physical Review Letters*, **62**(26):3050–3053, 1989.

C. Cottin-Bizonne, C. Barentin, É. Charlaix, L. Bocquet, and J.-L. Barrat. Dynamics of simple liquids at heterogeneous surfaces: Molecular-dynamics simulations and hydrodynamic description. *The European Physics Journal E*, **15**:427–438, 2004.

F. de Fornel. *Evanescent waves from Newtonian Optics to Atomic Optics.* Springer, 1st edition, 2001.

P.G. de Gennes. Wetting: statics and dynamics. *Reviews of Modern Physics*, **57**(3): 827–863, 1985.

P.G. de Gennes, F. Brochard-Wyart, and D. Quéré. *Capillarity and Wetting Phenomena: Drops, Bubbles, Pearls, Waves.* Springer-Verlag, 2004.

B.V. Derjaguin and N.V. Churaev. Structural component of disjoining pressure. *Journal of Colloid and Interface Science*, **49**(2):249–255, 1974.

B.V. Derjaguin, A.S. Titijevskaia, I.I. Abricossova, and A.D. Malkina. Investigations of the forces of interaction of surfaces in different media and their application to the problem of colloid stability. *Discussions of the Faraday Society*, **18**:24–41, 1954.

P.A. Durbin. Considerations on the moving contact-line singularity, with application to frictional drag on a slender drop. *Journal of Fluid Mechanics*, **197**:157–169, 1988.

E.B. Dussan V. The moving contact line: the slip boundary condition. *Journal of Fluid Mechanics*, **77**(4):665–684, 1976.

E.B. Dussan V. On the spreading of liquids on solid surfaces: static and dynamic contact lines. *Annual Review of Fluid Mechanics*, **11**:371–400, 1979.

E.B. Dussan V and S.H. Davis. On the motion of a fluid-fluid interface along a solid surface. *Journal of Fluid Mechanics*, **65**(1):71–95, 1974.

P. Eaton and P. West. *Atomic Force Microscopy.* Oxford University Press, 1st edition, 2010.

J. Eggers, J.H. Lister, and H.A. Stone. Coalescence of liquid drops. *Journal of Fluid Mechanics*, **401**:293–310, 1999.

C.W. Extrand. A thermodynamic model for contact angle hysteresis. *Journal of Colloid and Interface Science*, **207**(1):11–19, 1998.

A. Fery, T. Pompe, and S. Herminghaus. Nanometer resolution of liquid surface topography by scanning force microscopy. *Journal of Adhesion Science and Technology*, **13**(10):1071–1083, 1999.

P. Fontaine, P. Guenoun, and J. Daillant. A critical look at surface force measurement using a commercial atomic force microscope in the noncontact mode. *Review of Scientific Instruments*, **68**(11):4145–4151, 1997.

M.J.Z. Franken, C. Poelma, and J. Westerweel. Nanoscale contact line visualization based on total internal reflection fluorescence microscopy. *ISFV14 - 14th International Symposium on Flow Visualization, June 21-24, EXCO Daegu, Korea*, 2010.

M.J.Z. Franken, C. Poelma, and J. Westerweel. Nanoscale contact line visualization based on total internal reflection fluorescence microscopy. *Optics Express*, **21**(22):26093–26102, 2013.

C. Gell, M. Berndt, J. Enderlein, and J. Diez. TIRF microscopy evanescent field calibration using tilted fluorescent microtubules. *Journal of Microscopy*, **234**(1):38–46, 2009.

E. Glynos, B. Frieberg, and P.F. Green. Wetting of a multiarm star-shaped molecule. *Physical Review Letters*, **107**, 118303, 2011.

H.P. Greenspan. On the motion of a small viscous droplet that wets a surface. *Journal of Fluid Mechanics*, **84**(1):125–143, 1978.

J.S. Guasto and K.S. Breuer. High-speed quantum dot tracking and velocimetry using evanescent wave illumination. *Experiments in Fluids*, **47**(6):1059–1066, 2009.

H. Gumpp, S.W. Stahl, M. Strackharn, E.M. Puchner, and H. E. Gaub. Ultrastable combined atomic force and total internal fluorescence microscope. *Review of Scientific Instruments*, **80**, 063704, 2009.

P.J. Haley and M.J. Miksis. The effect of the contact line on droplet spreading. *Journal of Fluid Mechanics*, **233**:57–81, 1991.

R.J. Hansen and T.Y. Toong. Dynamic contact angle and its relationship to forces of hydrodynamic origin. *Journal of Colloid and Interface Science*, **37**(1):196–207, 1971.

W.B. Hardy. The spreading of fluids on glass. *Philosophical Magazine Series 6*, **38**(223): 49–55, 1919.

S. Harlepp, J. Robert, N.C. Darnton, and D. Chatenay. Subnanometric measurements of evanescent wave penetration depth using total internal reflection microscopy combined with fluorescent correlation spectroscopy. *Applied Physics Letters*, **85**(17):3917–3919, 2004.

S. Herminghaus, T. Pompe, and A. Fery. Scanning force microscopy investigation of liquid structures and its application to fundamental wetting research. *Journal of Adhesion Science and Technology*, **14**(14):1767–1782, 2000.

H. Hervet and P.G. de Gennes. Physique des surfaces et des interfaces – dynamique du mouillage: films précurseurs sur solide. *Comptes Rendus de l'Académie des Sciences Série II*, **299**(9):499–503, 1984.

F. Heslot, A.M. Cazabat, N. Fraysse, and P. Levinson. Experiments on spreading droplets and thin films. *Advances in Colloid and Interface Science*, **39**:129–145, 1992.

A. Hoang, G. Berteloot, P. Sharif-Kashani, and H.P. Kavehpour. Dynamic measurement of microfilms and nanofilms of fluids using fluorescence microscopy. *Experiments in Fluids*, **52**(6):1657–1662, 2012.

A. Hoang and H.P. Kavehpour. Dynamics of nanoscale precursor film near a moving contact line of spreading drops. *Physical Review Letters*, **106**, 254501, 2011.

L.M. Hocking. A moving fluid interface on a rough surface. *Journal of Fluid Mechanics*, **76**(4):801–817, 1976.

L.M. Hocking. A moving fluid interface. Part 2. The removal of the force singularity by a slip flow. *Journal of Fluid Mechanics*, **79**(2):209–229, 1977.

P. Huang and K.S. Breuer. Direct measurement of slip length in electrolyte solutions. *Physics of Fluids*, **19**, 028104, 2007.

P. Huang, J.S. Guasto, and K.S. Breuer. Direct measurement of slip velocities using three-dimensional total internal reflection velocimetry. *Journal of Fluid Mechanics*, **566**:447–464, 2006.

C. Huh and S.G. Mason. The steady movement of a liquid meniscus in a capillary tube. *Journal of Fluid Mechanics*, **81**(3):401–419, 1977.

C. Huh and L.E. Scriven. Hydrodynamic model of steady movement of a solid/liquid/fluid contact line. *Journal of Colloid and Interface Science*, **35**(1):85–101, 1971.

J.N. Israelachvili. *Intermolecular & Surface Forces*. Academic Press, 2nd edition, 1997.

A. Jabbarzadeh, J.D. Atkinson, and R.I. Tanner. Effect of wall roughness on slip and rheological properties of hexadecane in molecular dynamics simulation of Couette shear flow between two sinusoidal walls. *Physical Review E*, **61**(1):690–699, 2000.

S. Jin, P. Huang, J. Park, J.Y. Yoo, and K. Breuer. Near-surface velocimetry using evanescent wave illumination. *Experiments in Fluids*, **37**(6):825–833, 2004.

J.F. Joanny and P.G. de Gennes. Upward creep of a wetting fluid: a scaling analysis. *Journal de Physique*, **47**(1):121–127, 1986.

K. Kanda, S. Ogata, K. Jingu, and M. Yang. Measurement of particle distribution in microchannel flow using a 3D-TIRFM technique. *Journal of Visualization*, **10**(2):207–215, 2007.

H.P. Kavehpour, B. Ovryn, and G.H. Mckinley. Microscopic and macroscopic structure of the precursor layer in spreading viscous drops. *Physical Review Letters*, **91**, 196104, 2003.

H. Kim. *Moving liquid droplets with inertia: Experiment, simulation, and theory.* PhD thesis, Delft University of Technology, 2013.

S. Kim, S. Jin, and J.Y. Yoo. Flow near the meniscus of a pressure-driven water slug in microchannels. *Journal of Mechanical Science and Technology*, **20**(5):710–716, 2006.

K. Kling and D. Mewes. Two-colour laser induced fluorescence for the quantification of micro- and macromixing in stirred vessels. *Chemical Engineering Science*, **59**(7):1523–1528, 2004.

T. Konisho and I. Ueno. Detection of advancing edge and length of precursor film ahead of macroscopic contact line of droplet spreading on solid substrate. *Annals of the New York Academy of Sciences*, **1161**:292–303, 2009.

U. Landman, W.D. Luedtke, N.A. Burnham, and R.J. Colton. Atomistic mechanics and dynamics of adhesion, nanoindentation, and fracture. *Science*, **248**(4954):454–461, 1990.

D. Lasne, A. Maali, Y. Amarouchene, L. Cognet, B. Lounis, and H. Kellay. Velocity profiles of water flowing past solid glass surfaces using fluorescent nanoparticles and molecules as velocity probes. *Physical Review Letters*, **100**, 214502, 2008.

L. Léger, M. Erman, A.M. Guinet-Picart, D. Ausserre, C. Strazielle, J.J. Benattar, F. Rieutord, J. Daillant, and L. Bosio. Spreading of non volatile liquids on smooth solid surfaces: role of long range forces. *Revue de Physique Appliquée*, **23**:1047–1054, 1988a.

L. Léger, M. Ertnan, A.M. Guinet-Picard, D. Ausserre, and C. Strazielle. Precursor film profiles of spreading liquid drops. *Physical Review Letters*, **60**(23):2390–2393, 1988b.

H. Li, R. Sadr, and M. Yoda. Multilayer nano-particle image velocimetry. *Experiments in Fluids*, **41**(2):185–194, 2006.

H. Li and M. Yoda. An experimental study of slip considering the effects of non-uniform colloidal tracer distributions. *Journal of Fluid Mechanics*, **662**:269–287, 2010.

Y.-C. Liao, Y.-C. Li, and H.-H. Wei. Drastic changes in interfacial hydrodynamics due to wall slippage: slip-intensified film thinning, drop spreading, and capillary instability. *Physical Review Letters*, **111**, 136001, 2013.

D. Loerke, B. Preitz, W. Stühmer, and M. Oheim. Super-resolution measurements with evanescent-wave fluorescence excitation using variable beam incidence. *Journal of Biomedical Optics*, **5**(1):23–30, 2003.

J. Lowndes. The numerical simulation of the steady movement of a fluid meniscus in a capillary tube. *Journal of Fluid Mechanics*, **101**(3):631–646, 1980.

C. Mack. *Fundamental Principles of Optical Lithography: The Science of Microfabrication*. John Wiley & Sons, Ltd, 2007.

O. Marti, H. Bielefeldt, B. Hecht, S. Herminghaus, P. Leiderer, and J. Mlynek. Near-field optical measurement of the surface plasmon field. *Optics Communications*, **96**(4-6): 225–228, 1993.

A.L. Mattheyses and D. Axelrod. Direct measurement of the evanescent field profile produced by objective-based total internal reflection fluorescence. *Journal of Biomedical Optics*, **11**(1):014006, 2006.

S.R. Maymoudi, K. Adamiak, G.S.P. Castle, and K.K. Varanasi. Electrostatic precursor films. *Soft Matter*, **9**(41):9918–9923, 2013.

F. Mugele, T. Becker, R. Nikopoulos, M. Kohonen, and S. Herminghaus. Capillarity at the nanoscale: an AFM view. *Journal of Adhesion Science and Technology*, **16**(7):951–964, 2002.

G. Nagayama and P. Cheng. Effect of interface wettability on microscale flow by molecular dynamics simulation. *International Journal of Heat and Mass Transfer*, **47**(3):501–513, 2004.

C.L.M.H. Navier. Mémoire sur les lois du mouvement des fluides. *Mémoires de l'Académie Royale des Sciences de l'Institut de France*, **6**:389–440, 1823.

M. Nirmal, B.O. Dabbousi, M.G. Bawendi, J.J. Macklin, J.K. Trautman, T.D. Harris, and L.E. Brus. Fluorescence intermittency in single cadmium selenide nanocrystals. *Nature*, **383**:802–804, 1996.

N. Pamme. Continuous flow separations in microfluidic devices. *Lab on a Chip*, **7**(12): 1644–1659, 2007.

M.N. Popescu, G. Oshanin, S. Dietrich, and A.M. Cazabat. Precursor films in wetting phenomena. *Journal of Physics: Condensed Matter*, **24**(24):1–30, 2012.

S. Pouya, M. Koochesfahani, P. Snee, M. Bawendi, and D. Nocera. Single quantum dot (QD) imaging of fluid flow near surfaces. *Experiments in Fluids*, **39**(4):784–786, 2005.

J. Ralston, M. Popescu, and R. Sedev. Dynamics of wetting from an experimental point of view. *Annual Review of Materials Research*, **38**:23–43, 2008.

O. Reynolds. On the theory of lubrication and its application to Mr. Beauchamp Tower's experiments, including an experimental determination of the viscosity of olive oil. *Philosophical Transactions of the Royal Society*, **177**:157–234, 1886.

M. Riepen, F. Evangelista, and S. Donders. Contact line dynamics in immerson lithography − Dynamic contact angle analysis. *Proceedings of the 1st European Conference on Microfluidics, Bologna, Italy*, 2008.

R. Sadr, M. Yoda, Z. Zheng, and A.T. Conlisk. An experimental study of electro-osmotic flow in rectangular microchannels. *Journal of Fluid Mechanics*, **506**:357–367, 2004.

A. Sarkar, R.B. Robertson, and J.M. Fernandez. Simultaneous atomic force microscope and fluorescence measurements of protein unfolding using a calibrated evanescent wave. *Proceedings of the National Academy of Sciences*, **101**(35):12882–12886, 2004.

J.H. Snoeijer and B. Andreotti. Moving contact lines: scales, regimes, and dynamical transitions. *Annual Review of Fluid Mechanics*, **45**:269–292, 2013.

V.P. Sokhan, D. Nicholson, and N. Quirke. Fluid flow in nanopores: Accurate boundary conditions for carbon nanotubes. *Journal of Chemical Physics*, **117**(18):8531–8539, 2002.

V.M. Starov, M.G. Velarde, and C.J. Radke. *Wetting and Spreading Dynamics.* CRC Press, 1st edition, 2007.

J.A. Steyer and W. Almers. Tracking single secretory granules in live chromaffin cells by evanescent-field fluorescence microscopy. *Biophysics Journal*, **76**(4):2262–2271, 1999.

K. Stock, R. Sailer, W.S.L. Strauss, M. Lyttek, R. Steiner, and H. Schneckenburger. Variable-angle total internal reflection fluorescence microscopy (VA-TIRFM): realization and application of a compact illumination device. *Journal of Microscopy*, **211**: 19–29, 2003.

R. Tadmor, P. Bahadur, A. Leh, H.E. N'guessan, R. Jaini, and L. Dang. Measurement of lateral adhesion forces at the interface between a liquid drop and a substrate. *Physical Review Letters*, **103**, 266101, 2009.

G.F. Teletzke, H.T. Davis, and L.E. Scriven. Wetting hydrodynamics. *Revue de Physique Appliquée*, **23**(6):989–1007, 1988.

R.S. Voronov, D.V. Papavassiliou, and L.L. Lee. Slip length and contact angle over hydrophobic surfaces. *Chemical Physics Letters*, **441**(4-6):273–276, 2007.

D. Wang, C. Meinhart, and M. Sigurdson. Two-color micro PIV measurements of particle and fluid motion in AC electrokinetics. *Proceedings of IMECE2003. 2003 ASME International Mechanical Engineering Congress and Exposition, Washington, USA*, 2003.

W. Wang, J.S. Guasto, and P. Huang. Measurement bias in evanescent wave nanovelocimetry due to tracer size variations. *Experiments in Fluids*, **51**(6):1685–1694, 2011.

H. Xu, D. Shirvanyants, K. Beers, K. Matyjaszewski, M. Rubinstein, and S.S. Sheiko. Molecular motion in a spreading precursor film. *Physical Review Letters*, **93**, 206103, 2004.

X.F. Yang. Equilibrium contact angle and intrinsic wetting hysteresis. *Applied Physics Letters*, **67**(15):2249–2251, 1995.

Acknowledgements

This thesis is the result of about four-and-a-half years of research in the Laboratory for Aero and Hydrodynamics at Delft University of Technology. Although only my name is present on the cover of the thesis, it would not have been established without the help, support, and guidance of many people.

Firstly and foremostly, I would like to thank my promotor and supervisor Jerry Westerweel for his support, encouragement, inspiration, and patience, while giving me the freedom and opportunity to work on my own ideas. The choice of research path not only resulted in this thesis, but also into many discussions.

Secondly, I would like to thank my co-promoter and daily supervisor Christian Poelma for his advice and guidance especially on the data analysis and experimental aspects of the thesis. In the final stage of the project Gijs Ooms and Mathieu Pourquie have been of great value regarding the theoretical work on precursor films and eventually got me back on track.

Because my research project was part of the research programme 'Contact Line Control during Wetting and Dewetting' (CLC) of the 'Stichting voor Fundamenteel Onderzoek der Materie (FOM)', which was financially supported by the 'Nederlandse Organisatie voor Wetenschappelijk Onderzoek (NWO)', I would like to thank all the people involved in the somewhat regular meetings. In particular Ramin Badie, Michel Riepen, and co-workers at ASML in Veldhoven for their enthusiasm about the project.

I wish to express my sincere gratitude to everybody that contributed to the pleasant and helpful working environment in the lab: Arnoud, Astrid, Carole, Christian, Daniele, Dirk-Jan, Edwin, Gea, Gerrit, Gosse, Jan, Jasper Ruijgrok, Jasper Tomas, Jeanette, Jerke, Manu, Marc, Marcel, Marieke, Mathieu, Nikolay, Norbert, Pedro, Pepijn, René, Sasha, Sebastian, Sedat, Sita, Uli, Valentina, Vincent, and Wim-Paul. I enjoyed the coffee breaks, the go-karting, the BBQ's, the movie evenings, the lab outings, the bowling events, the pub evenings, and the game evenings very much. In particular, I would like to thank Gosse, I really enjoyed the nerve-wrecking table soccer games at *Gezelschap Leeghwater* during lunch breaks on Fridays.

I am particulary grateful to my office mates, Sasha, and (the Italian invasion of) Valentina and Daniele. I enjoyed the time we spent together, the discussions of (my) Dutch habits, the laughs, the coffee breaks, the pasta-problem discussions, etc. Without my office mates, the time in the laboratory would definitely not have been as pleasant as it was.

Additionally, I would like to thank fellow Ph.D.'s; Dieter 't Mannetje, Jolet and Riëlle de Ruiter, and Christian Berendsen for contributing to a pleasant (non-) scientific atmosphere during regular scientific meetings.

The results presented in this thesis could not have been obtained without the support of technical and administrative staff. For this reason, I would like to thank Caroline, Cor, Edwin, Jasper, Joop, Ria, and Simon. Undoubtedly, the attended English courses have resulted in a more readable thesis, for this I am grateful to Froukje van Veggel and Maaike Beliën. Additionally, I would like to thank Edwin for providing me with freshly roasted coffee beans. Your beans resulted in a coffee that kept me awake during late evenings of homework.

Not only the support within the laboratory was important, but also the technical support by Ernst van Duijvendijk, Herman Fennema, and Donald van Velzen of Nikon Instruments Europe. Their support was appreciated very much, and have resulted in a Nikon microscope that could eventually be used throughout my Ph.D. As explained in Chapter 3, a combined TIRFM-AFM setup was required to characterize the evanescent field. However, the first attempts of this characterization were done with a Veeco diCaliber, which was installed by Patrick Markus. I am very grateful to him for teaching me the basics of AFM-imaging and the pleasant conversations.

Eventually, an AIST-NT system was installed to perform a simultaneous TIRFM-AFM measurement. For this, I would like to thank Peter Vernhout and co-workers at AIST-NT for providing the required technical support to get the CombiScope up and running. Considering the AFM-measurements described in Chapter 3 and 4, I am very grateful to Marcel Bus and Anika Embrechts for the fruitful discussions regarding non-disturbing AFM-imaging and the ~~problems~~ challenges with the experimental setup. Anika, besides the numerous discussions on AFM-imaging, I enjoyed the beers (and the continuation of our discussions) on the Beestenmarkt very much.

Besides the research on precursor films, I worked on near-wall flow physics with nano-PIV as a side project. This work has been done together with a M.Sc.-student Can Tümer. I would like to thank him for doing the graduation project in the first place, and second, for the pleasant discussions during the extensive measurement campaigns.

Als laatste wil ik mijn ouders, pa en ma, en mijn broers Richard en Arno, bedanken voor jullie belangstelling, steun, vertrouwen, en gezelligheid in de afgelopen jaren. Het zijn voornamelijk de kleine dingen die er uiteindelijk toe doen.

Mark Franken
Delft, January 2014

About the Author

Mark Franken was born on 11 January, 1983 in Rotterdam, the Netherlands. His secondary education was followed at the Regionale Scholen Gemeenschap in Oud-Beijerland. After finishing his secondary education in 2001, he started studying mechanical engineering at the Hogeschool Rotterdam in Rotterdam. In 2008 he obtained his M.Sc. degree after performing a graduation project on contactless positioning using an air film at the department of Precision & Microsystems Engineering. This graduation project started his interest in fluid mechanics, in particular microfluidics. Therefore, he continued his investigations into the small scale fluid dynamics as a Ph.D. candidate at the Laboratory for Aero & Hydrodynamics, faculty of Mechanical, Maritime and Materials Engineering at Delft University of Technology in November 2008. The research topic was the study of nanoscale contact line dynamics, including the development and validation of a novel measurement technique. The results are presented in this thesis.